UNIVERSITY OF OKLAHOMA

GRADUATE COLLEGE

NOCTURNAL BOUNDARY LAYER AND LOW-LEVEL JET CHARACTERISTICS UNDER DIFFERENT TURBULENCE REGIMES

A DISSERTATION

SUBMITTED TO THE GRADUATE FACULTY

in partial fulfillment of the requirements for the

Degree of

DOCTOR OF PHILOSOPHY

By

TIMOTHY ANDREW BONIN
Norman, Oklahoma
2015

NOCTURNAL BOUNDARY LAYER AND LOW-LEVEL JET CHARACTERISTICS UNDER DIFFERENT TURBULENCE REGIMES

A DISSERTATION APPROVED FOR THE
SCHOOL OF METEOROLOGY

BY

Dr. Petra Klein, Co-Chair

Dr. Phillip Chilson, Co-Chair

Dr. Alan Shapiro

Dr. David Turner

Dr. David Miller

Dedication

To my family for always encouraging and supporting me, and to my friends for always raising my spirits.

Acknowledgements

Firstly, I would like to thank both of my co-advisors, Dr. Petra Klein and Dr. Phillip Chilson, for all of their guidance, support, and giving me the opportunity to work on this project and to make it my own. They have encouraged me to pursue my own research interests and allowed a lot of freedom in deciding my dissertation topic. Their advice, in numerous aspects, has helped me become a better and more knowledgeable scientist, for which I am very grateful.

I would also like to thank all the members of my committee, Dr. David Miller, Dr. Alan Shapiro, and Dr. David Turner, for their valuable time and input which have greatly improved the quality of this dissertation. Discussions with each of them, and Dr. Evgeni Fedorovich, have greatly increased my knowledge on a variety of subjects making me a more well-rounded researcher.

I am grateful to the many fellow graduate students and friends with whom I've had numerous discussions. They have also lifted my spirits in tough times.

I am especially thankful for my family for always loving, supporting, and encouraging me to follow my dreams and passion, even when that took me far away from home.

Finally, I am especially grateful for Jennifer Newman for everything she has done for me.

Contents

List Of Tables

List Of Figures

Abstract

The intensity, extent, and continuity of turbulence in the nocturnal stable boundary layer (SBL) is governed by many interacting processes and features. Generally, SBLs can be grouped into two broad categories: weakly stable and very stable. While the weakly SBL is relatively well understood and can be described by Monin-Obukhov similarity theory or other local scaling laws, the very SBL is difficult to characterize and parameterize. It is also difficult to predict which type of SBL will form nocturnally as differentiating characteristics of the two regimes are not well-known. Furthermore, nocturnal low-level jets (LLJs) often form around sunset, particularly in the Great Plains region of the United States, and generally interact with the nocturnal SBL. These relationships between LLJs and the SBL are currently not well-understood.

To characterize turbulence within the SBL, vertical velocity variances estimated from Doppler lidar (DL) observations are used, which first need to be validated. To accomplish this, DL-derived values of vertical velocity variance are directly compared with those from sonic anemometer observations installed on a 300-m tower during the Lower Atmospheric Thermodynamics and Turbulence Experiment (LATTE), which was conducted in February–April 2014 at the Boulder Atmospheric Observatory . An autocovariance method of removing noise from the DL observations is used, which is shown to improve measurements of vertical velocity variance. In addition to removing noise, this method can also correct

for underestimates of variance due to time and volume averaging of the DL. Generally, the DL-derived variance values tend to agree closely with those from the sonic anemometers after the autocovariance correction is applied.

To investigate the SBL in detail, Doppler lidar, sonic anemometer, Atmospheric Emitted Radiance Interferometer (AERI), and radiosonde measurements that were collected during the Lower Atmospheric Boundary Layer Experiment (LABLE-I) are analyzed. LABLE-I was a multi-institutional field campaign that took place from 18 September to 13 November 2012 at the Southern Great Plains site in north central Oklahoma. During the experiment, LLJs were frequently observed and interacted with both weakly and very stable SBLs. Within the weakly stable boundary layer, turbulence tended to be generated at the surface and transported upward, and no strong surface-based inversion formed overnight. When a strongly stable boundary layer formed, mixing was either generated near a LLJ or at the surface and remained very weak overnight. On these nights, a strong surface based inversion formed and slowly grew throughout the night.

LLJs also evolved differently depending on if a weakly or strongly SBL formed. With a strongly SBL, LLJs tended to increase in both strength and height overnight, often corresponding to a gradual increase in synoptic-scale forcing. LLJs that occurred with a weakly SBL generally remained constant in height overnight, and reached a peak in strength around midnight. These LLJs often had approximately constant large-scale forcing overnight, thus their evolution more closely resembled what is expected by an inertial oscillation.

Chapter 1

Introduction

1.1 The Planetary Boundary Layer

The planetary boundary layer (PBL), the lowest part of the atmosphere just above the surface, is a critical component of the Earth-atmosphere system. Conditions within the PBL have profound impacts on people's lives and livelihood, and at the same time human modifications of the land surface strongly affect conditions within the PBL. There are also tremendous economical impacts of weather in the PBL. Just to name a few examples, frost and freezes can cause losses of crops (Miller and Glantz 1988), strong turbulence can damage wind turbines (Vermeer et al. 2003), and fog formation can cause significant weather delays resulting in lost revenue for airlines (Valdez 2000). With such high impacts from conditions in the PBL, it is imperative that the weather within it is well-understood and can be accurately predicted, so that preventative measures can be taken to limit losses from adverse conditions.

The structure of the daytime convective boundary layer (CBL) differs drastically from the structure of the nocturnal stable boundary layer (SBL), as shown in Fig. 1.1. During the day, the CBL generally is dominated by strong turbulence

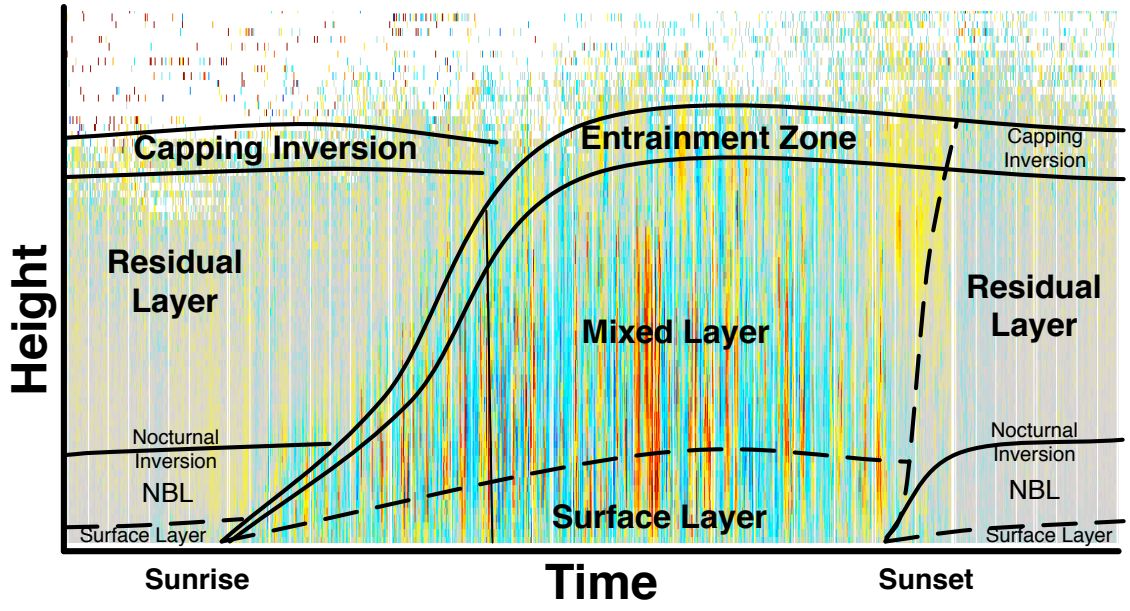

Figure 1.1: Schematic of the typical diurnal variation of the PBL, overlaid on vertical velocity data from a Doppler lidar. Reds indicate rising motion and blues indicate sinking motion, with brighter colors meaning stronger velocities. Grey indicates no vertical motion. Layers within the PBL are marked and labeled. (Figure modified after Stull (1988)).

that mixes quantities such as potential temperature, moisture, momentum, pollutants and trace gases throughout the depth of the PBL. As such, within the mixed layer, these quantities are relatively constant with height. Below the mixed layer is the surface layer, wherein the temperature profile is superadiabatic and moisture increases towards the surface. Additionally, roughness elements at the surface strongly affect the mean profiles of turbulence and wind within the surface layer, leading to a logarithmic wind profile within it (Garratt 1992).

Around sunset, the PBL undergoes a dramatic evolutuion during the early evening transition (EET) period. At this time, turbulence decays throughout the depth of the formerly well developed CBL (Nieuwstadt and Brost 1986). Concurrently within a shallow layer near the surface, temperature rapidly decreases as a

radiation inversion begins to form and moisture increases (Acevedo and Fitzjarrald 2001; Bonin et al. 2013). Typically, strong static stability limits the amount of mixing that can occur overnight. However, low-level jets (LLJs) develop on some nights, which will be the focus of this dissertation. These LLJs are associated with strongly sheared layers which can overcome the strong static stability to generate significant turbulence overnight.

1.2 The Low-Level Jet

Throughout the last 50+ years, LLJs have been a topic of frequent discussion in the literature. Papers address the possible mechanisms for the formation of the jet, climatologies of the LLJ (e.g., Bonner 1968; Mitchell et al. 1995), effects of the LLJ on the weather on scales from local to synoptic (e.g., Stensrud 1996; Higgins et al. 1997), and turbulence profiles associated with LLJs (e.g. Banta et al. 2006), among other subjects. In the American Meteorological Society glossary, the LLJ is given a broad definition as 'a jet stream that is typically found in the lower 2–3 km of the troposphere.' Bonner (1968) provides a more focused definition in which a LLJ is defined as a local wind maximum that exceeds 12 m s^{-1} in the lowest 2.5 km above ground level (AGL), and the wind must decrease to half of the wind speed maximum above the jet but below 3 km. This definition is further divided into different classes based on the maximum wind speed in the jet, in which criteria-1 LLJs have a wind speed >12 m s^{-1}, criteria-2 LLJs have a wind speed >16 m s^{-1}, and criteria-3 LLJs have a wind speed >20 m s^{-1}. Blackadar

(1957) used different criteria in his study of low-level wind speed maxima, but did not specifically refer to the maximum as a LLJ since the term was not used widely at the time. In his definition, a low-level wind maximum was noted if it occurred in the lowest 1.5 km AGL and the wind decreased by at least 5 kt (2.57 m s^{-1}) to the next higher minimum. In many climatologies of the LLJ, the Bonner (1968) definition has been typically used. However, a looser definition more similar to the Blackadar (1957) has often been used when investigating PBL processes associated with LLJs.

1.2.1 Climatology

Over the years, numerous studies have addressed the climatology of the LLJ. The strategies used to accurately capture the climatology of the LLJ have changed with the advancement of technology. LLJs have been observed all over the world, on or around every continent, and have taken many forms. Stensrud (1996) provides a comprehensive review of literature up to the publication date detailing the location of the LLJs and discusses the importance of LLJs on climate. In this review, it is noted that LLJs typically occur to the east of a large mountain range or where a significant land-sea gradient exists. Rife et al. (2010) used 21-yr global mesoscale reanalysis to create an updated worldwide climatology of LLJs, shown in Fig. 1.2. A seasonal dependence is clearly visible, with LLJs being much more prevalent in summer months. While LLJs can be found in many locations around the world, one of largest in areal coverage, strongest, and most studied LLJs occurs in the

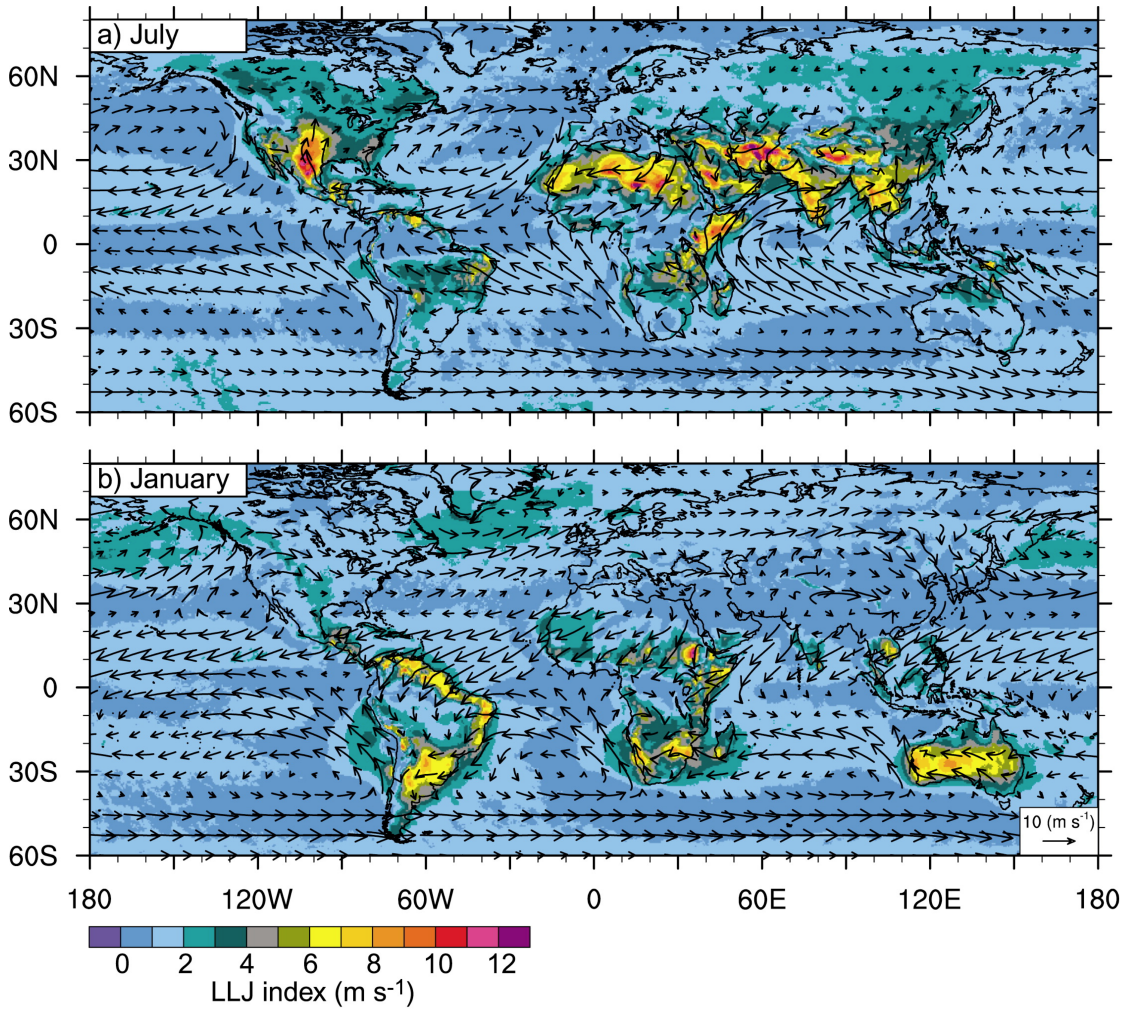

Figure 1.2: Mean LLJ index (shaded) and 500-m AGL winds (arrows) at local midnight for 1985-2005 for a) July and b) January. LLJ index considers both the strength of the diurnal cycle and the winds at 500-m AGL relative to 4-km AGL. (Figure from Rife et al. (2010)).

Great Plains region of the United States. The Great Plains LLJ will be the focus of this paper henceforth.

Bonner (1968) conducted the first thorough study of the Great Plains LLJ using 2 years of radiosonde data at 6-hr intervals over the United States. He found that the LLJ occurs most frequently and is associated with the highest wind speeds at night, with a maximum in the magnitude of the winds at midnight local time.

Additionally, Bonner (1968) showed that LLJs climatologically occur most frequently in northwestern Oklahoma, most often form during the summer months, and tend to be southerly or southwesterly. Northerly LLJs are often observed as well, especially in winter. These typically occur after a cold front passes and are essentially large-scale density currents (Whiteman et al. 1997). Recently, Walters et al. (2008) provided an updated climatology of LLJs using 40-years of radiosonde observations at 0000 UTC and 1200 UTC, and found the summertime climatological maximum of the LLJ to be located in a similar area shown by Bonner (1968). However, the annual LLJ maximum was located farther south over Texas.

More recently, Mitchell et al. (1995) used a network of wind profilers scattered over the Great Plains to create an updated climatology of the LLJ, using hourly profiles instead of the 6-hourly radiosonde profiles that were available to Bonner (1968). A similar climatological maximum was found over Oklahoma, with the maximum occurring over the late summer months. However, Mitchell et al. (1995) found that the height of the LLJ was slightly higher at around 1 km with some spatial variability. The height increase is likely due the lower vertical resolution of the wind profiler datasets compared to rawinsonde profiles. Additionally, the lowest range-gate of the wind profilers is 500-m, so any LLJs below that height cannot be captured.

Both Whiteman et al. (1997) and Song et al. (2005) took advantage of the rich data set available from a large suite of instruments at the Atmospheric Radiation

Measurement (ARM) Southern Great Plains (SGP) site operated by the United States Department of Energy (DOE), including additional data collected during various experiments at the site. Details about the ARM SGP site, which is situated near the climatological maximum of LLJ occurrence, can be found in Sect. 3.2. Both studies found that the maximum wind speed with the LLJ was frequently located within a layer 250–500 m above the ground. Song et al. (2005) also compared observations from nearby sites that were at different elevations, and found that the LLJ tended to remain constant with height with respect to sea level.

1.2.2 Mechanisms

Blackadar (1957) formulated the first theory to explain the LLJ as an inertial oscillation. The inertial oscillation is essentially the diurnal fluctuation of momentum, oscillating around the geostrophic wind, as turbulent mixing increases and decreases over a 24-hr cycle. Around sunset, turbulent mixing rapidly diminishes within the PBL. During this time, the flow above the surface begins to accelerate, as only a small amount of momentum from this layer is transported downward from the weak nighttime mixing. With this theory, the maximum wind speed with the LLJ would be located at the top of the nocturnal inversion. The inversion slowly grows overnight as air cooled at the surface slowly is transported upward through the weak turbulence that is generated by the strong shear associated with the LLJ. Radiative flux divergence in this near-surface layer also leads to intensification of the surface-based inversion. Strong shear is not supported above the jet

since the thermodynamic profile, above the inversion, is much less statically stable. Thus, below the LLJ nose shear is strong but turbulent mixing is weak while above the LLJs nose shear is weak but mixing is strong. The period of this inertial oscillation depends on latitude, as the period is π/f. Here, f is the Coriolis frequency defined as $2\omega\sin(\phi)$, where ω is rotation rate of the Earth and ϕ is the latitude. Van de Wiel et al. (2010) recently expanded upon this theory to include the effects of friction within the nocturnal SBL, and showed that the velocity profile oscillates around the nighttime equilibrium profile, not the geostrophic wind.

Both Holton (1967) and Shapiro and Fedorovich (2009) formulate that the Southern Great Plains LLJ forms due to the sloping terrain that is present over the region, but different reasons are discussed in the two papers. Holton (1967) showed that a periodic radiative forcing term could explain the observed diurnal wind oscillation, but it did not adequately reproduce the phasing of observed LLJs. Shapiro and Fedorovich (2009) considered the thermal structure of the lower atmosphere and how it changes horizontally over a gently sloping terrain. The residual layer of the PBL is tilted over the terrain. Due to the tilt of the residual layer with respect to the stably stratified free atmosphere, gradients in buoyancy exist which cause the flow to accelerate over time. This leads to a jet for which the evolution is supported by observations.

Wexler (1961) proposed that the high frequency of LLJs in the Great Plains region is due to the large-scale blocking of low-level winds by the Rocky Mountains. The easterly trade winds are deflected northward as they approach the Rocky

Mountains, resulting in the observed strong southerly flow. This is analogous to the intensification of ocean currents along eastern seaboards (Stommel 1948). Ting and Wang (2006) examined the role of the terrain by simulating the flow with real terrain features and treating North America as a flat surface, and found that the predominant strong southerly winds would not dominate over the Great Plains if the terrain were flat. However, the blocking by the Rocky Mountains alone does not explain the periodicity of the observed LLJ, which can only be explained by the other aforementioned theories.

There are the three main mechanisms that have been proposed to explain the formation and evolution of the LLJ. Each has been somewhat supported by follow-up studies, and all of the mechanisms likely work together to form and maintain the LLJ. It is also plausible that multiple LLJs may form at different heights overnight if the mechanisms are not working in unison, and each jet may have its own unique characteristics associated with it.

1.2.3 Effects on Atmosphere at Larger and Smaller Scales

The LLJ itself has significant impacts on the atmosphere over a wide range of time and size scales. Stensrud (1996) provides a thorough review of how LLJs affect regional climatologies. One of the most significant climatological effects of LLJs is the large poleward moisture flux. The LLJ transports moisture long distances from the Gulf of Mexico into the Great Plains, contributing significantly to the amount of rainfall over the region (Higgins et al. 1997). In fact, strong

LLJs that occur frequently during the summer months over the same area can lead to catastrophic flooding causing significant agricultural losses, such as was the case over the Mississippi Valley region during the summer of 1993 flood (Arritt et al. 1997). Much of this rainfall occurs when nocturnal Mesoscale Convective Systems (MCSs) form, which frequently happens when a LLJ impinges on an existing surface-boundary such as a stalled front (Augustine and Caracena 1994).

In addition to transporting moisture, LLJs can also transport pollutants and other tracers long distances during the night, where they are mixed downward to the surface. In Germany at a rural site, Corsmeier et al. (1997) found that ozone concentrations frequently increased overnight as LLJs transported the ozone several hundred kilometers, where it was mixed downward by turbulence created by the LLJ itself. Similarly, Hu et al. (2013b) showed that vertical mixing at night associated with LLJs removed ozone from the residual layer causing a secondary maxima at night, but also reduced the surface ozone concentrations the following day. LLJs also can cause intermittent exchange of carbon dioxide above forests and agricultural fields, resulting in either a buildup for venting of carbon dioxide within the canopy layer (Karipot et al. 2006).

Urban boundary layers (UBLs) are also significantly impacted when a LLJ impinges on a city. Wang et al. (2007) showed that over the central business district of Oklahoma City, the LLJ is 25–100 m higher than over the surrounding

suburban area due to the higher roughness elements and different thermal properties. Lundquist and Mirocha (2007) discussed the importance of including larger-scale influences when modeling the UBL, by adequately capturing the LLJ within a computational simulation, in order to accurately estimate the turbulent mixing generated within an UBL at night. The intensity of the urban heat island was also found to be related the the strength of the LLJ, as nights with strong LLJs tended to induce mechanical mixing throughout the night, thus preventing a strong nocturnal inversion and urban heat island from forming (Hu et al. 2013a). Relating UBLs with the dispersion of air pollutants, Klein et al. (2014) showed that the strongest LLJs are associated with highest urban ozone concentrations, due to the long-range transport and persistent downward mixing of the ozone reservoir in the residual layer towards the surface.

On a much smaller scale than the above-mentioned LLJ-atmospheric interactions, the strong shear layers associated with LLJs can generate substantial amounts of mixing within the PBL. This is the mechanism that transports pollutants down to the surface, as mentioned in the earlier section. However, the amount of turbulent mixing varies greatly depending on the LLJ, as discussed by Banta et al. (2006). A thorough review of the literature, covering turbulence within the LLJ and associated SBL, is discussed is detail within Ch. 3. To date, discriminating characteristics between strongly turbulent and weakly turbulent LLJs are not well-known. Near-surface thermodynamic stability is likely a key difference.

However, continuous high temporal and spatial (in the vertical) resolution thermodynamic measurements are needed to quantify and understand the static stability within the SBL, which are not currently available in most field campaigns. Herein, measurements from a passive remote sensor, the Atmospheric Emitted Radiance Interferometer (AERI), are used to investigate the time-evolution of the temperature profile throughout the lowest 1-km and differing types of SBLs and LLJs for the first time.

1.2.4 Direct Relevance to Industry and Human Activities

In addition to the indirect effects of LLJs on human activity through the aforementioned weather modification, LLJs also have more direct effects on several different industries. Aviation is affected by LLJs in several ways. If the LLJ winds are across a runway, wake vortices generated by aircraft are differentially transported with height, impacting how closely aircraft can consecutively land (Kaplan et al. 2000). If the LLJ is relatively aligned with the runway, the sharp decrease in wind speed with height as an aircraft is landing reduces the lift of the aircraft, which can cause aircraft to land short of the runway (Neyland 1956). If the existence of these LLJs is known beforehand, aircraft traffic control and pilots can anticipate these effects beforehand to ensure safe landings.

LLJs have a mixture of positive and negative effects on the wind energy industry, as discussed in detail by Storm et al. (2009). Of course, the strong winds associated with LLJs allow for tremendous generation of renewable energy. However,

the strong directional and speed shear associated with the LLJs can cause damage and shorten the typical lifespan of wind turbine rotors (Kelley et al. 2006). Additionally, the strong turbulence that can be generated by LLJs both reduces power production and damages mechanical parts of wind turbines (Wharton and Lundquist 2012).

1.3 Doppler Lidar as a tool to study LLJs and the Boundary Layer

Within the past couple decades, Doppler lidars (DLs) have become more accessible and skillful for studying the PBL and for use in wind energy applications. In addition to prototype research lidars that are custom made by individual organizations (e.g., Chanin et al. 1989; Grund et al. 2001), several companies have started making commercially available DLs (e.g., Pearson et al. 2009; Cariou and Boquet 2010; Slinger and Harris 2012) that are being used more widely. In comparison to traditional wind and turbulence sensors such as cup or sonic anemometers, DLs are capable of taking observations over a layer of the atmosphere where scatterers are present. The DLs used herein rely on aerosol backscattering, thus are generally capable of taking measurements in the lowest 1–3 km of the atmosphere where sufficient aerosols are present.

1.3.1 Theory of Operation

Coherent DLs, which are highly utilized herein, transmit pulses of collimated laser radiation into the atmosphere. The radiation is scattered by aerosol and cloud

particles in the atmosphere, some of which is scattered back in the direction of the lidar. This radiation is received by transceiver and processed to estimate radial velocity and attenuated backscatter, respectively based on the Doppler shift and intensity of signal received (Werner 2005).

Using heterodyne detection, the Doppler lidar is able to measure radial velocity with very good precision (typically under 10 cm s^{-1}) (Newsom 2012). Heterodyne detection is performed by mixing the received radiation with light generated by the local oscillator. This mixed signal results in a temporal modulation of the amplitude which oscillates at the frequency difference of the local oscillator and the received signal. The resulting modulation frequency yields the Doppler shift, which can then be used to retrieve radial velocity (Grund et al. 2001). The range of the received signal is related to the time delay between the emission and reception of the pulse.

To collect measurements at different azimuths and elevations, DL laser beams are typically steered using one of two methods. Many of the research-grade, scanning DLs are directed by two-axis mechanically-steering head, which are capable of pointing in any azimuth and elevation. These DLs are capable of many different scanning strategies, which are discussed below. Profiling DLs that were primarily developed for wind-energy applications are directed by a rotating mirror or prism, which can only steer the beam at certain elevation angles and azimuths. These often continuously perform Doppler-beam swinging (DBS) scans that cannot be changed by the user.

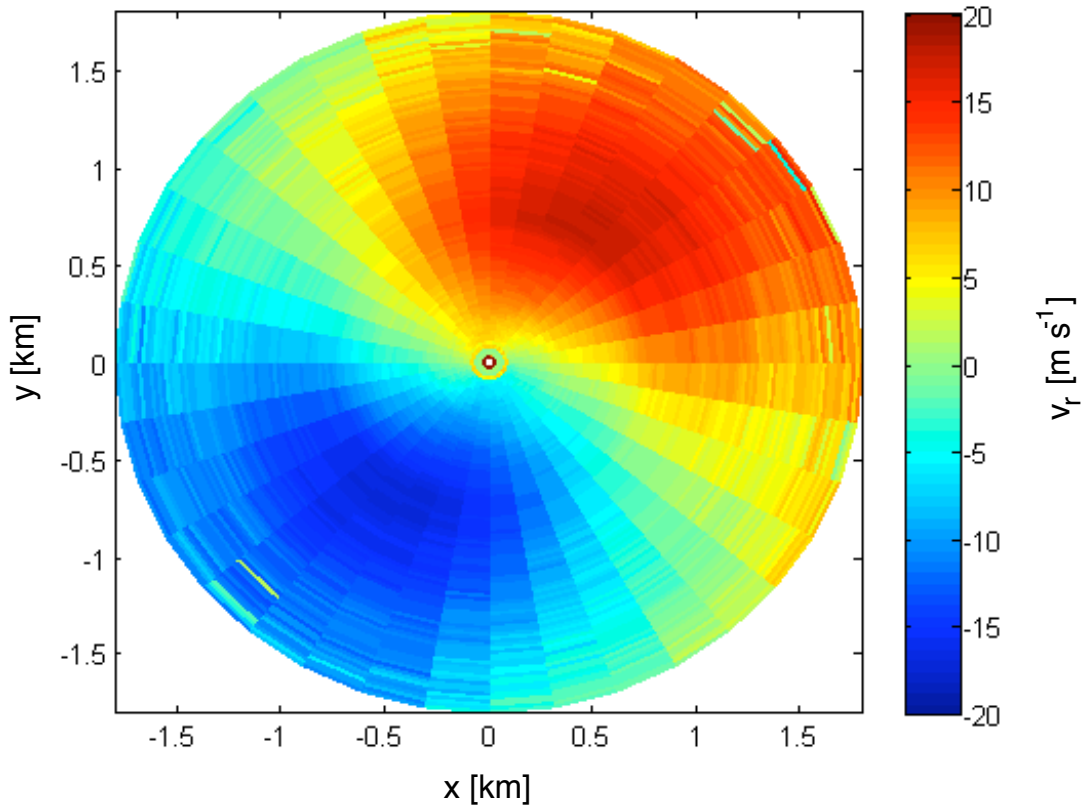

Figure 1.3: An example of a PPI scan during a LLJ.

1.3.2 Common Scanning Strategies

Several of the most common scanning strategies employed by DLs are outlined below, including a discussion of typical applications and quantities measured. In addition to these scanning strategies, several new strategies that are being proposed and utilized to quantify turbulence are discussed within Ch. 2.

1.3.2.1 Plan-Position-Indicator and Velocity-Azimuth-Display

A plan-position-indicator (PPI) scan is very similar to those typically used by operational radars, in that the DL scans across all 360 degrees in azimuth at a predetermined elevation angle. An example of a PPI scan taken during a LLJ is shown

in Fig. 1.3. Depending on the purpose of the scan, the spacing between azimuths varies. With a lower number of azimuths, a faster update-time can be achieved at a lower spatial resolution. PPI scans have been used to examine several different phenomena, through quantification of spatial variability in the radial velocity. Charland and Clements (2013) used PPI scans to calculate divergence and convergence associated with thermal plumes created by wild fires. Käsler et al. (2010) examined how the horizontal extent of wakes created by wind turbines mix and change downstream. Banta et al. (1997) used DL PPIs to show how drainage flows in a valley can both transport and concentrate pollutants. Similarly, Barkwith and Collier (2011) were able to examine how flow varies over complex terrain using PPI scans.

PPI scans can also be used to retrieve wind profiles by using the Velocity-Azimuth-Display (VAD) technique. VAD analysis was initially done using Doppler radar observations to retrieve the wind profile throughout the atmosphere (Browning and Wexler 1968). By assuming that the backscattering aerosols are moving with the flow and that the flow is homogeneous over a scanning circle, the radial velocity is expected to vary sinusoidally over the full 360 degree range. Negative radial velocities (towards the lidar) are expected when the DL is pointed into the mean wind, positive radial velocities (away from the lidar) are measured when the DL is aligned with the mean wind, and radial velocities of zero are when the mean wind is perpendicular to the beam. The VAD technique is used by fitting the radial velocity, v_r, to

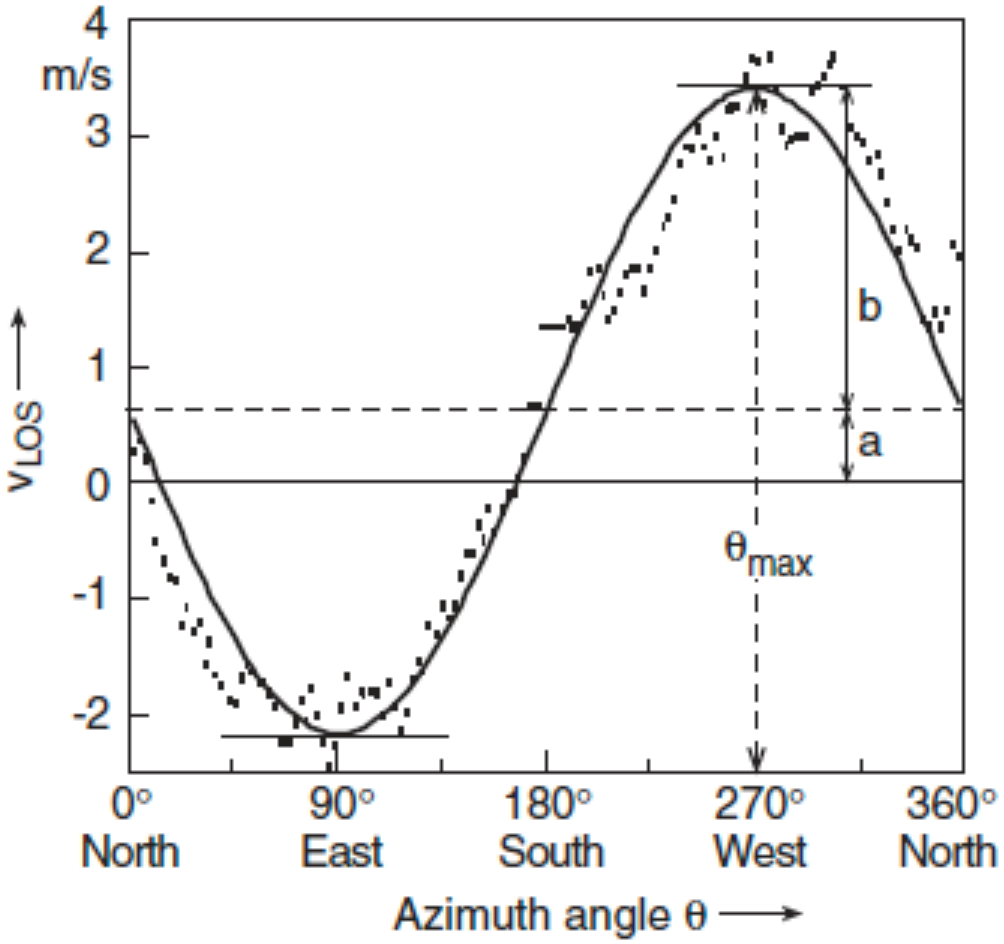

Figure 1.4: An example of a VAD fitting to observed v_r (V_{LOS} on his plot), from Werner (2005).

$$v_r = a + b\cos(\Theta - \Theta_{max}), \tag{1.1}$$

where a is the offset, b is the amplitude, Θ is the azimuth angle, and Θ_{max} is the phase shift. The components of the wind u, v, and w can then be calculated by the equations

$$u = -b \sin \Theta_{max} / \cos \Phi \tag{1.2}$$

$$v = -b \cos \Theta_{max} / \cos \Phi \tag{1.3}$$

$$w = -a / \sin \Phi, \tag{1.4}$$

where Φ is the elevation angle above the horizon. An example of the VAD fitting is provided in Fig. 1.4. VAD analysis is performed for every range gate from a PPI scan to retrieve the mean wind at different heights. This yields a vertical wind profile.

1.3.2.2 Doppler-Beam Swinging

There are several different variations of the DBS scanning strategy, all of which are similar to the VAD technique with a few key differences. DBS scans typically only use 3–5 beams, where each beam is an individual measurement at a distinct azimuth and elevation. In comparison, VAD scans usually use an order of magnitude more beams. Of those 3–5 beams, one beam typically points at zenith to take a direct measurement of w over the lidar. The other beams are taken at slightly off-zenith angles, typically directed to either two or four of the cardinal directions (either N/E or N/E/S/W). For one variation of the DBS where 3 beams are used, the three components of the wind can be calculated

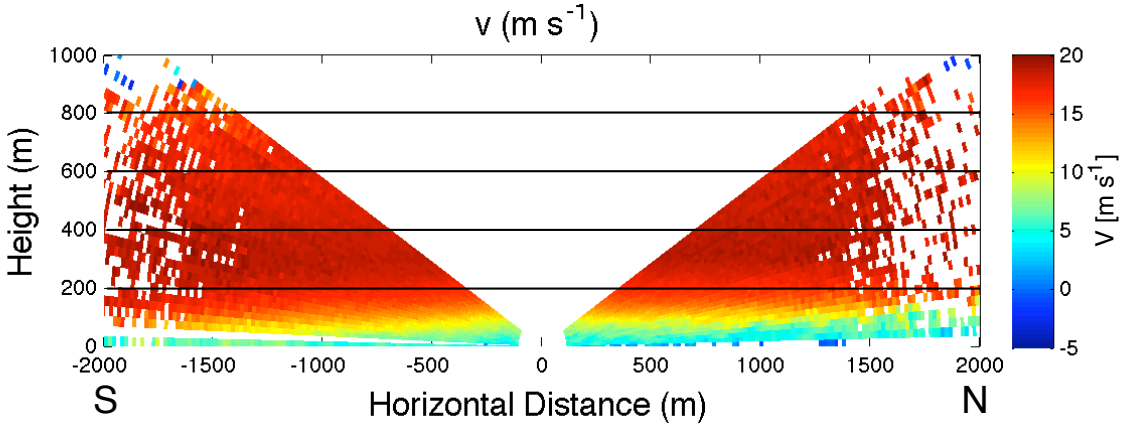

Figure 1.5: An example of an RHI scan that was performed on the roof of the National Weather Center on 7 August 2013. Values of v_r were converted to the v component of the wind by assuming w to be zero.

$$u = -(v_{r2} - v_{r1}\sin\Phi)/\cos\Phi \tag{1.5}$$

$$v = -(v_{r3} - v_{r1}\sin\Phi)/\cos\Phi \tag{1.6}$$

$$w = -v_{r1}, \tag{1.7}$$

where $v_{r1,2,3}$ are the radial velocities respectively from a vertical, east, and north beam. Srinivasa Rao et al. (2008) discuss in more detail the various beam configurations that can be used in the DBS technique.

1.3.2.3 Range Height Indicator

Range height indicators (RHIs) are conducted by scanning at small increments in elevation, typically beginning on the horizon, at a selected azimuthal angle. Consecutive RHIs are very useful for investigating how features evolve over time, or studying how the flow changes in height with respect to roughness elements or

terrain changes. For example, Iwai et al. (2011) studied the evolution of a sea-breeze as it approached the location of a DL through consecutive RHIs over a period of time. During a campaign in Oklahoma City, Wang et al. (2007) showed that wake vortices often developed in the lee of an individual tall building when strong LLJs occurred. Gravity waves that were generated by the LLJ during the morning transition period were visible within RHI scans (Wang et al. 2013). An example of an RHI scan taken on the roof of the National Weather Center (NWC) is shown in Fig. 1.5, where it appears that the LLJ increases with height as it approaches the NWC and the city of Norman at large.

1.3.2.4 Vertical Stares

In addition to the above-mentioned scanning strategies, many DLs simply measure w by pointing vertically for periods of time as a part of a scanning schedule. An example of measurements collected during vertical stares is shown in Fig. 1.1, where the top of the CBL is clearly visible as the layer where mixing quickly decreases with height. These measurements allow for quantification of turbulence that can be used to estimate a wide variety of fundamental PBL parameters such as PBL depth. A thorough discussion of the applications of these measurements, and corrections that need to be made due to instrument error and limitations, is provided in Ch. 2.

1.4 Open Research Questions to be Addressed

Three general open research questions are addressed in the following chapters. The questions, along with a brief description of how they are answered throughout the rest of the paper, are outlined below. Each of the following three chapters are written as independent standalone journal articles, which have been or are planned to be submitted to peer reviewed journals.

1. How accurate are DL-derived estimates of vertical velocity variance, and can these estimates be improved?

2. Can vertical velocity variance measurements from the DL be used to confirm or improve the classification of the nocturnal SBL as either weakly stable or very stable? How do the properties (i.e., turbulence, thermodynamic, velocity) within these subtypes of SBLs vary in time and height?

3. How do LLJs themselves evolve under differing turbulence regimes? Do the LLJs have different features, or are driven by different mechanisms, under these different regimes?

Previously, DL vertical velocity variance measurements have not been carefully compared with those from in-situ observation. Through these comparisons, DL measurements can be validated and techniques for correcting the measurements for errors can be improved. To enable such comparisons, a measurement campaign occurred at the Boulder Atmospheric Observatory in Erie, CO, where

two DLs were deployed next to a 300-m tower instrumented with sonic anemometers on several levels. Vertical velocity variance estimates computed from vertical stares are compared with similar measurements from the sonic anemometers. An autocovariance technique to remove noise from the returned signal in the DL observations, discussed by Lenschow et al. (2000), is evaluated to determine its effectiveness under different conditions. The effect of time averaging on variance values is also assessed, by comparing averaged and raw sonic data. These results are presented within Ch. 2.

Differentiating characteristics of the nocturnal SBL are not well-known. Additionally, a lack of high spatial- and temporal-resolution turbulence and thermodynamic measurements above typical tower height (10-m) have limited the current understanding of the evolution and structure of the NBL. To address this, a two-month experiment was conducted at the ARM SGP site in rural north-central Oklahoma near Lamont, for which the University of Oklahoma brought several complementary instruments including a DL. During the experiment in the autumn of 2012, many different synoptic weather conditions occurred, resulting in vastly varying structures of the nocturnal SBL. Wind, turbulence, and thermodynamic profiles from several instruments are combined together to examine how the SBL distinctly evolves, in both time and in height, under the different turbulent regimes. Composite profiles of these quantities, created for each turbulence regime that is found, are presented within Ch. 3.

Within previous LLJ climatologies and studies, all LLJs regardless of the intensity of mixing are generally not differentiated. Since the structure and evolution of the nocturnal SBL differs greatly depending on the turbulence intensity, it is expected that characteristics of the LLJ should vary based on these conditions. During the aforementioned two-month experiment at the ARM SGP site, LLJs of varying magnitude developed on most nights. The LLJs are generally grouped into the two main turbulence regimes that are discussed within Ch. 3, with LLJs in each category having different characteristics and evolutions overnight. Several case studies of LLJs within each turbulence regime are presented, for which both the time-evolution of the LLJ and the synoptic setup are discussed. Additionally, overall differences in the overnight evolution of the LLJs associated with each turbulence regime are shown, including a discussion for why these differences occur. These results are presented in Ch. 4.

Chapter 2

The Accuracy and Improvement of Vertical Velocity Variance Measurements from Doppler Lidars

2.1 Background

Various scanning strategies and measurement methods have been used to quantify turbulence characteristics from DL observations. Sathe and Mann (2013) summarize the state-of-the-art DL turbulence measurement techniques and limitations with current observations, several of which are briefly described here. Velocity structure function can be calculated longitudinally along the beam or transversely across azimuths in sector PPI scans (e.g., Frehlich and Cornman 2002; Krishnamurthy et al. 2011; Davies et al. 2004). Values of the horizontal wind variance (σ_u^2 and σ_v^2) can be calculated from range height indicator scans, by first separating the measured velocity into height bins and calculating the variance in velocity at each height (e.g., Banta et al. 2006; Pichugina et al. 2008). A novel six-beam technique proposed by Sathe et al. (2015) can be used to calculate all six terms within the Reynold's stress tensor.

Quantifying vertical velocity variance σ_w^2 and the vertical velocity spectra is one of the simplest and most direct measurements of turbulence that is possible, and this method has been used in many studies (e.g., Hogan et al. 2009; Lothon

et al. 2009; Barlow et al. 2011; Shukla et al. 2014). For this measurement, the DL simply points at zenith and continually collects measurements of the vertical velocity w, over which σ_w^2 and w spectra can be calculated at every range gate over a user-defined time interval.

Measurements of σ_w^2 and other statistics of w, calculated using observations when a DL is directed at zenith, are often used to derive other important planetary boundary layer (PBL) variables. Sensible and latent heat fluxes can be retrieved using σ_w^2 and w skewness profiles (Gal-Chen et al. 1992; Davis et al. 2008; Dunbar et al. 2014). The mixing height can be determined from profiles of σ_w^2 as the height where σ_w^2 decreases below a threshold value of approximately 0.1 m^2 s^{-2}, but may depend on aerosol loading and other conditions (Pearson et al. 2010; Barlow et al. 2011). Integral time and length scales, which are critical parameters for turbulence schemes within numerical models, can be calculated from the autocorrelation of w (Lenschow et al. 2000; Lothon et al. 2006). Eddy dissipation rate ε can be estimated from the spectrum of w (O'Connor et al. 2010). With all of these above variables being calculated from observed fluctuations of w, it is important to assess the accuracy of DL w measurements and their derived statistics.

The mean wind speeds computed from DL VAD or DBS scans have been shown to compare well to those from anemometers, radiosondes, and radar wind profilers (Smith et al. 2006; Päschke et al. 2014). However, few previous studies have performed an in-depth comparison of turbulence statistics derived from DL measurements with those from in situ sensors such as sonic anemometers, and

discuss possible corrections for DL measurements to improve their accuracy. In comparison to sonic anemometers, the sampling volume and averaging time of DLs is large ($\sim$ 20 m and 1 s), and therefore unable to resolve smaller scales of turbulence. A diagram to show these effects is provided in Fig. 2.1. Additionally, DL data can be noisy when aerosol loading and the signal-to-noise ratio (SNR) are small. These effects have opposite effects on computed higher-order statistics such as σ_w^2, as noise increases computed σ_w^2 and resolution volume effects reduces the values of σ_w^2 measured by the DL compared to the true atmospheric variance. Barlow et al. (2011) compared the standard deviation of w, σ_w, with those from a sonic anemometer and found that the sonic anemometer generally observed larger values due to the higher sampling frequency. When the sonic anemometer data were averaged to match the frequency of the DL observations, the values of σ_w from the DL and sonic anemometer were in better agreement, but considerable scatter still existed. Fuertes et al. (2014) used measurements from three synchronous DLs to compute the three-dimensional wind vector at 0.5 Hz for comparisons with sonic anemometer measurements, and showed that the DL and sonic measurements were in agreement when the sonic observations were filtered and downsampled.

Both Barlow et al. (2011) and Fuertes et al. (2014) highlight that DLs are incapable of resolving turbulence on small spatial and temporal scales, as shown in Fig. 2.1, but do not offer corrections for these limitations in the DL measurements. Hogan et al. (2009) attempts to correct for underestimates of σ_w^2 by extrapolating the power spectrum out to higher frequencies that cannot be resolved by the DL,

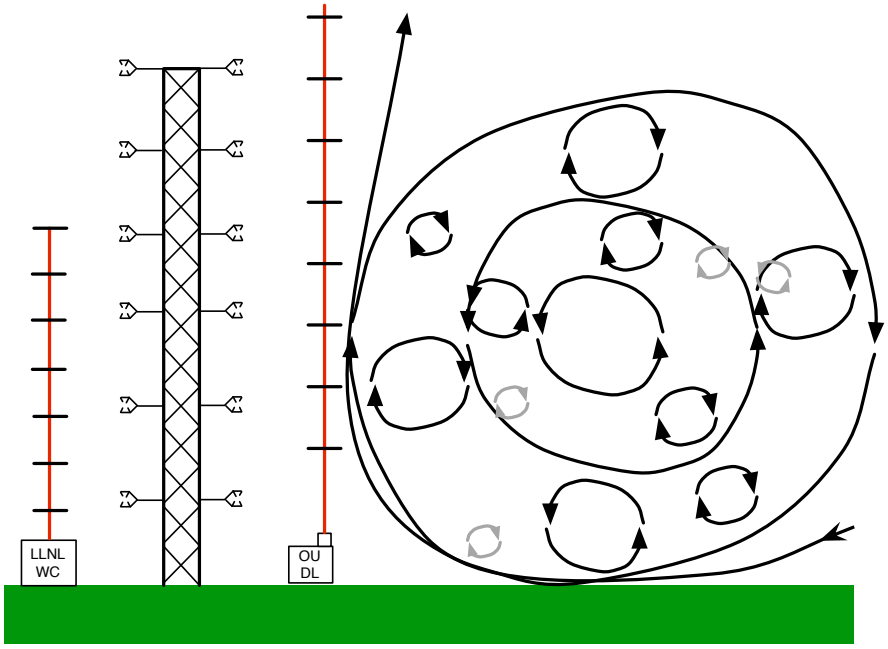

Figure 2.1: Diagram showing various scales of turbulence compared to the resolution volumes of the DL and sonic anemometers on the tower. DL beam is denoted by red line, and range gates by black line segments over it. The DL is able to resolve many of the larger turbulent eddies, but vertical velocities associated with eddies smaller than the range-gate size, such as those shown in grey, cannot be resolved. Many of the smaller eddies may be captured by the sonic anemometer, since their resolution volume is much smaller than the DL. Image is not to scale.

but does not have sonic anemometer measurements for which these corrected DL σ_w^2 values can be compared. While this method may correct for the inability of DLs to capture smaller scales of turbulence, it is not able to be used to remove noise that can be present in DL observations when SNR is low. Herein, we propose to use the autocovariance method discussed by Lenschow et al. (2000) to correct for the effects of both noise and the resolution volume to accurately determine the value of variance along the radial velocity, in this case σ_w^2 since the beam is vertical. Lenschow et al. (2000) originally proposed this method as a means of measuring higher-order moments in noisy data, and will be discussed in detail in Sect. 2.3.

Few studies compare lidar-derived statistics that utilize the autocovariance method with in situ measurements. Turner et al. (2014a) has compared Raman lidar estimates of water vapour variance and skewness with those from aircraft observations and showed general agreement in the profile shape, but significant differences in the observations were also apparent. Some disagreement in the measurements was partially attributed to sampling differences. Lenschow et al. (2012) compared normalized profiles of DL-derived vertical velocity variance, skewness, and kurtosis with those from other experiments and found generally good agreement. However, higher-order statistical values were not directly compared with other in situ observations.

Herein, we provide the first in-depth analysis of the applicability of the autocovariance method of retrieving variance values. DL measurements and derived estimates of σ_w^2 are directly compared with those from sonic anemometers to address the following questions:

1. How many lags should be used when applying the autocovariance method? How does the number of lags used affect the accuracy of the derived statistics?

2. What scales of turbulence can DLs explicitly resolve? Can the autocovariance technique be used to correct for the limitations of time and volume averaging?

3. How robust are DL-derived estimates of vertical velocity variance, and how does the accuracy of these change with height and for different stability regimes?

The structure of the paper is outlined here. A description of the instrumentation used and experiment, including weather conditions during the measurements, is provided in Sect. 2.2. The autocovariance technique and the ideal number of lags used in its application is described in detail in Sect. 2.3. Comparisons of DL and sonic anemometer measurements and derived statistics are presented within Sect. 2.4. Potential additional applications of this technique and the need for other intercomparison studies are discussed in Sect. 2.5. A summary and the main conclusions are provided in Sect. 2.6.

2.2 The Lower Atmospheric Thermodynamics and Turbulence Experiment

Measurements used here were collected during the Lower Atmospheric Thermodynamics and Turbulence Experiment (LATTE), which was conducted at the Boulder Atmospheric Observatory (BAO) from 10 February to 28 March 2014 with a small extension to 28 April 2014. The BAO is located 25 km east of the foothills of the Rockies within gently rolling terrain near Erie, CO, USA. The BAO has a suite of permanently and semi-permanently installed meteorological and boundary-layer instruments, such as sodars, a ceilometer, and temperature, humidity, ozone, and wind sensors on a 300-m tower. More complete details of the BAO facility and the surrounding terrain are discussed by Kaimal and Gaynor

(1983). In addition to these permanently installed instruments, several DLs and an unmanned aerial system were deployed at the site by Lawrence Livermore National Laboratory (LLNL) and the University of Oklahoma (OU). Additionally, the National Center for Atmospheric Research (NCAR) deployed a new 449-MHz wind profiler (see Lindseth et al. 2012) at the site for validation of wind and reflectivity measurements.

One of the primary objectives of LATTE was to measure and validate PBL three-dimensional turbulence fields with multiple Doppler lidars, sonic anemometers, an unmanned aerial system, and radar. Several different DL scanning strategies outlined in Sect. 2.1 were tested for comparison of turbulence measurements with those collected from sonic anemometers. Herein, we focus on measurements taken during a two-day period from 26 March to 28 March, when two DLs were placed within two metres of the sonic anemometer booms on the 300-m tower. Since these measurements are in so close proximity with each other, vertical velocity statistics calculated from the DL measurements can be directly compared with those from sonic anemometers. A summary of the instruments, which are discussed in more detail below, used within this study is provided in Table 2.1.

2.2.1 Bolder Atmospheric Observatory Tower

The 300-m BAO tower is permanently instrumented with cup anemometers, temperature, humidity, and ozone sensors at 10-, 100-, and 300-m on booms extending to the southeast (154°) of the tower. In addition to these measurements, six

Table 2.1: Overview of all instruments and their properties that are used here.

Instrument	Measurement Heights	Sampling Rate	Owner	Boom
RM Young 3-D Sonic Anemometers	50, 100, 150, 200, 250, 300 m	30 Hz	OU	North-west
Campbell Scientific CSAT3 3-D Sonic Anemometers	50, 100, 150, 200, 250, 300 m	60 Hz	NCAR	South-east
Halo Streamline Pro Doppler Lidar	99 m–9.6 km 18-m range gates	0.7 Hz	OU	South-east
WindCube v2 Doppler Lidar	40-200 m 12 measurement heights 20-m range gates	0.25 Hz for vertical beam	LLNL	North-west

sonic anemometers were temporarily installed on booms on both the southeast and northwest (334°) side of the tower. The sonic anemometers were equally spaced every 50-m in height, with the lowest mounted at 50-m and the highest at the top of the tower at 300-m. Six RM Young 3-D sonic anemometers provided by OU were installed on the northwest booms, and these sampled at 30 Hz. NCAR provided the Campbell Scientific 3-D sonic anemometers, which sampled at 60 Hz, that were installed on the southeast booms. With instrumentation on opposite sides of the tower, measurements that are not affected by the wake are always available from sonic anemometers on the upwind side of the tower. For all of the results presented here, observations only from the NCAR Campbell Scientific sonic anemometers will be utilized, as significant differences in vertical velocity statistics, shown in

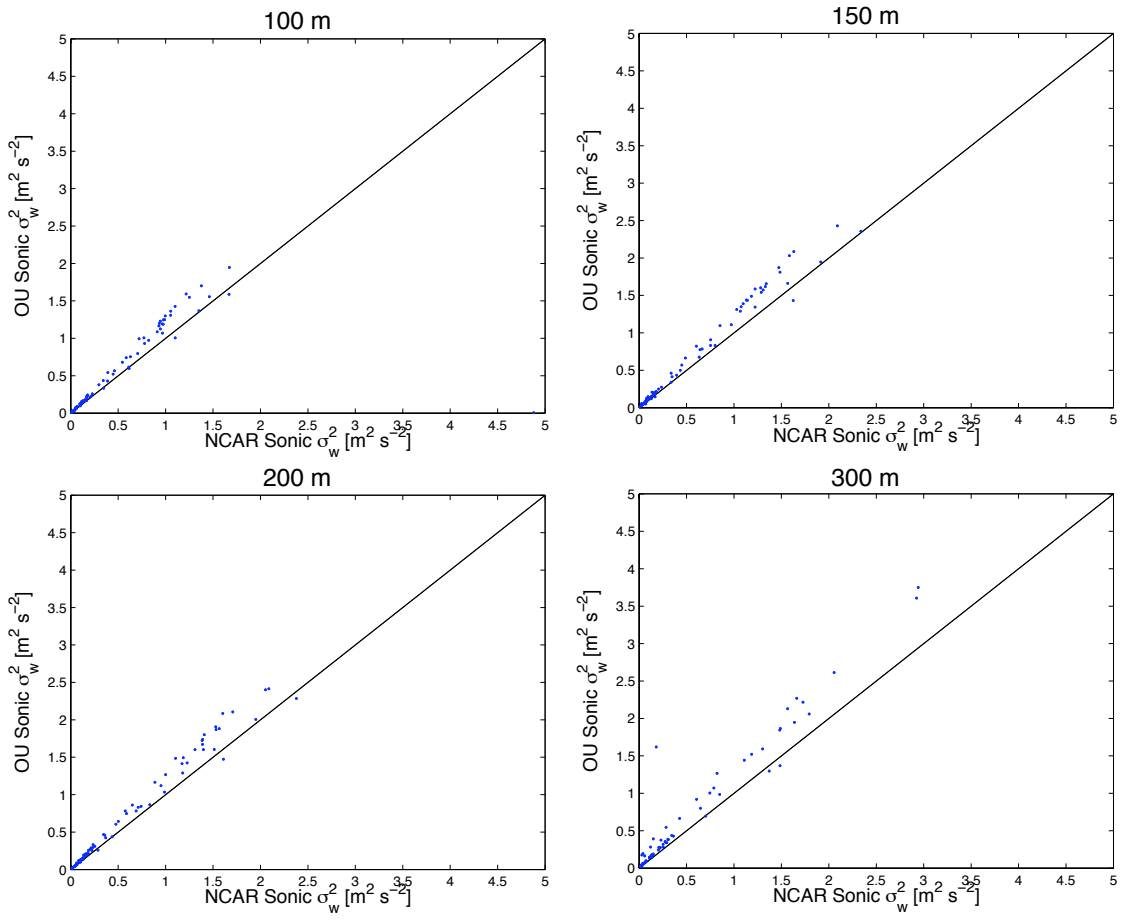

Figure 2.2: Comparison of vertical velocity variance from the OU RM Young and NCAR Campbell Scientific sonic anemometers at various heights. Black line denotes a 1-to-1 agreement. Measurements are only shown when both sonic anemometers are not waked by the 300-m tower.

Fig. 2.2, are apparent between the two models. Based on the design of these instruments, the Campbell Scientific anemometer appears better able to accurately measure *w*, since the RM Young sonic anemometers have large vertical shafts that may alter the flow that would particularly affect the *w*-component. A spike filter was used to remove erroneous measurements, in which data points that were farther than three standard deviations of the mean, calculated over 30-min windows, were removed. The highest frequency data available were used (60 Hz for NCAR sonic anemometers), unless otherwise noted.

2.2.2 Doppler Lidars

Two DLs, a LLNL WindCube v2 (henceforth LLNL WC) and an OU Halo Streamline Pro (henceforth OU DL), were deployed next to the base of the 300-m tower from 26 March to 28 March. The LLNL WC was situated to the northwest of the tower, while the OU DL was deployed southeast of the tower. The DLs were located a few metres from the ends of the booms on the tower so that the beam would not be obscured.

2.2.2.1 OU Halo Streamline Pro

The OU DL uses a pulsed, heterodyne 1.5 μm laser to detect backscattered energy from aerosols within the atmosphere and determine their velocity along the radial. The range gate size is user-adjustable, with a minimum spacing of 18-m that was used during this portion of LATTE. The smallest range gate spacing of 18-m was chosen to minimize the effects of volume averaging. The focus was set at 300 m, which is the minimum possible focus length, so that generally the largest SNR and highest-quality data are at that height. Since the aerosol content of the air was generally low during the experiment, as predominantly westerly winds advected clean air over the BAO site, the noise in the measurements tends to increase significantly for measurements closer to the surface and farther from the focus height. Details about the Halo Streamline Pro hardware, specifications, and theory of operation can be found in Pearson et al. (2009).

2.2.2.2 LLNL WindCube v2

The LLNL WC was designed primarily for wind energy applications, and thus continuously conducts DBS scans for retrieval of horizontal winds within the lowest 200 m of the atmosphere. The DBS scan consists of consecutive beams off-zenith pointing north, east, south, west, and followed by a vertically pointing beam. The vertical velocity component w is directly measured by the vertical beam, and the only dataset from the LLNL WC that is used within this analysis. Independent measurements of w from the vertical beam are available approximately every 4 s. The range gate size is 20 m, which is slightly larger than that for the OU DL. Typically during LATTE, the SNR values from LLNL WC measurements are largest at 50 m and decrease with height, thus the highest-quality measurements are closer to the surface than those from the OU DL.

2.2.3 Meteorological Conditions

To document the general meteorological conditions, mean temperature, wind speeds, and bulk Richardson number (Ri) at three heights during the two-day period when the DLs were located next to the towers are shown in Fig. 2.3. The value of Ri, which is used as a proxy for stability, is calculated as

$$\mathrm{Ri} = \frac{\frac{g}{\theta}\frac{\Delta\theta}{\Delta z}}{\frac{\Delta V^2}{\Delta z^2}}, \tag{2.1}$$

where g is gravity, θ is the potential temperature, $\Delta\theta$ is the difference in temperatures between the measurement height and that at 10-m, Δz is the difference in

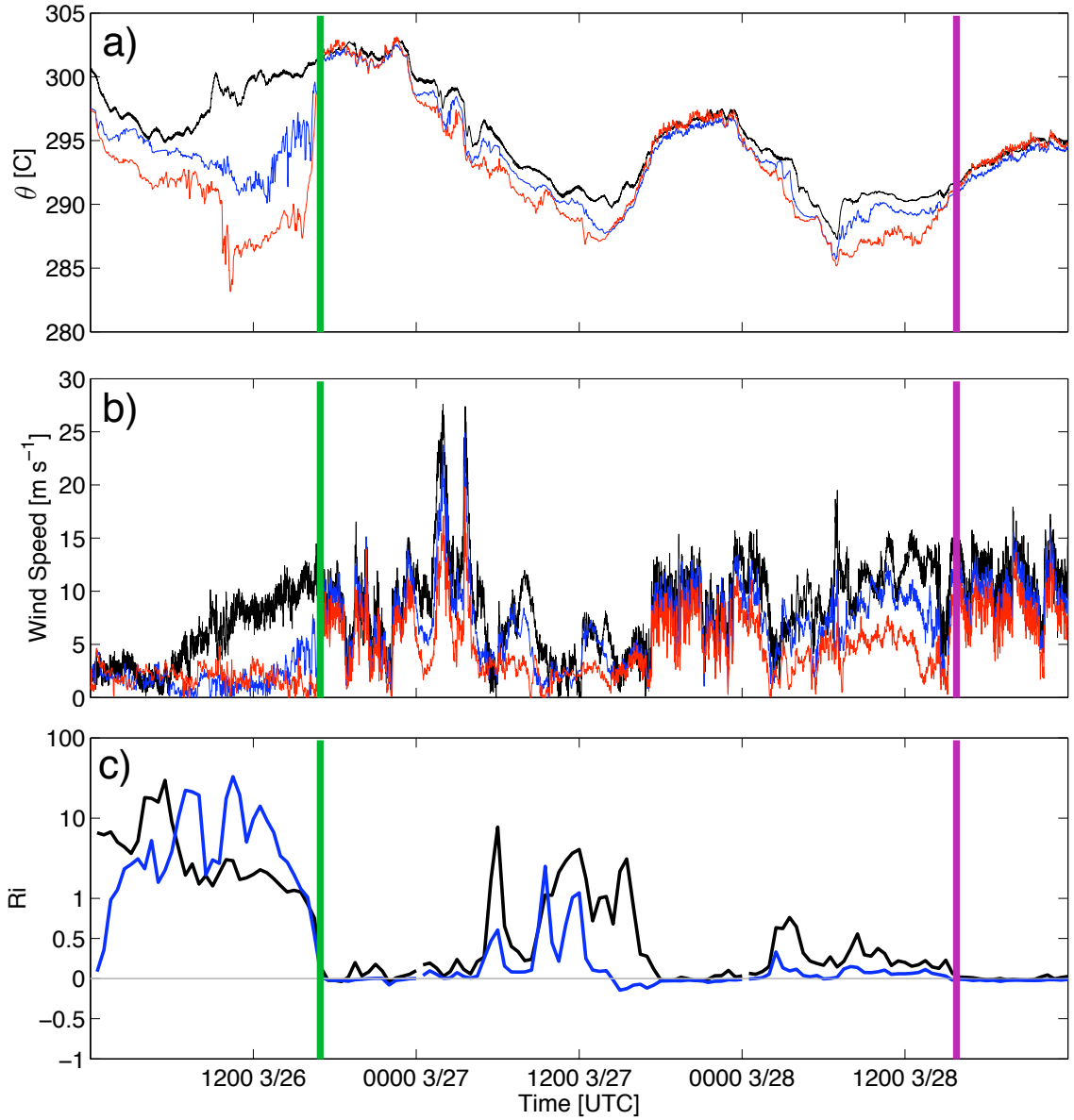

Figure 2.3: Evolution θ (a), wind speed (b), and Ri (c) over the two-day observational period from 26 to 28 March, 2014. The colours indicate the height of the measurement on the BAO tower, for which red is 10-m, blue is 100-m, and black is 300-m. Thick green lines denotes when DLs were setup and began operating near the tower, while the magenta lines indicate the end of this observational period.

height between the measurements, and ΔV is the wind speed at the height that Ri is calculated, which assumes that the surface wind speed is zero.

During a significant portion of the observational period, the wind speed in the lowest 300-m was relatively large, being greater than 5 m s^{-1}. This generally prevented a strongly stable layer from forming during the nighttime hours of 27 and 28 March, as the inversion on both of the nights is much less than that found on 26 March. Thus, during this campaign, few observations are available during strongly stable conditions when Ri is greater than 1, except for a few time periods around 1200 UTC on 27 March. Particularly strong winds occurred around 0300 UTC on 27 March. Since the wind direction was westerly (not shown), these were likely associated with downsloping flow on the lee of the mountains transporting down higher momentum from higher in the troposphere that often occur in the area (e.g., Brinkmann 1974).

2.3 Correction of Lidar Variance Values

Lenschow et al. (2000) discusses a methodology of estimating second- through fourth-order moment values within noisy measurements, with a focus on observations taken by various types of lidars. This technique has been used in numerous studies to estimate second- and higher-order moments of water vapour from Raman lidars and Differential Absorption lidars (DIALs) (e.g., Machol et al. 2004; Wulfmeyer et al. 2010; Turner et al. 2014a,b), temperature from Raman lidar (e.g., Behrendt et al. 2014), ozone from a DIAL (e.g., Machol et al. 2009; Alvarez et al.

2011), velocity from Doppler lidars (e.g. Grund et al. 2001; Tucker et al. 2009), and it was also extended to correct eddy-covariance flux measurements of trace gases (e.g., Mauder et al. 2013; Peltola et al. 2014). While this methodology has been used within many studies, to the author's knowledge there are no in-depth comparisons of variance estimates of any quantity measured by a lidar to those from in situ observations, such as to sonic anemometers or fast-response thermistors. Herein, we evaluate the applicability of this methodology to extract accurate variance estimates from lidar measurements.

2.3.1 Overview of Method

The method described by Lenschow et al. (2000) to obtain turbulence statistics in noisy data are outlined here. The second-order autocovariance function (M_{11}) of a stationary time series is defined as

$$M_{11}(t) = \overline{(w' + \varepsilon')(w'_t + \varepsilon'_t)}, \tag{2.2}$$

where $w(t)$ is a correlated variable (herein, specifically vertical velocity), ε is contamination from random white noise, t is the time-lag, and primes denote deviations from the mean. If the noise is uncorrelated, as is expected with lidar measurements, the cross terms become small and negligible, thus at a lag of zero

$$M_{11}(0) = \overline{w'^2} + \overline{\varepsilon'^2}. \tag{2.3}$$

This relationship shows that the measured variance by the lidar $M_{11}(0)$ is the result of both the true atmospheric variance $\overline{w'^2}$ and the noise variance in the returned signal $\overline{\varepsilon'^2}$. By assuming that $\overline{w'^2}$ is largely due to isotropic turbulence within the inertial subrange (Monin and Yaglom 1979), which is generally true within the PBL except when gravity waves are present, the expected M_{11}^* is

$$M_{11}^*(t) = \overline{w'^2} - Ct^{2/3}, \tag{2.4}$$

in which C is a parameter related to eddy dissipation since w is a component of the velocity. Henceforth, the fitting of Eq. 2.4 will be referred to as the 'structure function fitting', as the 2/3-power within Eq. 2.4 ultimately stems from Kolmogorov's structure function (Kolmogorov 1941). By treating both $\overline{w'^2}$ and C as unknowns and fitting M_{11}^* to the observed M_{11} at lags within the inertial subrange, estimates of $\overline{w'^2}$ and $\overline{\varepsilon'^2}$ can be made wherein

$$\overline{w'^2} = M_{11}^*(0) \text{ and} \tag{2.5}$$

$$\overline{\varepsilon'^2} = M_{11}(0) - M_{11}^*(0). \tag{2.6}$$

Using this relationship implicitly requires that Taylor's frozen hypothesis is valid (Taylor 1938), which assumes that turbulent eddies do not evolve over time as they pass through the resolution volume.

2.3.2 Number of Lags for Fitting

For the most accurate and robust estimates of variance or higher-order moments, the proper number of lags to use for the fitting is not well-known or trivial. Within many studies in which this method is used, the number of lags used is either not discussed or a seemingly arbitrary number of lags that the authors determined were within the inertial subrange is used (e.g. Lenschow et al. 2000; Wulfmeyer et al. 2010). Previously, the longest lagtime (τ_{max} below) used within the fitting ranges from 12.5 s (e.g., McNicholas and Turner 2014) to over 100 s (e.g. Behrendt et al. 2014). Ideally, the smallest lag used in the fitting should correspond to the time scale at which contributions to M_{11} from turbulent eddies that cannot be explicitly resolved become negligible. The largest lag to be used should be within the inertial subrange, but not so long that frozen turbulence cannot be safely assumed. The total number of lags used should be enough that an accurate and representative fitting can be ensured.

Here, we define the ideal lags to use in the fitting based on the resolution of the instrument and turbulence characteristics. Since the smallest lag is related to the time scales of the turbulent eddies that cannot be resolved by the lidar, we define the smallest lag τ_{min} to be

$$\tau_{min} = \frac{\Delta r}{V}, \tag{2.7}$$

where Δr is the size of the range gate or resolution volume and V is the mean wind speed. Assuming that turbulence is isotropic, this ensures that τ_{min} is large

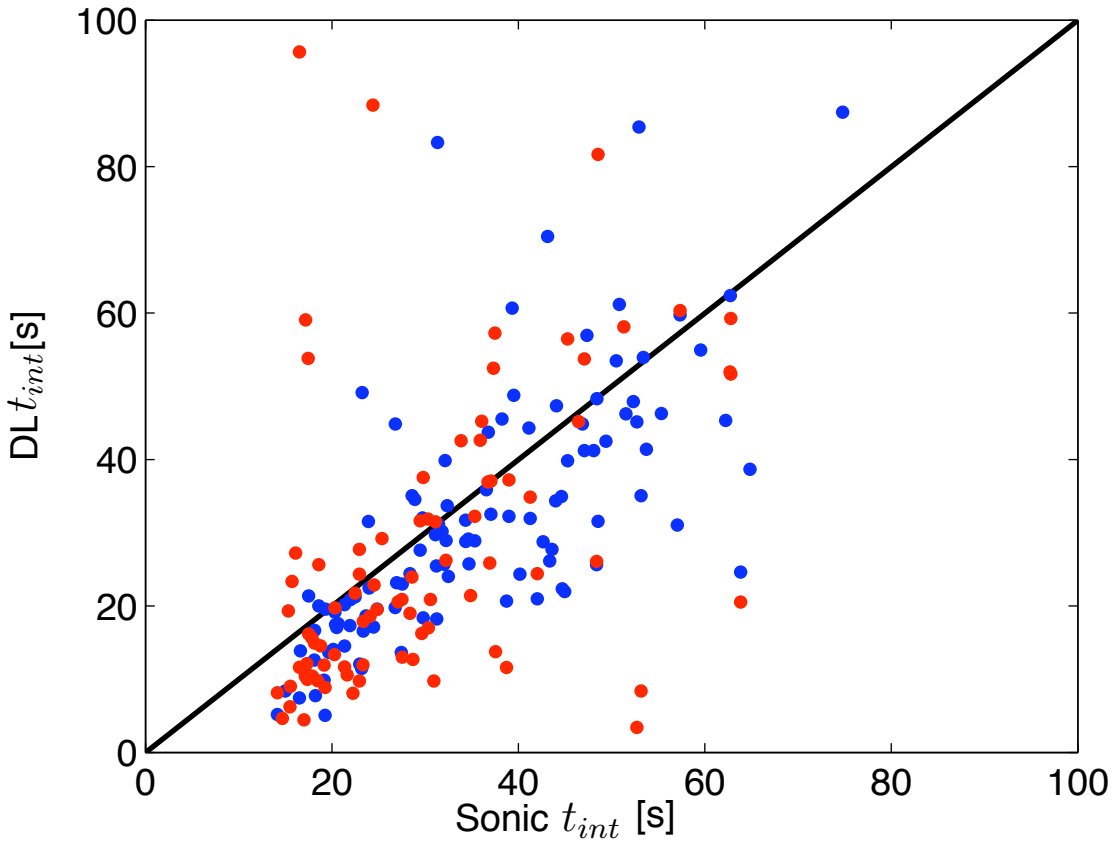

Figure 2.4: Comparison of t_{int} as calculated from the sonic anemometer and DL M_{11} values, using Eq. 2.9. Red shows values calculated from LLNL WC measurements, and blue shows those calculated from the OU DL observations.

enough that eddies of the same size or smaller than the resolution volume, which lead to underestimates of the true M_{11} at short lags, will not negatively affect the fitting. Within this study, the maximum value of τ_{min} is set to 8 s for time periods when the wind speed is small. This maximum for τ_{min} is somewhat arbitrary, but a maximum value is needed since $\tau_{min} \rightarrow \infty$ as $V \rightarrow 0$. Since the evolution of turbulent structures becomes significant for larger lag times (Higgins et al. 2013), this limit for τ_{min} is a compromise between minimizing the effects of both volume averaging and time evolution of turbulence.

We define the largest lag τ_{max} to use as

$$\tau_{max} = \min\left(\frac{t_{int}}{2}, t\left(M_{11}(t) = \frac{M_{11}(0)}{2}\right)\right), \tag{2.8}$$

where t_{int} is the integral time scale and τ_{max} is the minimum of the two possible values. Values of t_{int} are defined as

$$t_{int} = \frac{1}{\overline{w'^2}} \int_0^{t(M_{11}=0)} M_{11}(t)dt, \tag{2.9}$$

wherein $\overline{w'^2}$ is $M_{11}^*(0)$, and both t_{int} and $\overline{w'^2}$ are both iteratively solved. Values of t_{int} calculated from the DL observations compared with those calculated from sonic anemometer measurements are shown in Fig. 2.4. Generally, the values of t_{int} calculated from the OU DL are in better agreement with those derived from anemometer measurements than those from the LLNL WC. This is likely due to the higher sampling rate of the OU DL, therefore the time between lags (dt) is shorter in the numerical integration. Considerable scatter is evident in the estimates of t_{int}, which is due to the differences in the values of M_{11} at various lags that is discussed within Sect. 2.4.3.

Under convective conditions, generally $\tau_{max} = \frac{t_{int}}{2}$. However, under more stable conditions, t_{int} often becomes much larger than the typical time scales within the inertial subrange due to the small value of $\overline{w'^2}$. Under these conditions, the time at which $M_{11} = \frac{M_{11}(0)}{2}$ is used for τ_{max} instead. If the conditions are such that τ_{min} is greater than τ_{max}, such as in the stable boundary layer with weak winds, then τ_{max} is set to be one lag more than τ_{min}. Using this method for such time periods when the integral time scale is not explicitly resolved is not ideal since values of

M_{11} are not accurately modeled by Eq. 2.4. However, as shown in Sect. 2.4.4, this method generally improves estimates of σ_w^2 during this time periods by removing noise, albeit the lidar σ_w^2 estimates are often smaller than the true atmospheric variance. Typical values of τ_{min} and τ_{max} that were used during LATTE are shown in Table 2.2.

When using this method to determine the value of $\overline{w'^2}$ and $\overline{\varepsilon'^2}$, it is expected that $M_{11}^*(0)$ (i.e., $\overline{w'^2}$) is less than $M_{11}(0)$, and that $\overline{\varepsilon'^2}$ is the positive difference of $M_{11}(0)$ and $\overline{w'^2}$. An example of this is shown in Fig. 2.5a, where the fitting of Eq. 2.4 leads to a smaller estimate of $\overline{w'^2}$ than M_{11} at lag zero. However, we observe that under periods of strong turbulence and high SNR, estimates of $\overline{w'^2}$ can be greater than $M_{11}(0)$ as shown in Fig. 2.5b. Using the definition in Eq. 2.6, values of $\overline{\varepsilon'^2}$ are negative in these cases, which is physically impossible since $\overline{\varepsilon'^2}$ in the signal is always positive or zero. To our knowledge, this behaviour has not been discussed in any previous studies. We attribute this 'negative error' to volume-averaging effects, where the smaller scales of turbulence cannot be properly captured by the DL, when the true noise in the measurements is low. The accuracy of the fitting under conditions when $M_{11}^*(0)$ is both greater and less than $M_{11}(0)$ is discussed in Sect. 2.4 through comparison with sonic anemometer measurements.

Numerous studies discuss the importance of considering the averaging time when measuring turbulence statistics (e.g. Lenschow et al. 1994; Mahrt 1998;

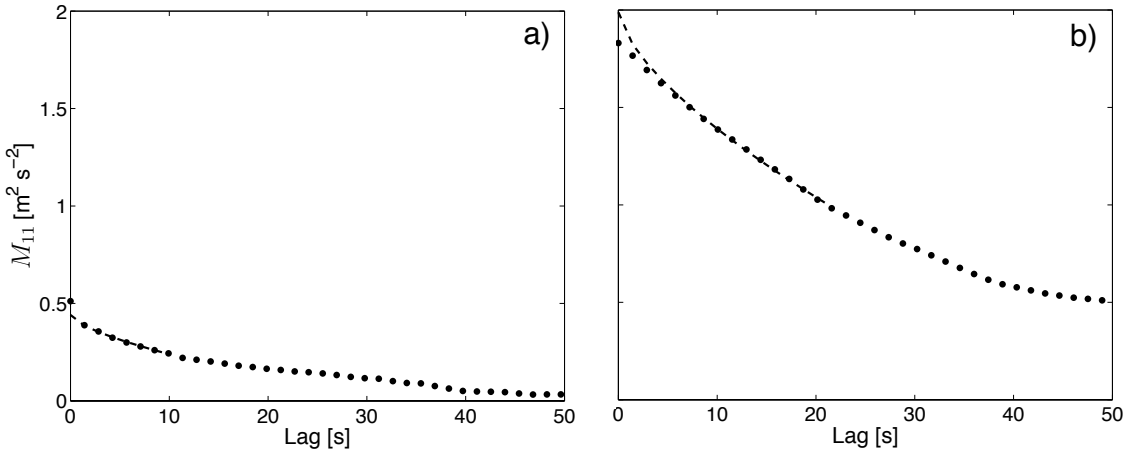

Figure 2.5: The dashed black lines are example fittings of the structure function (Eq. 2.4) to M_{11} values from the DL observations, which are shown by black dots. The fitting shown in (a) is expected when white noise is present, as the peak at lag zero is attributed to noise. Within (b), M_{11} at lags zero and one are less than is expected from isotropic turbulence. This is attributed to the volume and time averaging effects of the DL when noise values are very low.

Hollinger and Richardson 2005). These errors, which are related to how representative statistics from a single measurement location are to the PBL over an area, need to be considered when making generalizations about the PBL from single-point measurements. However, they are outside of the scope of this study. Since measurements from the DL and sonic anemometer were taken within a few metres of each other, which is smaller than the resolution volume of the DL, measured statistics are expected to be very similar to each other and errors due to the spatial separation of the instruments should be minimal. Any differences in statistics

Table 2.2: Typical values of τ_{min} and τ_{max} that are used during LATTE.

	Min [s]	Max [s]	Mean [s]	Standard Deviation [s]
τ_{min}	1.4	8	2.9	2.2
τ_{max}	2.8	35	11.5	9.1

of w between the two instruments are more likely due to differences in sizes of sampling volumes and measurement principles.

2.4 Comparison of Vertical Velocity Statistics

Observations are averaged over 30-min windows for the computation of M_{11} and other vertical velocity statistics from the DLs and sonic anemometers. During time periods when the instruments are waked from the 300-m tower, data are removed since characteristics of the sampled turbulence will be influenced by the tower and not representative of the PBL. For the removal of possibly waked measurements, observations are removed when the upwind direction was within $\pm 45^{\circ}$ of the tower. Measurements are also removed during time periods when precipitation or virga is evident on ceilometer measurements at the BAO site, since precipitation affects the DL measured w. Since the method discussed in Sect. 2.3 quantifies and removes noise, no explicit SNR filter was used to remove observations. All measurements of w from the DLs, regardless of the SNR value, are used in the computation of σ_w^2. However, DL data are removed during time periods when the estimated $\overline{\varepsilon'^2}$ is larger than a threshold. Several different threshold values were evaluated, and a threshold of 1 $\mathrm{m}^2\ \mathrm{s}^{-2}$ was a good compromise between keeping data where accurate σ_w^2 statistics would be retrieved and eliminating meaningless results. Threshold values based on the ratio of $\overline{\varepsilon'^2}$ to σ_w^2 were evaluated, but no threshold ratio could be found that both kept accurate values of low σ_w^2 and removed inaccurate values of high σ_w^2. Sampling errors $\Delta\sigma_w^2$ were calculated using

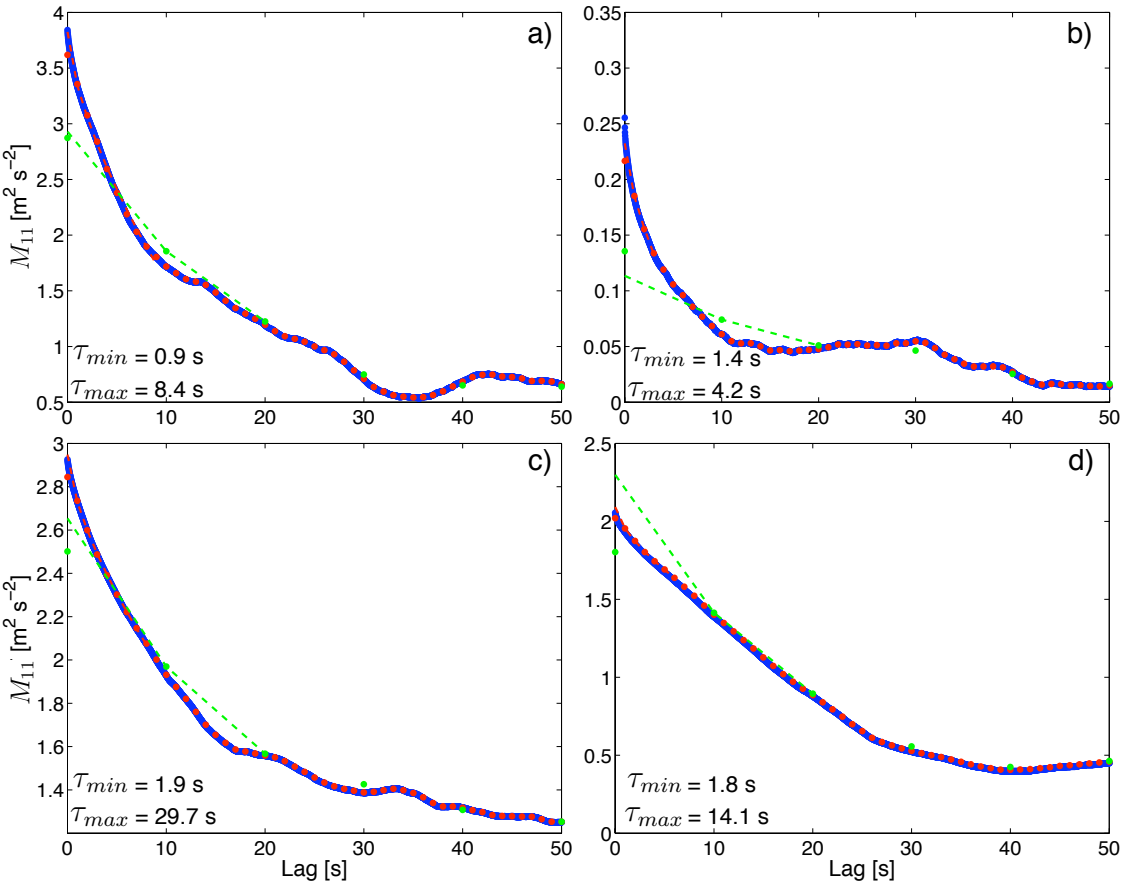

Figure 2.6: Sample M_{11} from the 300-m 60-Hz sonic data (blue dots) compared with the sonic data averaged to 1-Hz (red dots) and 0.1-Hz (green dots). Dashed lines are the fittings of Eq. 2.4 to the filtered sonic data, using the specified number of lags discussed in Sect. 2.3.2. M_{11} is calculated over 0200–0230 UTC (a), 0100–01300 UTC (b), 2000–2030 UTC (c), and 2030–2100 UTC (d) all on 27 March. Values of τ_{min} and τ_{max} are provided in the lower left.

formulations within Lenschow et al. (1994). These errors were found to be less than 5% of σ_w^2 for 84% of all DL observations due to the long half-hourly averaging time in comparison to t_{int} which was typically on the order of 1 min. In fact, for 50% of the DL estimates, the sampling error is less than 1%. Thus, throughout the rest of this study, sampling error is generally not a significant source of error and discrepancy between the DLs and the sonic anemometers.

2.4.1 Effect of Temporal Averaging and Number of Lags for Fitting

As discussed in Sect. 2.3.2, the proper number of lags to use for the fitting of the Eq. 2.4 has not been evaluated carefully previously. Here, the autocovariance method is applied using various amount of lag time to identify the accuracy of estimated values of σ_w^2 for differing numbers of lags. Measurements of w from the SE sonic anemometer at 300-m are averaged over 1-s (1-Hz) and 10-s (0.1-Hz) intervals, to simulate the typical averaging times of DLs and DIALs/Raman lidars respectively. From these averaged timeseries, values of M_{11} are calculated to test various lag times for the extrapolation.

Examples of M_{11} calculated from the raw and averaged sonic anemometer measurements are shown in Fig. 2.6, with fittings of the structure function applied using the specified number of lags outlined in Sect. 2.3.2. τ_{min} is calculated assuming a range gate size of 20 m, simulating DL values of τ_{min}. Values of $M_{11}(0)$ from the 1-Hz and 0.1-Hz averaged data are smaller than those from the 60-Hz observations, since the small-scale fluctuations are not resolved during the averaging. However, values of M_{11} at larger lags, from the 1-Hz averaged and raw observations, are often very similar. Thus, the fitting of the structure function to the 1-Hz observations generally accurately models M_{11}, and the extrapolation to zero lag is nearly identical to that from the raw time series. Values of M_{11} from the 10-s averaged data are not in good agreement with those from the raw timeseries, especially when M_{11} increases quickly at small timescales as in Fig. 2.6a, b. Due

to these differences, values of M_{11} are not accurately modeled when fitting the structure function to the 0.1-Hz observations.

To further evaluate the effect of averaging time and amount of lag time used, comparisons of estimates of σ_w^2 using the structure function fitting are compared with those from raw sonic anemometer measurements, shown in Fig. 2.7. Estimates of σ_w^2 are calculated from the 0.1- and 1-Hz measurements using both 100-s of lag time and the previously defined number of ideal lags. The 100-s of lag time is similar to those used when applying this method to DIAL or Raman lidar measurements (e.g., Behrendt et al. 2014), which is needed since these observations are contaminated by significantly larger values of ε'^2 and the sampling rate is much lower.

Using the previously mentioned ideal number of lags, the σ_w^2 estimates from the 1-Hz averaged data are in close agreement with those calculated from the raw 60-Hz measurements for the entire range of σ_w^2. This indicates that the sonic observations can be accurately modeled by the structure function fit and contain little noise after the spike removal mentioned in Sect. 2.2.1. Additionally, the lags defined in Sect. 2.3.2 are the correct lags to use to retrieve accurate estimates of σ_w^2. With the 0.1-Hz averaged observations, estimates of σ_w^2 generally are in agreement with the true value of σ_w^2 when using the ideal number of lags, although greater scatter is apparent. This also shows that the random error that may arise from using varying number of lags is minimal. If the random error were to change drastically based on the variable number of lags used in the fitting, there would be much larger

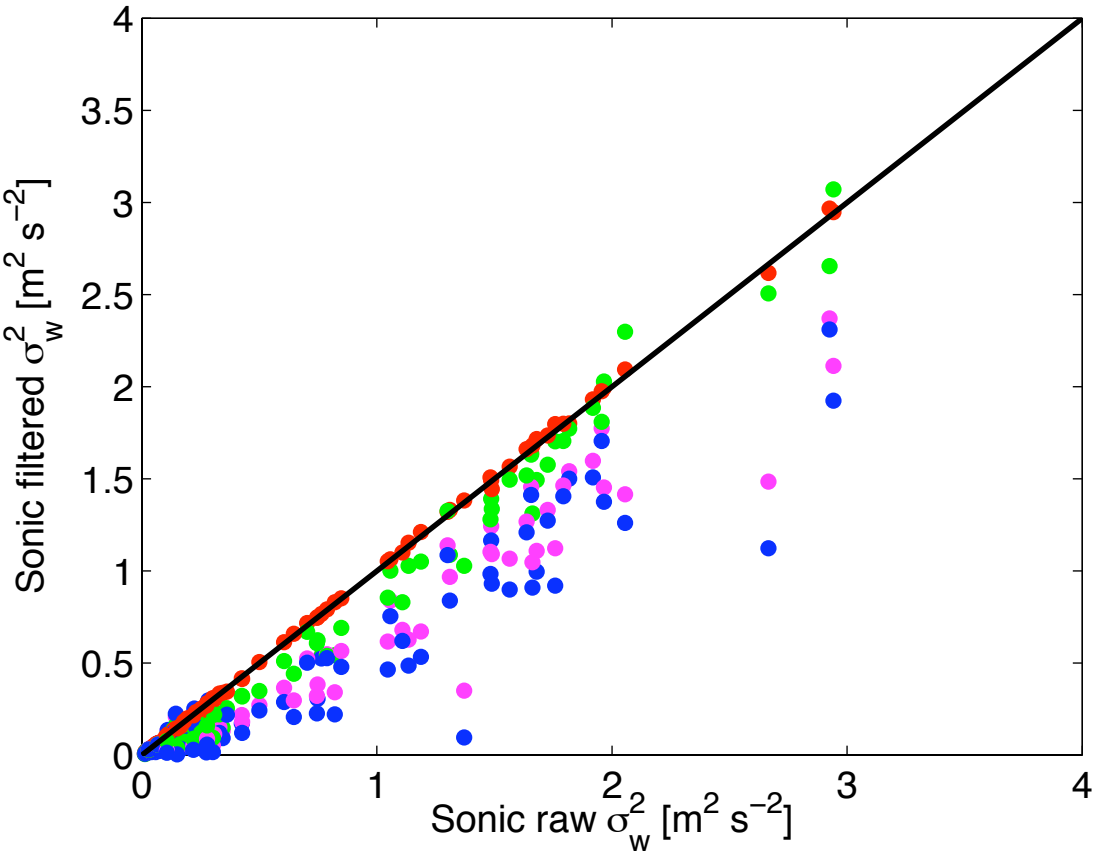

Figure 2.7: Relation of σ_w^2 values computed from the raw 30-min sonic timeseries compared with those estimated from the fitting of Eq. 2.4 to the filtered sonic anemometer data at 300-m. Red and green dots are the estimate from sonic data averaged to 1-Hz and 0.1-Hz respectively, after the fitting is applied using the specified number of lags discussed in Sect. 2.3.2. Magenta and blue dots are estimates from sonic data averaged to 1-Hz and 0.1-Hz, after the fitting is applied using 100 s of lag time.

scatter for some of the data points depending on the amount of lags that are used. However, since the data (red dots in Fig. 2.7) follow nicely along the 1-1 line, the fitting is good for all lag times used and the random error due to the variable lag time is small.

However, when 100 s of lag time is used within the fitting of the structure function, estimates of σ_w^2 are generally grossly underestimated regardless of the averaging time. This lag time should never be applied under stable conditions since the inertial subrange is small. However, it is also apparent that when turbulence is

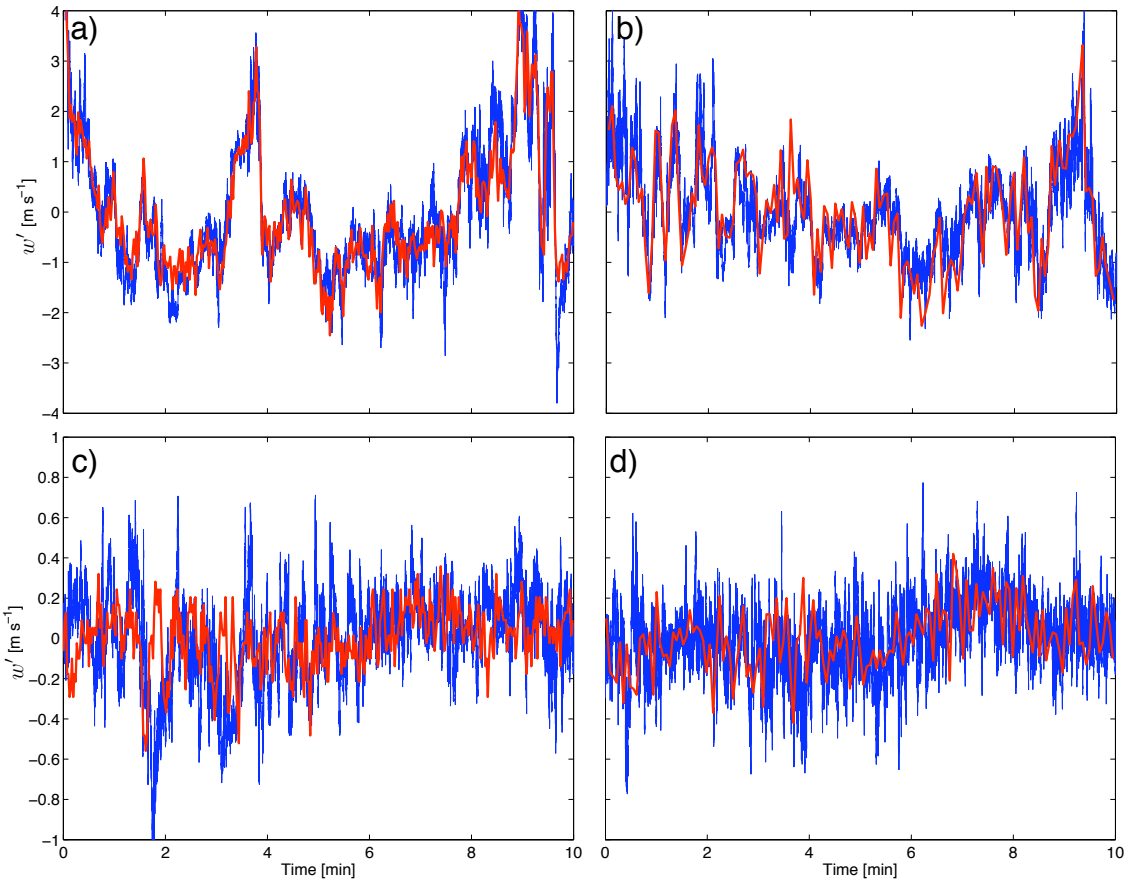

Figure 2.8: 10-min timeseries of w' during unstable (a, b) and stable (c, d) conditions, with each stability being during the same time periods when the sonic anemometer is not waked by the 300-m tower. OU DL data are at 300-m (a, c), and LLNL WC measurements are at 100-m (b, d). Red line shows the DL timeseries, while the blue line shows the comparable timeseries from the SE sonic at the same height.

strong during convective conditions, when 100 s lag time is often used, this amount of lag time is too large and leads to underestimates of σ_w^2. Furthermore, since σ_w^2 is underestimated, values of t_{int} as defined in Eq. 2.9 will be overestimated. This leads to the inaccurate interpretation that a larger number of lags is acceptable to use.

2.4.2 Comparison of Timeseries of w from DLs and Sonic Anemometers

Example timeseries of w' from each DL compared with similar measurements from sonic anemometers are shown in Fig. 2.8 for both convective and stable periods. Generally, measurements from both the sonics and DLs tend to show similar trends in how w' varies over time. Maximums and minimums of w' occur at nearly the same time, which is particularly apparent in Fig. 2.8a, b where the fluctuations are much larger. The magnitude of each individual maximum/minimum of w' is generally less in the DL observations as compared to those from the sonic anemometers. The longer time and larger volume averaging of the DLs reduces the magnitude of its observed fluctuations. Additionally, both DLs do not resolve all of the fluctuations that occur at short timescales. Differences is sampling frequency of the OU DL and LLNL WC are evident, particularly in Fig. 2.8a, b. Since the LLNL WC has a lower sampling rate than the OU DL, turbulence statistics computed from its measurements are not as representative of the true atmospheric variance as those from the OU DL.

Observations during stable conditions, shown in Fig. 2.8c, d, show less agreement in the time evolution of w' between the DL and sonic anemometer measurements compared to those during unstable conditions. This can largely be attributed to the fact that much larger eddies, that can be more easily resolved by the DLs, are present during unstable conditions. This is also why the DL timeseries under stable conditions are in much less agreement with each other than those during unstable conditions.

2.4.3 Comparison of DL and Sonic Spectra and Autocovariance Function

Several examples of M_{11} and the spectra of w from the OU DL and LLNL WC, compared with similar statistics from the collocated sonic anemometer, are shown in Figs. 2.9, 2.10. The cases were picked to show the accuracy of the DL spectra and M_{11} under various conditions, and using a different number of lags in the fitting. Measurements from the sonic anemometer are averaged to replicate the averaging time and sampling frequency for each DL, to isolate how these parameters affect the measurement and evaluate the accuracy of using the method discussed in Sect. 2.3. Generally, the spectra for the OU DL show good agreement with those calculated from sonic anemometer measurements. Under all of the cases presented, the inertial subrange is well-captured by the OU DL, as a portion of the spectra follows the theoretical -2/3 line. However, at high frequencies within Fig. 2.9b, d, the OU DL spectra flattens out, which is likely due to noise in the signal increasing the variance. Noise within the OU DL spectra in Fig. 2.9f is large enough to cause an increase in the spectra at high frequencies.

While the spectra of w' from the OU DL are generally in agreement with those from the sonic anemometers, significant differences are apparent in M_{11} computed from the two instruments (Fig. 2.9a, c, d). For example, within Fig. 2.9a, M_{11} values are in general agreement for short lags up to 10 s, after which M_{11} computed from the OU DL is greater than that from the sonic anemometer. On the contrary, within the time period for Fig. 2.9e, the values of M_{11} are in better agreement at larger lags (greater than 30 s), but the OU DL derived M_{11} is much less than

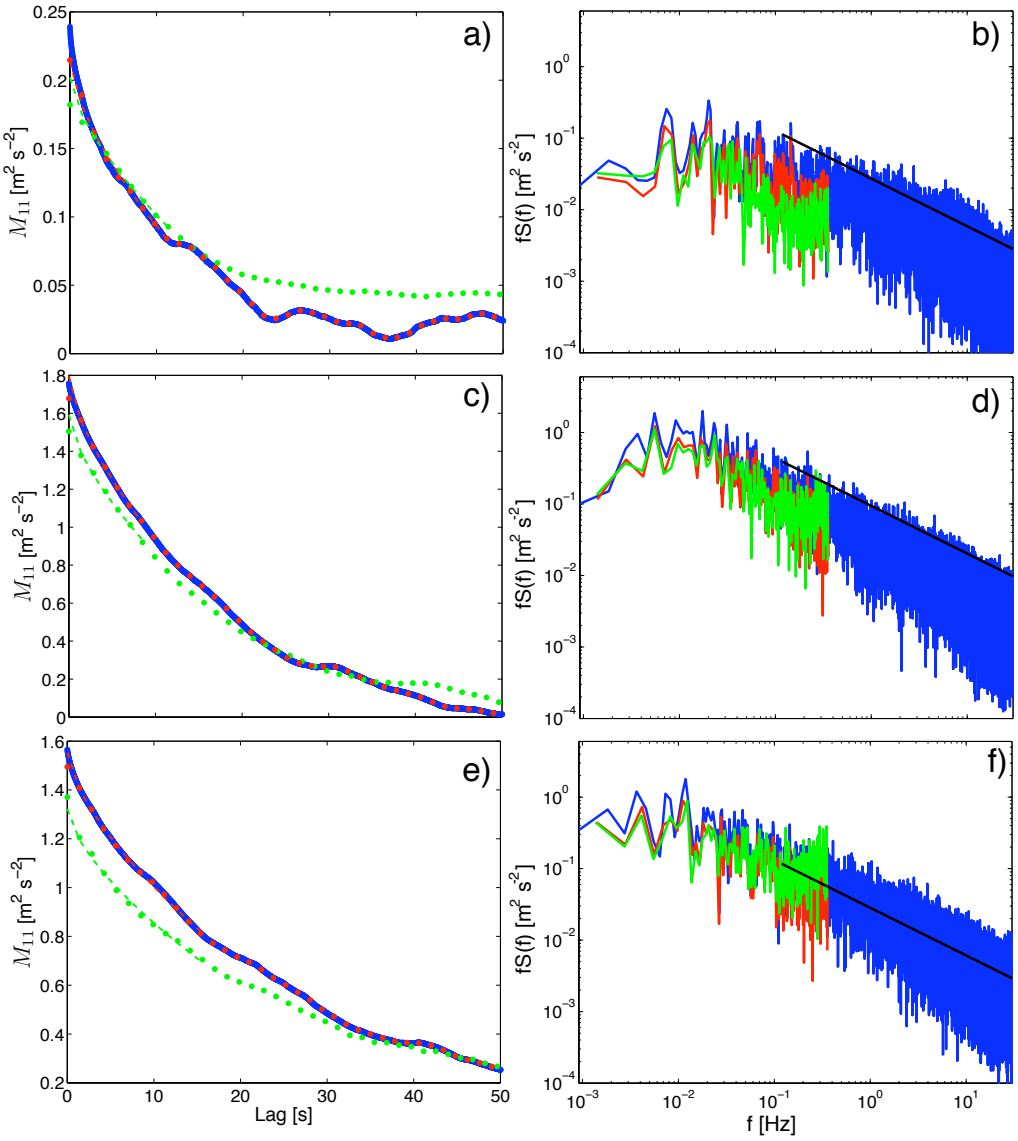

Figure 2.9: Sample M_{11} (left column) and the corresponding normalized spectra (right column) averaged over different 30-min time periods for measurements at 300-m. Measurements shown are those calculated from the raw sonic observations (blue), sonic data averaged to match the lidar averaging time (red), and OU DL observations (green). Dashed lines overlaid on M_{11} are the fittings of the structure function fit to the corresponding measurement. The fitting for the filtered sonic data use the same lags as that for the DL. M_{11} and the spectra are computed over 0530–0600 UTC (a, b), 1730–1800 UTC (c, d), and 2300–2330 UTC (e, f) on 27 March.

those computed from the sonic anemometers at shorter lags. The reasons for these differences are not clear, but is likely due to differing resolution volumes. The anemometer samples a volume of air precisely at 300 m, while the comparable OU DL measurement is averaged over a layer between 288–306 m.

Within all three cases shown in Fig. 2.9, $M_{11}(0)$ calculated from the OU DL measurements is less than the same value from the sonic anemometer measurements. This indicates that, within these cases, the variance is underestimated by the OU DL. Using the structure function fit, the estimated value of the variance from the OU DL data are improved for the cases shown in Fig. 2.9a, c. Within Fig. 2.9e, the fitting leads to a smaller value of OU DL-derived σ_w^2, due to the fact that significant is noise is present as shown in Fig. 2.9f. No significant differences in the accuracy of the σ_w^2 estimate depending on the number of lags used are apparent. By applying the structure function fit to the sonic anemometer measurements that are averaged to simulate the OU DL observations, it is shown that the fitting uses a proper number of lags to estimate the expected M_{11} to lag zero. The effect of averaging time on retrieved estimates of variance is discussed more throughly in Sect. 2.4.1.

Based on the presented spectra in Fig. 2.10b, d, f, LLNL WC w' spectra are in generally good agreement at most frequencies with those derived from sonic anemometer measurements. Similarly to the OU DL spectra, the LLNL WC spectra are often larger than those from the anemometers at high frequencies due to noise in the signal. The LLNL WC is often, but not always, able to resolve the

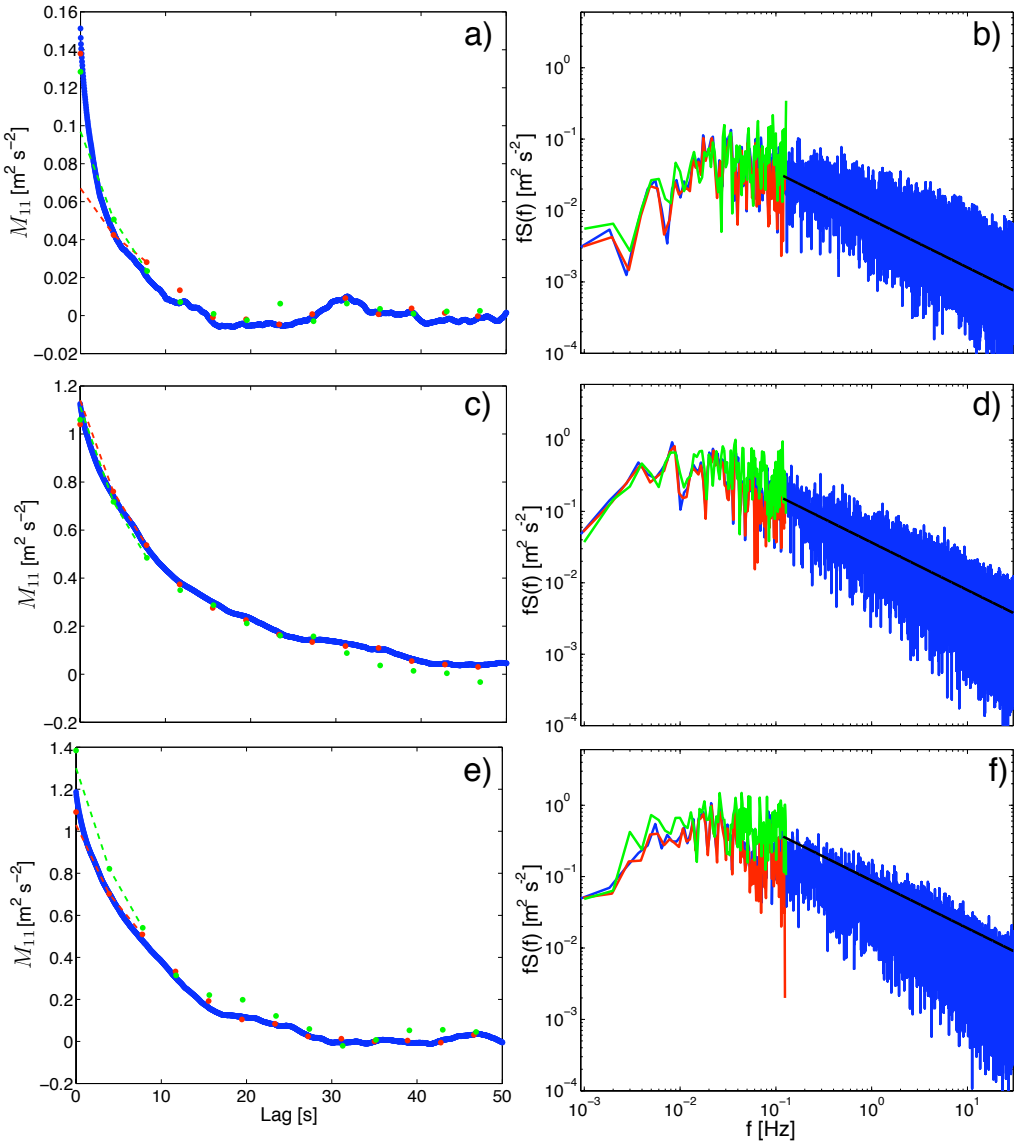

Figure 2.10: Sample M_{11} (left column) and the corresponding normalized spectra (right column) averaged over different 30-min time periods for measurements at 100-m. The spectra are made by averaging 10-min spectra within the 30-min time period to reduce the noise within the spectra. Measurements shown are those calculated from the raw sonic observations (blue), sonic data averaged to match the lidar averaging time (red), and LLNL WC observations (green). Dashed lines overlaid on M_{11} are the fittings of the structure function fit to the corresponding measurement. The fitting for the filtered sonic data use the same lags as that for the DL. M_{11} and the spectra are computed over 0030–0100 UTC (a, b), 2130–2200 UTC (c, d), and 1730–1800 UTC (e, f) on 27 March.

inertial subrange. Within the convective conditions shown in Fig. 2.10d, f, the high-frequency region of the LLNL WC spectra follows the -2/3-law expected within the inertial subrange. However, within the time period shown in Fig. 2.10b, the inertial subrange is not resolved due to the fact that turbulence scales are small and that the sampling frequency is 0.25 Hz, not fast enough to capture the smaller turbulence scales.

Generally, the values of M_{11} at various lags computed from either the LLNL WC or sonic anemometers are in agreement with each other. Although, differences in M_{11} do exist due to similar reasons to those discussed for the OU DL. For time periods where the inertial subrange could be resolved (i.e., in Fig. 2.10c, e), the structure function fitting yields an improved estimate for σ_w^2, compared to the raw variance at $M_{11}(0)$, that is closer to the sonic-derived value. However, when the inertial subrange is not properly resolved, the fitting of Eq. 2.4 poorly models the true values of M_{11} at short lags and the estimated value of σ_w^2 is grossly underestimated. This is expected, as the fitting is the expected M_{11} within the inertial subrange.

2.4.4 Accuracy of DL Variance Estimates

Comparisons of 30-min averaged σ_w^2 from the DL observations compared with those from sonic anemometers are shown in Fig. 2.11. Fig. 2.11 shows DL-derived values of σ_w^2 that were either directly-computed or estimated using the structure function fitting. For both the LLNL WC and OU DL, using the structure function

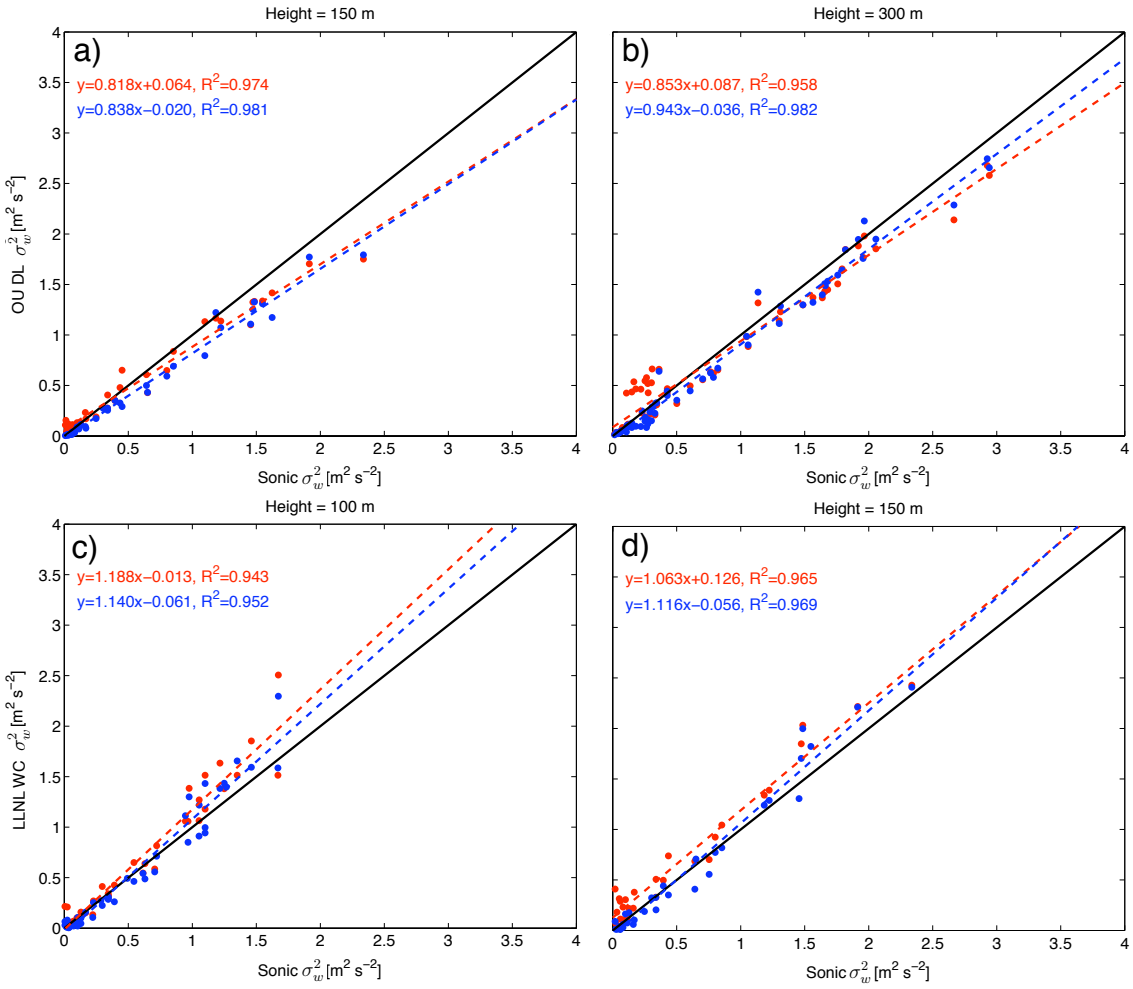

Figure 2.11: Comparison of σ_w^2 computed from DL observations with those from the sonic anemometer observations at different heights. Heights were chosen to highlight differences in the quality of observations with height, at heights where high-quality sonic and lidar observations are available. Observations from the OU DL are shown in (a, b), while LLNL WC measurements are shown in (c, d). Red denotes σ_w^2 computed from the raw DL data (i.e., $M_{11}(0)$), while blue is for values wherein σ_w^2 is taken as $M_{11}^*(0)$. Equation of the best fits are shown in the upper left of each plot, with R^2 being the coefficient of determination. Values of σ_w^2 are averaged over 30-min windows.

fitting to estimate values of σ_w^2 generally provided more accurate and less biased values, based on the higher values of R^2, a slope of the best-fit line closer to one, and y-intercept closer to zero compared to the values computed directly from the timeseries. Values of σ_w^2 from the OU DL are generally more accurate than those from the LLNL WC, since there is reduced scatter in the OU DL estimates. The higher scatter in the LLNL WC measurement is attributed to its reduced sampling frequency. Since there are 3 s gaps in its measurements of w while it collects data at off-zenith angles for the DBS scan, values of σ_w^2 computed from the LLNL WC are not as robust as those from the OU DL, which took w measurements continuously. Still, LLNL WC estimates of σ_w^2 are in generally good agreement with those from the sonic anemometers and show low bias when using the autocovariance fitting.

For the OU DL, estimates of σ_w^2 are generally improved when using the structure function fitting for the entire range of variance values. When σ_w^2 is small, noise is accurately removed and the OU DL estimates of σ_w^2 become in better agreement with those from the sonic anemometers. Conversely, when turbulent mixing is strong, values of OU DL-derived σ_w^2 are generally increased when applying the fitting, which corrects for the smaller scales of turbulence not being properly captured. For estimates of σ_w^2 from the LLNL WC, directly-computed values of σ_w^2 are generally larger than those computed from the structure function fitting regardless of the magnitude of the turbulence. Again, the autocovariance fitting accurately removes the contribution of noise in the measured σ_w^2, which is particularly apparent when σ_w^2 is less than 0.5 m^2 s^{-2} in Fig. 2.11d. For time periods when

turbulence is strong, the autocovariance fitting to the LLNL WC data often leads to reduced values of σ_w^2. This could be due to more noise in the LLNL WC observations compared to those from the OU DL under similarly strongly turbulent conditions, or the structure function fitting not as accurate with a reduced number of lags used. However, as shown in Fig. 2.10c, e, the M_{11}^* values are similar to that provided by the sonic anemometer measurements, and the inertial subrange is being resolved by the LLNL WC. Therefore, the reduced value of σ_w^2 for these turbulent conditions, after applying the fitting, is likely due to noise in the signal being removed.

2.4.5 Effect of Turbulence Characteristics and Stability

As shown earlier, the DL must be able to resolve the inertial subrange in order to accurately extract measurements of σ_w^2. If the inertial subrange is not explicitly resolved when turbulence scales are small, then a proper fitting that is representative of how M_{11} actually varies at small lags cannot be accurately applied. Regardless, even in these conditions when turbulence is weak, it is especially important to not simply use σ_w^2 directly computed from the timeseries, as ε^2 is often a large component of the computed σ_w^2, as shown for small values of σ_w^2 in Fig. 2.11b, d. Thus, even for these cases, applying the structure function fitting generally provides more accurate estimates of σ_w^2, although $M_{11}^*(0)$ values are systematically underestimates of the true variance.

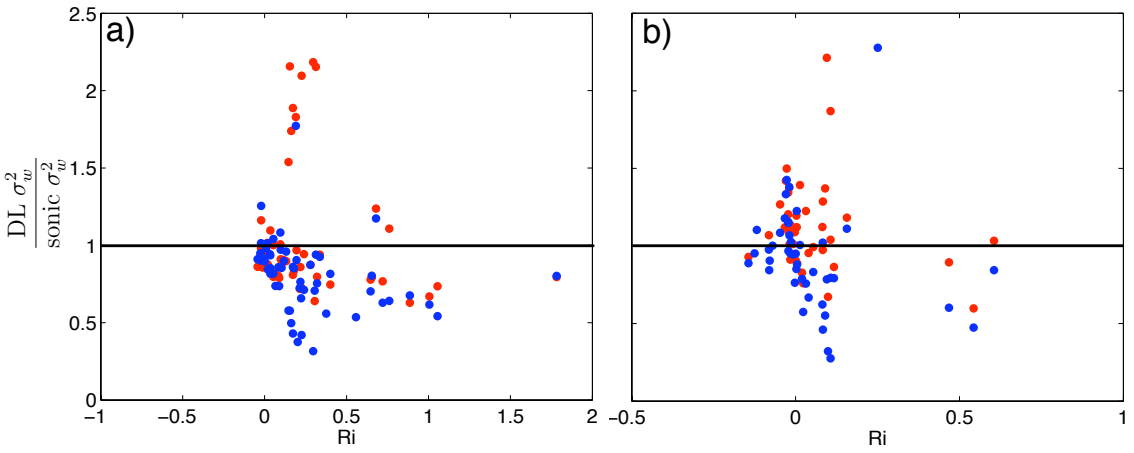

Figure 2.12: Relation of stability with error in lidar measured σ_w^2, as compared to σ_w^2 computed from sonic anemometer measurements, for raw (red) and corrected (blue) measurements. Measurements from the OU DL at 300-m are shown in a), while LLNL WC measurements at 100-m are shown in b). For some time periods under stable conditions (e.g., Ri greater than 0.25), uncorrected DL measurements have very high error, the ratio is greater than 2, and points are off the graph.

For the OU DL, estimates of σ_w^2 are generally in better agreement at 300 m than at lower heights. In fact, during the two-day observational period, σ_w^2 generally became more underestimated at lower heights reflected in the slope of the best fit line decreasing. While the reason for this is not entirely clear, it is thought that the more accurate measurements at higher heights is due to the fact that eddies are larger further from the ground, which are better resolved by the DL. These differences in how the accuracy of lidar variance measurements change with height needs to be considered when evaluating how second- and higher-order statistics vary with height.

The relationship between the accuracy of turbulence parameters measured by both DLs and stability, specifically Ri, during those observations is shown in Fig. 2.12. During unstable conditions when the Ri is less than zero, the estimates of σ_w^2 from both DLs are generally more accurate than those measurements during

stable conditions. This is evident based on the lower scatter and ratios of σ_w^2 closer to one under unstable conditions for both uncorrected and corrected estimates. Additionally, especially for OU DL measurements, the corrected measurements during convective conditions are larger and more accurate than those that are uncorrected. When conditions are stable, there is substantially more scatter in the quality of the DL measurements and the improvement due to the structure function fitting is less clear. There are times when the correction technique improves the σ_w^2 estimates, such as when significant noise is present that is accurately removed. These time periods also tend to be when SNR is reduced, as shown in Fig. 2.13. The method also can lead to worse estimates of σ_w^2, when turbulence scales are small and the inertial subrange is not properly resolved by the DLs. However, applying the extrapolation technique during stable conditions generally improves the estimates of σ_w^2. Although values of σ_w^2 are systematically underestimated when determined from the extrapolation method during stable conditions, the values are more comparable with each other than uncorrected measurements.

2.5 Discussion

Below, recommendations are made as to the implementation of this technique for use with DLs based on these results. Additionally, the importance of validation studies for measurements from various types of lidars is discussed.

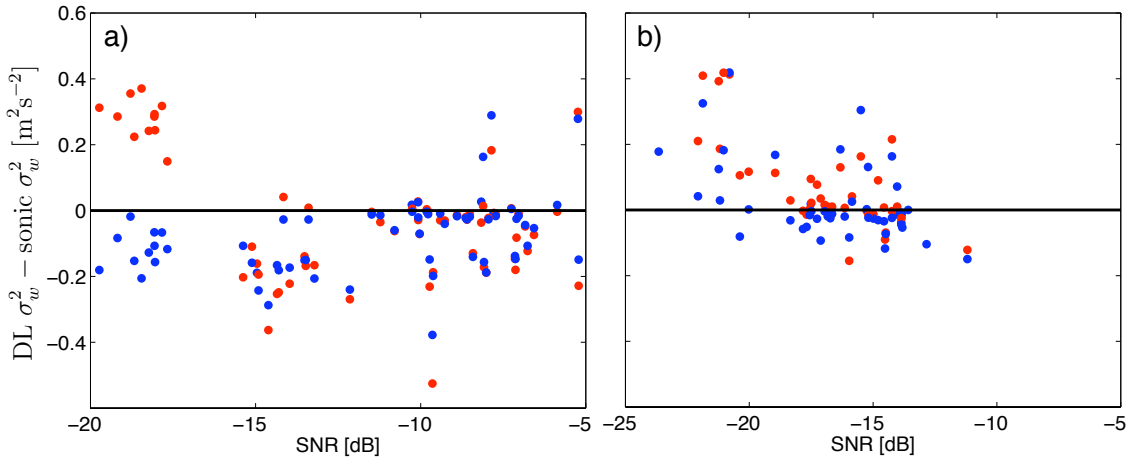

Figure 2.13: Relation of SNR with error of lidar measured σ_w^2, as compared to σ_w^2 computed from sonic anemometer measurements, for raw (red) and corrected (blue) measurements. Measurements from the OU DL at 300-m are shown in a), while LLNL WC measurements at 100-m are shown in b).

2.5.1 Possible Applications to Other DL Scanning Techniques

Within Sect. 2.4, it is shown that the autocovariance technique can be used to improve DL turbulence measurements, specifically σ_w^2 here, by both removing noise and correcting for unresolved turbulence structures. This method could similarly be applied to measurements of other turbulent quantities. For instance, for a DL continuously pointing at a very low elevation (near zero) into the wind, values of σ_u^2 can be derived by using a similar technique. Furthermore, this technique could be applied to be used in conjunction with more advanced scanning strategies. For turbulence measurements using the six-beam scanning strategy (Sathe et al. 2015), variances are first computed for each of the six independent beams. The six components of the Reynolds stress tensor can be computed from the individual variances of the six beams. However, due to the equations of computing each component of the Reynolds stress tensor, the effect of noise within each individual measurement is magnified. In particular, if there is a large amount of

noise in the vertical beam compared to other beams from differences in SNR, then negative values of σ_u^2 and σ_v^2 can be computed, which is not realistic. Thus, if the observations within each beam are taken at a large enough sampling rate to resolve the inertial subrange, the autocovariance technique should be applied to variances calculated from each beam before computing the velocity variances.

2.5.2 Importance of Validation Studies for Various Types of Lidars

Remote sensors, such as lidars, provide the ability to measure various quantities throughout the atmosphere. However, it is imperative that these measurements are compared with in situ observations for validation. Through this, relative accuracies can be quantified, so that future measurements using only remote sensors can be correctly interpreted and utilized. While the first in-depth analysis of σ_w^2 estimates measured using a method proposed by Lenschow et al. (2000) are presented here, further intercomparison studies of DL and in situ measurements are needed. Since this study was conducted over a short two-day period in early spring, the atmospheric conditions were not representative of the wide range that may occur over the entire year. Additionally, the measurement comparisons all were within the lowest 300-m of the PBL. While this provided a larger overlap region than allowed by most conventional meteorological towers, it still only encompasses a fraction of the possible PBL depth. As discussed in Sect. 2.4.4, there is evidence that biases in DL σ_w^2 change with height, which needs to be investigated further. These biases will effect how the DL-measured profiles of σ_w^2 vary with height.

In addition, measurements of higher-order moments from other types of lidars, such as DIALS and Raman lidars, should also be compared with in situ measurements. Due to the larger averaging time and often larger lag times used, errors associated with these lidars are likely higher and measured quantities are likely biased low, as discussed in Sect. 2.4.1. Turner et al. (2014a) compared Raman lidar-derived estimates of water vapour variance and skewness with those measured from aircraft, showing general good agreement in the trends in the profiles. However, the accuracy of the values of the DIAL and Raman lidar higher-order moments should be carefully evaluated.

2.6 Results

Here, a method discussed by Lenschow et al. (2000) of measuring higher-order statistics using autocovariances from lidar data are carefully evaluated. Specifically, estimates of vertical velocity variance and integral timescales derived from DL observations are compared with similar measurements from collocated sonic anemometers. Two DLs, a WindCube v2 and a Halo Streamline Pro, were placed within a few metres of the 300-m tower at the Boulder Atmospheric Observatory in Erie, Colorado, USA from 26 to 28 March 2014. The tower was instrumented with sonic anemometers every 50 m, up to 300 m, for validation and comparison of measurements from the DL.

The impact of several parameters on the accuracy and quality of lidar variances estimates is investigated using two methods. First, the sonic anemometer observations are averaged to simulate typical averaging times of different types of lidars, after which the autocovariance technique is used with various lag times to retrieve the variance values. Secondly, variances computed from the sonic anemometers are compared with those from the DL observations, both of those computed directly and using the autocovariance technique. Through these comparisons, it is shown that

- The amount of lag time used within the fitting of the structure function autocovariance is critical, and the number of lags leading to accurate retrievals of variance estimates are defined. Long lag times, which are generally used when extracting higher-order moments from DIALs and Raman lidars, lead to large underestimates of the true atmospheric variance.

- Not only does the autocovariance method accurately remove contributions from noise, but it also can be used to correct for limitations of time and volume averaging in the measurements. Thus, short lag times, for which the small-scale turbulent eddies are not accurately sampled (i.e., less than τ_{min}), should not be used when applying the fitting of the structure function.

- Generally, estimates of the vertical velocity variance from the DLs agree with those computed from sonic anemometers at the same measurement height,

especially during unstable conditions. Small differences in the measurements can be attributed to differences in averaging volumes (and averaging heights). For the WindCube, more substantial differences in the measurements are due to the lower sampling rate of the measurements, as vertical velocity is only measured every 4 s. By applying the autocovariance method, estimates of DL vertical velocity variance measurements are generally improved, even when turbulence is weak under stable conditions as small amounts of noise are a larger proportion of the total variance.

Herein, the importance of intercomparison studies for remote sensor measurements is highlighted. In particular, techniques for retrieving various derived-statistics can be validated and refined through the intercomparison of remote sensor measurements with high-quality in situ observations. Limitations in the applicability of the techniques can be identified as well. Since it is shown that DL-derived turbulence measurements are generally improved by applying the autocovariance techniques, it is thought that this method can be applied to more measurements taken using more advanced scanning strategies, such as the six-beam technique.

Chapter 3

Turbulence and Thermal Characteristics of the Nocturnal Boundary Layer with Southerly Winds

3.1 Background

Turbulence intensity, extent, and continuity in the nocturnal SBL are governed by many interacting processes and features. Generally, SBLs and their associated turbulence characteristics can be grouped into two broad categories: the weakly SBL (wSBL) and the very SBL (vSBL) (Mahrt 2014). The wSBL is relatively well-understood. Within it, turbulence is relatively continuous in space and time, and Monin-Obukhov similarity or local scaling defined by Nieuwstadt (1984) can generally be used. In the vSBL, turbulence is not well-understood and is difficult to parameterize or characterize, as turbulence is intermittent and not continuously connected with the surface (Banta et al. 2007; Mahrt 2011). Turbulence within the vSBL is sporadically generated by local and mesoscale processes such as gravity waves, density currents, and microfronts (Einaudi and Finnigan 1993; Sun et al. 2002; Newsom and Banta 2003; Mahrt 2010; Soler et al. 2014; Sun et al. 2014). The vSBL can take on several forms, such as a thin traditional boundary layer in which turbulence is generated at the surface and transported upward or an 'upside-down' boundary layer in which turbulence is generated aloft and

transported downwards towards the surface (Mahrt and Vickers 2002; Banta et al. 2006).

Differentiating characteristics that determine whether a wSBL or a vSBL forms is still an active area of research (e.g., Van de Wiel et al. 2012a; Sun et al. 2012; van Hooijdonk et al. 2014). Sun et al. (2012) used measurements from sonic anemometers on a 55-m tower to identify a threshold wind speed V_T at particular heights. If the mean horizontal wind speed V exceeds V_T, then strong bulk-shear generated turbulence is apparent at that height and turbulence intensity increases linearly with increasing wind speed. If V is less than V_T, then turbulence is weak and is either generated by local shear instabilities or transported downward by sporadic top-down turbulence events. Values of V_T have been determined for heights only up to 55 m using observations from sonic anemometers on a tower. Therefore, remote sensor measurements are needed in order to identify the maximum altitude for which a value of V_T can be clearly identified. Van de Wiel et al. (2012b) identify a crossing height in the velocity profile where the wind speed does not significantly change during the evening transition. The wind speed at the crossing height needed to be of sufficient magnitude, i.e., greater than V_T, to maintain turbulence overnight; this wind speed needs to be high enough to generate mixing and transport sufficient heat from above the surface downwards in order to prevent a strong surface-based inversion from forming.

While the wind speed at particular heights (whether at the crossing point or other heights) has been shown to be important in determining if either a vSBL or

wSBL develops, the depth of the mixing/SBL has not been addressed in previous studies. Additionally, since the threshold wind speed is a local relationship, the effect of the velocity profile above and below a given height is not considered even though it may be significant. Within this study, these issues will be explored by addressing the following questions:

1. The threshold wind speed has been shown to be an important criteria for sustaining bulk-shear generated turbulence near the surface at night. What is the maximum height up to which this threshold wind speed criteria can be used?

2. How important is the shape of the wind profile above and below a particular height for the development and maintenance of strong turbulence overnight? Does the threshold wind speed need to be exceeded at other heights for strong turbulence to develop?

3. How do the wind and turbulence profiles vary in the wSBL and the vSBL, and how do these compare to those found in previous studies?

4. How does the nocturnal potential temperature profile and nocturnal inversion evolve over the course of the night for the wSBL and vSBL?

The paper is structured as follows. Section 3.2 provides information about the experiment and instruments used within this study, including caveats about data from each instrument which are important for the interpretation of the results. Section 3.3 explains how vertical velocity variance is calculated from the DLs

and how noise within the data are removed. Section 3.4 discusses the use of the threshold wind speed criteria and composite temperature/velocity profiles for the vSBL and wSBL. The main results are summarized within Sect. 3.5.

3.2 The Lower Atmospheric Boundary Layer Experiment

The measurements used within this paper were collected during the first phase of the Lower Atmospheric Boundary Layer Experiment (LABLE-I), which took place at the SGP site operated by the ARM program. The ARM SGP site is located in rural north-central Oklahoma, USA, within patchy agricultural fields and open pastures and the terrain is relatively flat. Additionally, the site is situated near a climatological maximum of LLJs (Bonner 1968; Song et al. 2005), which can have a large impact on the structure of the SBL. LABLE-I was conducted from 18 September to 13 November 2012. Details about the LABLE-I campaign can be found in Klein et al. (2015). In addition to the instrumentation that is used herein, which is described below, radiosondes that are launched 4 times a day (0000, 0600, 1200, and 1800 UTC) at the SGP site are used for temperature profile comparisons.

3.2.1 Doppler Lidars

Observations from two DLs that were operating at the SGP site during LABLE-I are used here. One system is permanently installed at the SGP site and maintained by the ARM program (henceforth ARM DL), and the other DL was brought to the site by the University of Oklahoma for the duration of the experiment (henceforth

OU DL). Both of these systems are Halo Streamline DLs with nearly identical hardware. They use a pulsed 1.5 μm laser to detect backscattered energy from aerosols within the atmosphere. The ARM DL operates with 30-m range gate spacing, while the OU DL was operated at 18-m gate size.

The two DLs used slightly different sampling strategies. The ARM DL typically performed a PPI scan every 15 min at 60° elevation using eight azimuthal angles, which were used to derive the horizontal wind profile using the VAD technique (Browning and Wexler 1968). This PPI scan took ≈1 min to complete. In comparison, the OU DL performed PPI scans using 72 azimuths at both 40° and 70° every 30 min. These scans combined took 6 min to complete. The PPI scan at the lower elevation angle allowed retrieval of winds closer to the ground and at higher vertical resolution, but was subject to velocity aliasing when the wind speed was high, as often observed during LLJs. Between PPI scans, both systems collected vertical velocity w data at ≈ 0.8 Hz. Time series of w are used to calculate profiles of vertical velocity variance σ_w^2 and $\overline{w'^3}$, as described in Sect. 3.3.

3.2.2 Atmospheric Emitted Radiance Interferometer

The Atmospheric Emitted Radiance Interferometer (AERI) is a thermodynamic sounding instrument that observes downwelling infrared radiation from the atmosphere (Knuteson et al. 2004a,b). Under normal operations, the AERI collects a radiance spectrum that spans the wavelengths of 3.3 to 19 microns (520-3020 cm^{-1})

at a resolution higher than 0.01 m^{-1} approximately every 30 s. The AERI maintains a radiometric calibration better than 1% of the ambient radiance by viewing emissions from two well-characterized blackbodies (one kept at ambient temperature, the other at 333 K) every 5 min.

In order to transform the AERI observed spectra into a thermodynamic sounding, the spectra must be processed using a retrieval algorithm. Prior to retrieving the profiles, the observed radiance spectrum is processed by a noise-filtering algorithm (Turner et al. 2006) and averaged into 5-min samples. Then, AERI measured spectra are processed by AERIoe, an optimal estimation retrieval algorithm (Turner and Löhnert 2014) that is able to retrieve profiles of temperature and water vapour mixing ratio as well as cloud properties such as liquid water path and effective radius. AERIoe is an iterative Newton-Gauss retrieval (Rodgers 2000) that utilizes the Line-By-Line Radiative Transfer Model (Clough et al. 1992) to transform the radiance observed by the AERI into the retrieved thermodynamic variables. In order to begin the retrieval, AERIoe is provided an a priori dataset to act as a background field and a first guess. In this study, the a priori dataset is derived from the hourly Rapid Refresh (RAP) model analysis dataset available from the ARM data archive. This hourly dataset is computed by using approximately 2000 profiles from the RAP, centered in space and time around the AERI observation.

3.2.3 60-m Tower

A 60-m tower with sonic anemometers and infrared gas analyzers that measure CO_2 and H_2O densities at 4, 25, and 60 m is maintained by the ARM program at the SGP site. The 3-D Gill Solent Windmaster Pro sonic anemometers measure u, v, w, and sonic temperature at 10 Hz. The 10-Hz raw data are passed through a spike filter to eliminate noisy and erroneous data. From these measurements, the eddy covariance technique is used to calculate turbulent fluxes of momentum, CO_2, and sensible and latent heat over 30-min time windows (Kaimal and Finnigan 1994; Cook 2011). Additionally, 30-min means and variances of u, v, w, T, water vapour, and CO_2 were used extensively throughout this study. Values of $\overline{w'^3}$ over 30-min time series were also calculated.

3.3 Calculating Vertical Velocity Variance from Doppler Lidars

Radial velocity data collected by DLs are inherently noisy. The amount of noise can vary drastically and is largely based on the amount and size of aerosols suspended in the atmosphere and the humidity, since aerosols grow hygroscopically with increasing humidity (Kasten 1969; Carrico et al. 1998). Additionally, the noise in the signal can change very rapidly, such as with the passing of a cold front where the humidity typically decreases and much cleaner air is advected into the area. Therefore, it is not possible to simply remove the noise by treating it as a constant value. Instead, noise must be quantified and removed over short time periods and for every range gate when calculating second-order or higher moments.

To accomplish this, the methodology of removing noise from the DLs described in Ch. 2 is used , with a few differences that are discussed below. This methodology is applied to observations from both the OU DL and the ARM DL. While ideally τ_{min} and τ_{max} should be used for the fitting of Eq. 2.4, herein simply lags 1-4 (corresponding to $\approx$5 s of time lag) are used to reduce the processing time. A shorter segment is not used since the fitting often becomes too noisy. Since the extent of the inertial subrange is small during stable conditions (Coulter 1990), it is not necessary to use more lags to fit Eq. 2.4 to the data.

Time series of w are divided into 30-min segments, so that the averaging periods are identical to those from sonic anemometers. Each 30-min segment is then detrended, thus removing the mean. Any gaps in the time series, such as when PPI scans are performed, are filled in with zeroes at 0.8 Hz to preserve the structure of the turbulence. From each 30-min w time series at each measurement height, M_{11} is calculated and corrected for the gap-filling through the relationship

$$M_{11}(t) = \frac{N}{N - N_0} M_{11,U}, \tag{3.1}$$

in which $M_{11,U}$ is the uncorrected autocovariance function, N is the total number of points in the timeseries (including gap-filled points), and N_0 is the number of gap-filled points that are zeroes. This completely corrected for any underestimates of M_{11} from the gap-filling, assuming that the gap-filled turbulence characteristics are not drastically different than the observed features. From the corrected M_{11}, values of $\overline{\varepsilon'^2}$ and $\overline{w'^2}$ are determined using Eqs. 2.5 and 2.6. Throughout the rest

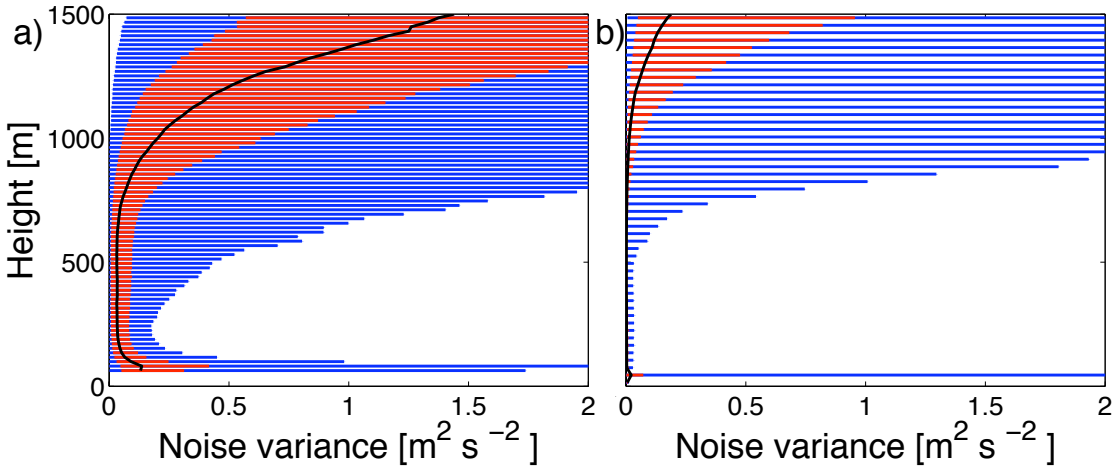

Figure 3.1: Profiles that show how the variance due to noise, $\overline{\varepsilon'^2}$, varies with height from the OU lidar (a) and ARM lidar (b). These are composites from all nocturnal profiles during LABLE-I to demonstrate typical coverage of both lidars during the campaign. The black line denotes the median noise value at a given height, while the red bars denote the noise within the 25-75 percentile and the blue bars denote noise within the 5-95 percentile.

of this study, values of σ_w^2 (σ_w) derived from the DLs refer to $\overline{w'^2}$ ($\overline{w'^2}^{1/2}$). This method does not remove any gravity waves. Thus, median values of the velocity statistics are presented, since mean values are strongly affected by large σ_w values caused by gravity waves. By using median values instead, the effects of gravity waves do not appear to significantly affect any of the results of this study.

For brevity, only the noise-removal of the second-order moment is discussed here. Using a similar method that is discussed in by Lenschow et al. (2000) in detail, noise is removed in the calculation of the third-order moment $\overline{w'^3}$ from the DLs. Specifically, the value of $\overline{w'^3}$ is estimated with a zeroth-order approximation, by taking $\overline{w'^3}$ as the average of M_{21} at ± 1 lag due to the asymmetry. This technique correctly removes noise within the third-order statistics, but values of $\overline{w'^3}$ from DLs within the SBL are not as accurate as those of σ_w since the magnitude of $\overline{w'^3}$ is much smaller.

Composite profiles comparing noise for the second-order moment from the two systems are shown in Fig. 3.1. These statistics are derived from profiles of all noise values between 0200-1200 UTC (2000-0600 local standard time). Noise from the ARM DL is considerably less than that from the OU DL. This can largely be explained by differences in range gate sizing. Since the OU DL was operating with a range gate size that was approximately half that of the ARM DL, the SNR from the OU DL was generally approximately half (i.e. 3 dB lower) that of the ARM DL. While the relationship between SNR and expected noise standard deviation due to speckle effects is non-linear (see Frehlich and Cornman 2002; Pearson et al. 2009), the noise variance is roughly expected to be related to be proportional to the square of the SNR. Both of the lidars typically had low noise values ($<$0.15 m^2 s^{-2} for 75% of the nocturnal profiles) up to at least 600 m, which is the layer where much of the analysis from the DLs is conducted. While these noise values are often low, performing the noise removal is important since turbulent mixing is often weak at night, and the noise variance can be larger than the true w variance within the SBL.

3.4 Analysis and Results

The results discussed here are derived using only data corresponding to a southerly wind direction. When northerly winds (and northerly LLJs) are observed, the turbulence characteristics of the nocturnal boundary layer are different. These discrepancies are likely related to systematic differences in the soil heat flux, such as warm ground heating near-surface air after a cold front passage, or differential

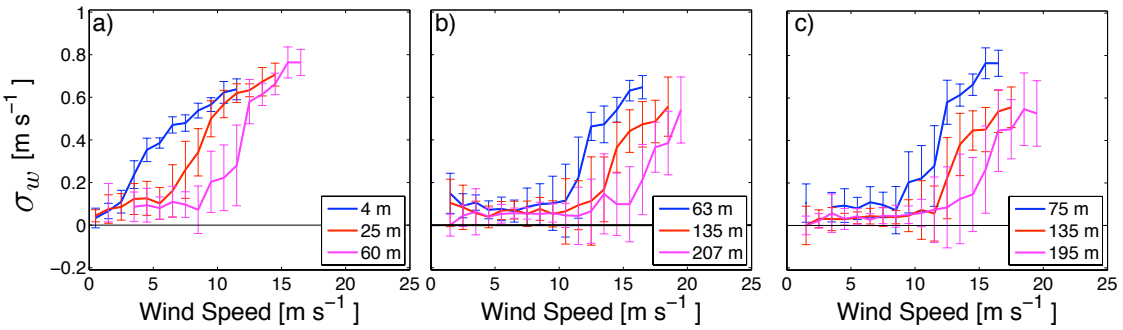

Figure 3.2: The relationship between the wind speed (for southerly winds) and σ_w, where σ_w is derived from 30-min w time series from sonic anemometers (a), the OU DL (b), and the ARM DL (c). Median σ_w is shown for each height by the solid lines and error bars denote the standard deviation of σ_w within each wind speed bin. Colours represent values at different heights given by the legends in the lower right corner of each plot.

temperature advection. The differences in turbulence/thermodynamic characteristics during northerly winds as compared to southerly will be explored in a future study, including possible reasons for the differences. Additionally, data collected while cloud bases are below 3 km are excluded from the study, as the AERI is not capable of retrieving accurate profiles above the cloud base. Time periods when fronts and other significant boundaries passed over the ARM site are manually determined based on rapid changes in the surface conditions, and are removed for this analysis.

3.4.1 Threshold Wind Speed

The concept of a threshold wind speed is tested using observations during the LABLE-I campaign. Measurements from the sonic anemometer are used first to verify that results similar to Sun et al. (2012), who also used sonic anemometers as well, could be obtained. Values of σ_w are separated into bins by 30-min means of V that are also measured by the sonic anemometers. The median and standard

deviation of σ_w are calculated within each 1 m s^{-1} bin of V as shown in Fig. 3.2a. Values of V_T are manually determined from sonic anemometer and OU DL data for the wind speed at which the slope of $d\sigma_w/dV$ increases significantly. It is clear that a well-defined V_T exists, above which turbulence increases rapidly with increasing wind speed. Conversely, when the wind speed is smaller than V_T, turbulence is weak and difficult to resolve with the DL. The value of V_T increases with height. Additionally, the slope of $d\sigma_w/dV$ is larger at higher measurement heights due to the impingement of the surface on turbulent eddies (Sun 2011). This set of findings is in agreement to those presented by Sun et al. (2012). One key difference from their findings is that the slope of $d\sigma_w/dV$, when V is greater than V_T, is not constant at any height. The amount of mixing tends to increase rapidly when V exceeds V_T, but the slope of $d\sigma_w/dV$ tends to decrease for stronger V. This result may not be apparent in the study by Sun et al. (2012) due to the fact that the maximum wind speeds within their study were not as large as those observed during LABLE-I.

The relationship between wind speed and σ_w, as observed by different instruments, is compared within Fig. 3.3. The exact measurement heights are not identical, due differences in measurement volumes and range gate spacing between the DLs, which explains some of the observed differences between the instruments. For example, the value of V_T appears to be larger for the ARM DL, due to the fact that the center of its measurements volume is 12–15 m higher than the center

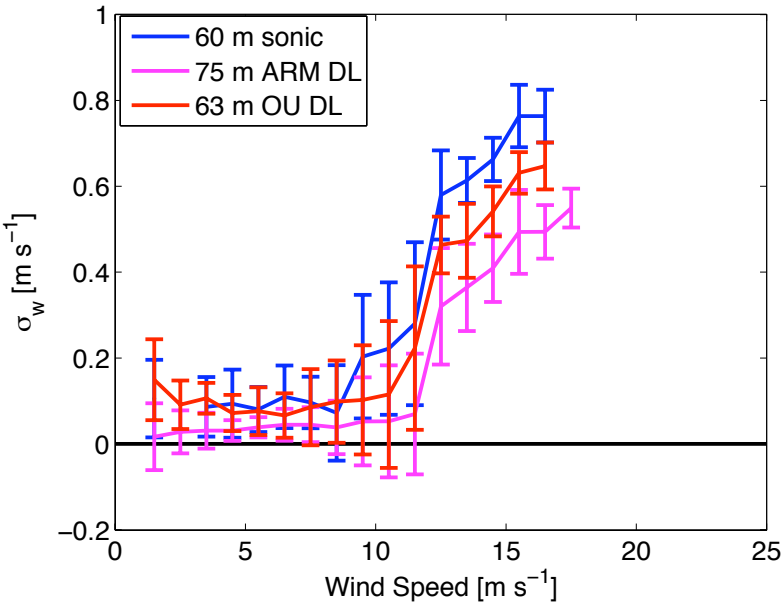

Figure 3.3: Same observations shown as in Fig. 3.2, comparing the observed relationship of σ_w on wind speed from different instruments at nearby measurement heights.

of the other two instruments' volumes. Generally, trends in the relationship between wind speed and σ_w are similar between the different instruments. However, σ_w as measured by the DLs tends to be smaller than that measured by the sonic anemometers. Albeit, some of these observed discrepancies may be explained by variations in the measurement height between instruments, as well. Farther from the ground, σ_w is expected to be smaller for similar wind speeds. Overall, the general agreement between the sonic anemometer and DLs demonstrates that measurements from the DLs can be used to estimate values of V_T.

Observations from the DLs were used to investigate if the V_T concept holds true for higher heights, and to test if DL measurements are of high-enough quality to find similar relationships. A similar method to that used for the sonic anemometer observations is also used with the DL observations. Horizontal wind speeds derived from PPI scans are used for separating the data into bins according to V.

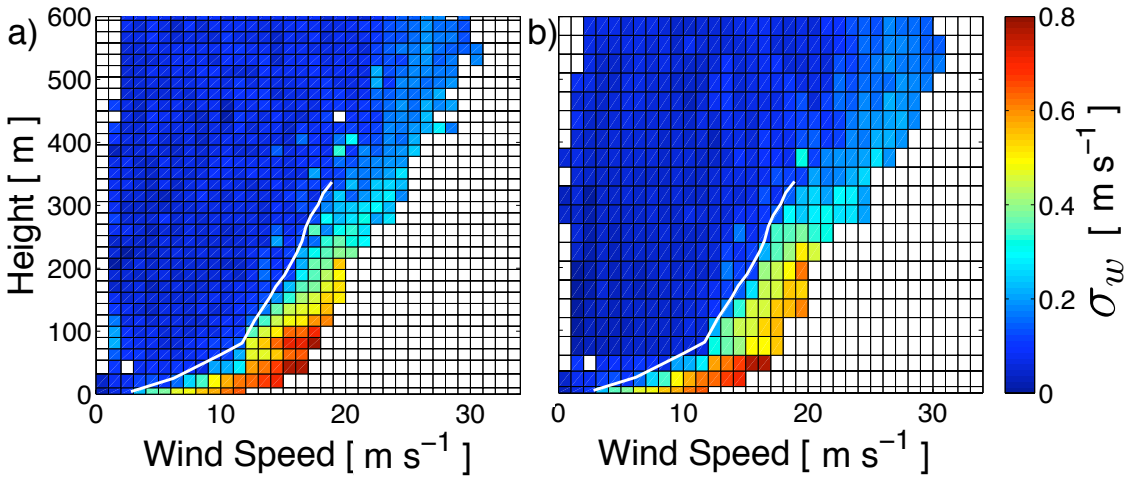

Figure 3.4: Median σ_w for a given wind speed at a particular height, where σ_w is derived from 30-min w time series from the OU Doppler lidar (a) and the ARM Doppler lidar (b). Data near the surface, where the lidars have no observations, are filled in with those from the sonic anemometers on the 60-m tower for visualization. The white line denotes the value of V_T at differing heights, determined from sonic anemometer and OU DL observations. The differing bin sizes in height is due to different resolution volumes. 430 independent 30-min profiles are used for this analysis. All bins with less than 10 data points have been removed (shown as white).

While these VAD wind profiles are not true 30-min averages, as measurements from the sonic anemometers are, the DL wind measurements are assumed to be representative of the 30-min mean horizontal wind speed. Similar relationships are found when applying this same procedure to the DL measurements, as shown in Fig. 3.2b, c. The value of V_T increases with height, as expected. However, at higher altitudes V_T becomes less distinct, as evidenced by the larger error bars for higher observations.

To further examine to what altitude a value of V_T can be established, profiles of σ_w at all heights from both DLs are shown in Fig. 3.4. Overall, values of σ_w from the OU DL are slightly higher than those from the ARM DL. This is especially apparent for measurements closer to the ground (specifically 75-150 m) and near

$V = V_T$. These discrepancies can be explained by the differences in volume averaging effects. Since the OU DL has a smaller sampling volume, it is capable of resolving smaller turbulent eddies that exist under weaker turbulence and near the surface. Both DLs clearly show that a V_T value exists up to heights of $\approx$ 300 m, as denoted within Fig. 3.4. At heights approaching 300 m, V_T becomes less defined and there is a more gradual increase in σ_w with increasing wind speed. There does not appear to be a threshold where σ_w increases dramatically above a certain wind speed, as the turbulence regime shifts. Although, if data were available with higher wind speeds, a V_T may become apparent at heights above $\approx$300 m.

The use of a V_T to determine the turbulence regime relies only on a local relationship of the wind speed at a given height and does not consider the wind profile around it. Thus, the use of this threshold does not take into account if the wind speed above or below a particular height exceeds V_T, thus theoretically generating bulk-shear turbulence at those heights. To investigate how non-local winds affect the turbulence intensity, wind profiles were categorized into four groups: profiles for which $V_{25\text{m}} > V_{T,25\text{m}}$, $V_{25\text{m}} < V_{T,25\text{m}}$, $V_{200\text{m}} > V_{T,200\text{m}}$, and $V_{200\text{m}} < V_{T,200\text{m}}$, where the subscripts denote the height of V and V_T. This tested the implications of the exceedance of V_T at a height on the turbulence above and below it. Results from this are shown in Fig. 3.5, including the number of individual profiles within each category. It is clear that if $V_{25\text{m}}$ is less than $V_{T,25\text{m}}$, as shown in Fig. 3.5b, then there is no generation of strong turbulence at any height above 25 m. A very thin

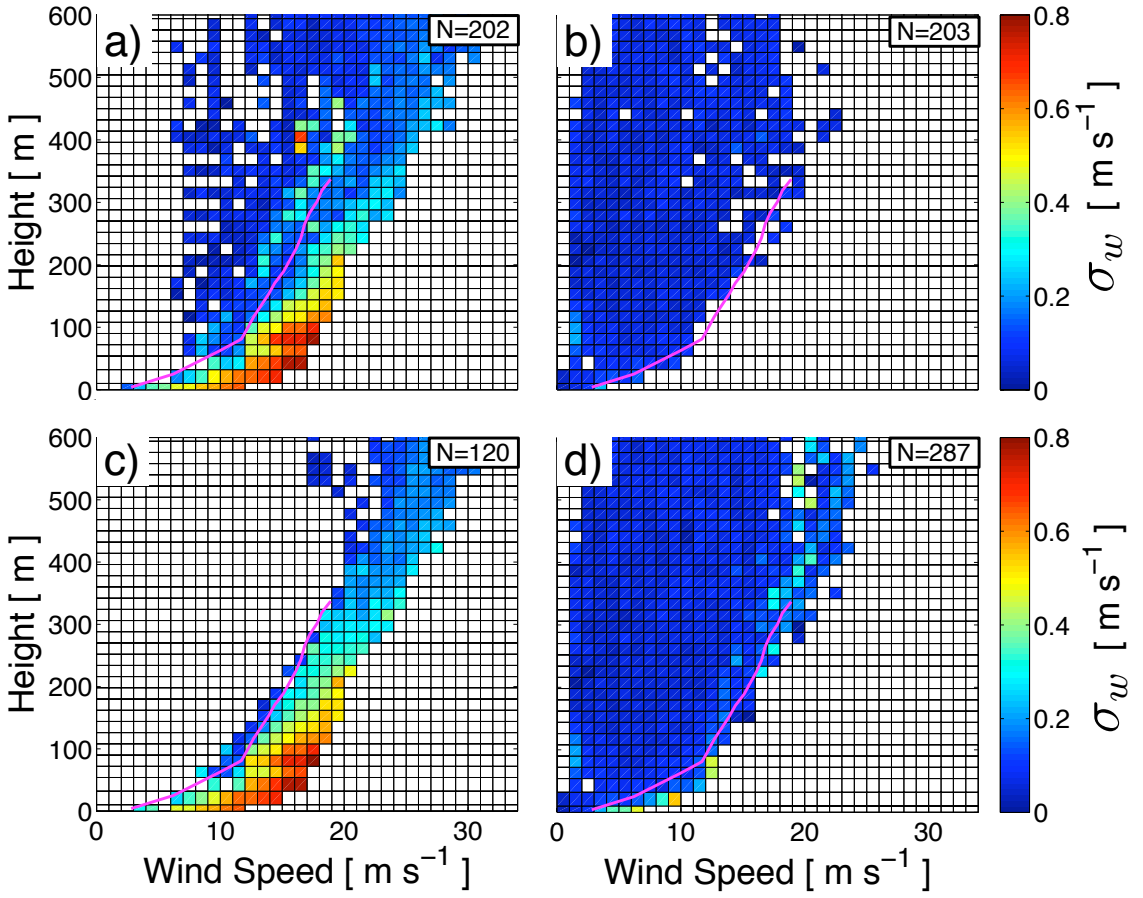

Figure 3.5: Median σ_w for a given wind speed at a particular height, where σ_w is derived from 30-min w time series from the OU Doppler lidar. Data near the surface, where the lidars have no observations, are filled in with those from the sonic anemometers on the 60-m tower for visualization. Data shown are from times when a) $V_{25\mathrm{m}} > V_{T,25\mathrm{m}}$, b) $V_{25\mathrm{m}} < V_{T,25\mathrm{m}}$, c) $V_{200\mathrm{m}} > V_{T,200\mathrm{m}}$, and d) $V_{200\mathrm{m}} < V_{T,200\mathrm{m}}$. The magenta line denotes the value of V_T at different heights, determined from sonic anemometer and OU DL observations. Total number of individual profiles within each category is given in the upper right corner of each plot. All bins with less than 10 data points have been removed (shown as white).

traditional boundary layer may be present, since $V_{4\mathrm{m}}$ may exceed $V_{T,4\mathrm{m}}$, generating turbulence near the surface. Additionally, in these cases the values of V rarely exceed V_T at any height above 25 m. The lack of strong turbulence at any height when $V_{25\mathrm{m}}$ is less than $V_{T,25\mathrm{m}}$ shows the importance of the generation of turbulence near the ground. Whereas if $V_{25\mathrm{m}}$ exceeds $V_{T,25\mathrm{m}}$ as shown in Fig. 3.5a, values of σ_w are sufficiently large (> 0.2 m s^{-1}) up to 25 m and to greater heights in many

cases. There are also cases when V at greater heights (i.e., 150-300 m) is less than V_T, but σ_w is greater than 0.2 m s^{-1}.

Sorting the profiles by whether $V_{200\mathrm{m}}$ exceeds $V_{T,200\mathrm{m}}$ also provides information about the structure of the SBL. In all the cases where $V_{200\mathrm{m}} > V_{T,200\mathrm{m}}$, values of σ_w are generally > 0.2 m s^{-1} up to at least 200 m, as shown in Fig. 3.5c. Values of V also generally exceed V_T at all heights below 200 m. For wind profiles in which $V_{200\mathrm{m}}$ is less than $V_{T,200\mathrm{m}}$, turbulent mixing may develop at heights below 200 m and not higher than 200 m (in cases where V exceeds V_T at lower heights). From these results, it may be inferred that strong mixing within the wSBL occurs up to the height at which $V < V_T$, assuming that $V > V_T$ at all lower heights.

3.4.2 Characteristic Turbulence Profiles under Different SBL Turbulent Regimes

While the threshold wind speed is a useful criteria in determining if strong turbulence is generated at heights up to 300 m, it does not provide information about the vertical profile of turbulence. Hence, profiles of velocity and σ_w are investigated using LABLE-I data. In previous studies, composite profiles of turbulent quantities (i.e., σ_w or standard deviation of the streamwise component σ_u) within the nocturnal SBL, which have been produced by combining observations over many nights, have been shown to normalize with the maximum low-level wind speed and the height of that maximum (Banta et al. 2006; Cuxart and Jiménez 2007; Kallistratova et al. 2013). Within our study, this maximum wind speed often coincided

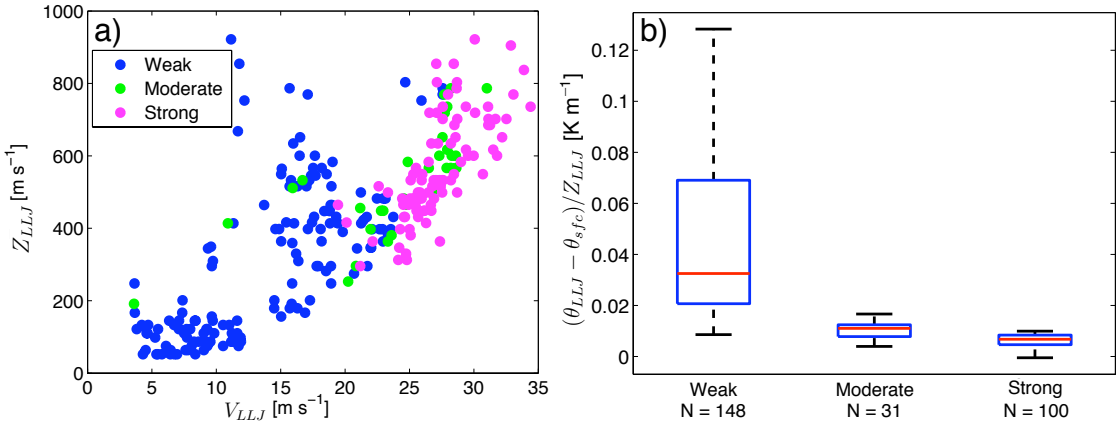

Figure 3.6: a) Relationship of V_{LLJ} with Z_{LLJ} and b) the bulk inversion strength from the surface to Z_{LLJ} under different turbulence intensity regimes where the red lines denote the median values, edges of boxes are the 25%–75% intervals, and whiskers show the maximum and minimum values. Weak, moderate, and strong turbulence regimes are categorized by $\overline{\sigma_w}_{,0-100\mathrm{m}} < 0.2$ m s^{-1}, 0.2 m s^{-1} $< \overline{\sigma_w}_{,0-100\mathrm{m}} < 0.4$ m s^{-1}, and $\overline{\sigma_w}_{,0-100\mathrm{m}} > 0.4$ m s^{-1} respectively. Number of individual 30-min profiles within each case is shown below the category name in b).

with the height of the LLJ, as LLJs were often observed during LABLE-I (Klein et al. 2015). Since some of the LLJs do not have a well-pronounced V maximum and exhibit a near-uniform wind profile above a certain height, the wind speed at the base of the LLJ (where shear becomes negligible, or less than 0.025 s^{-1}) is used for normalization. This wind speed at the base of the LLJ is referred to as V_{LLJ}, and it occurs at a height of Z_{LLJ} above which the wind shear is insignificant.

For the characterisation of turbulence and temperature profiles, three different turbulence regimes are used. These regimes are defined on the 30-min $\overline{\sigma_w}_{,0-100\mathrm{m}}$ (averages for measurements of σ_w from the OU DL under 100 m). The 100-m averaging layer is used to quantify the near-surface turbulence intensity that can be resolved by the DL, as the lowest range gate is 63 m. The weak turbulence regime is defined as $\overline{\sigma_w}_{,0-100\mathrm{m}}$ less than 0.2 m s^{-1}, which generally coincides with when V is less than V_T as shown in Fig. 3.2. The moderate turbulence regime is defined

as $\overline{\sigma_w}_{,0-100\text{m}}$ greater than 0.2 m s^{-1} but less than 0.4 m s^{-1}, which typically occurs when V is greater than V_T and $d\sigma_w/dV$ is large. The strong turbulence regime exists when $\overline{\sigma_w}_{,0-100\text{m}}$ is greater than 0.4 m s^{-1}, when V is much greater than V_T and after the slope of $d\sigma_w/dV$ decreases. Within both the moderate and strong turbulence regimes, stronger bulk-shear generated turbulence is expected since V is greater than V_T. As later discussed in Sect. 3.4.3, this categorization tends to separate the SBL cases into the wSBL when $\overline{\sigma_w}_{,0-100\text{m}} > 0.2$ m s^{-1} for both moderate and strong turbulence regimes, and vSBL when $\overline{\sigma_w}_{,0-100\text{m}} < 0.2$ m s^{-1} for the weak turbulence regime.

Generally during LABLE-I, LLJs associated with weak turbulence show lower wind speed maxima and are located much closer to the ground than LLJs accompanied by strong turbulence, as shown in Fig. 3.6. This agrees with findings by Shapiro and Fedorovich (2010), wherein LLJs with stronger mixing tend to be at higher altitudes than those with weaker mixing. Any LLJ with V_{LLJ} greater than 24 m s^{-1} tends to occur with a moderate or strong amount of mixing near the surface, while those with lower wind speed maxima occur with weak turbulence. Underneath the LLJ core, the static stability is much larger under the weak turbulence regime as compared to the moderate and strong turbulence regimes (Fig. 3.6b). When turbulence is weak, the large variability of the magnitude of the static stability is due to the strength and depth of the surface-based inversion evolving overnight, as later discussed in Sect. 3.4.3. Static stability in the moderate turbulence regime is slightly higher than that when strong turbulence is present.

While the static stability and turbulence intensity are inversely correlated, it is unclear if the turbulence causes a decrease in stability by mixing the inversion or if the absence of a strong surface-based inversion enables turbulence generation.

The LLJ characteristics of V_{LLJ} and Z_{LLJ} are used as velocity and length scales for normalization of composite profiles of V, σ_w, and $\overline{w'^3}^{1/3}$ within each turbulence regime, as shown in Fig. 3.7. These composites are produced by using all data within height bins of 0.1 Z/Z_{LLJ} for each category, in which Z/Z_{LLJ} was calculated for each individual 30-min profile. The shape of the wind profile for all three turbulence regimes tends to be very similar, as shown in Fig. 3.7a, d, g. Generally, there is a pronounced wind speed maxima with V decreasing above and below Z_{LLJ}. The wind profiles in the weakly turbulent regime tend to vary more, as evidenced by the larger error bars. However, the normalized shear below Z_{LLJ} tends to be very similar in all three regimes. The observations of normalized V from both the DLs and tower are in good agreement in regions of overlapping measurements.

Marked differences can be seen in Fig. 3.7b, e, h in the profiles of normalized σ_w between the three turbulence regimes. For all of the σ_w measurements shown here, the measurement error as calculated using equations within Lenschow et al. (2000) is less than 10% for 95% of the DL observations. Thus, the variability between profiles is much larger than the uncertainty in the measurements. Since these profiles are categorized by the magnitude of $\overline{\sigma_w}_{,0-100\mathrm{m}}$, it is not surprising that normalized values of σ_w below Z_{LLJ} within the strongly turbulent regime are

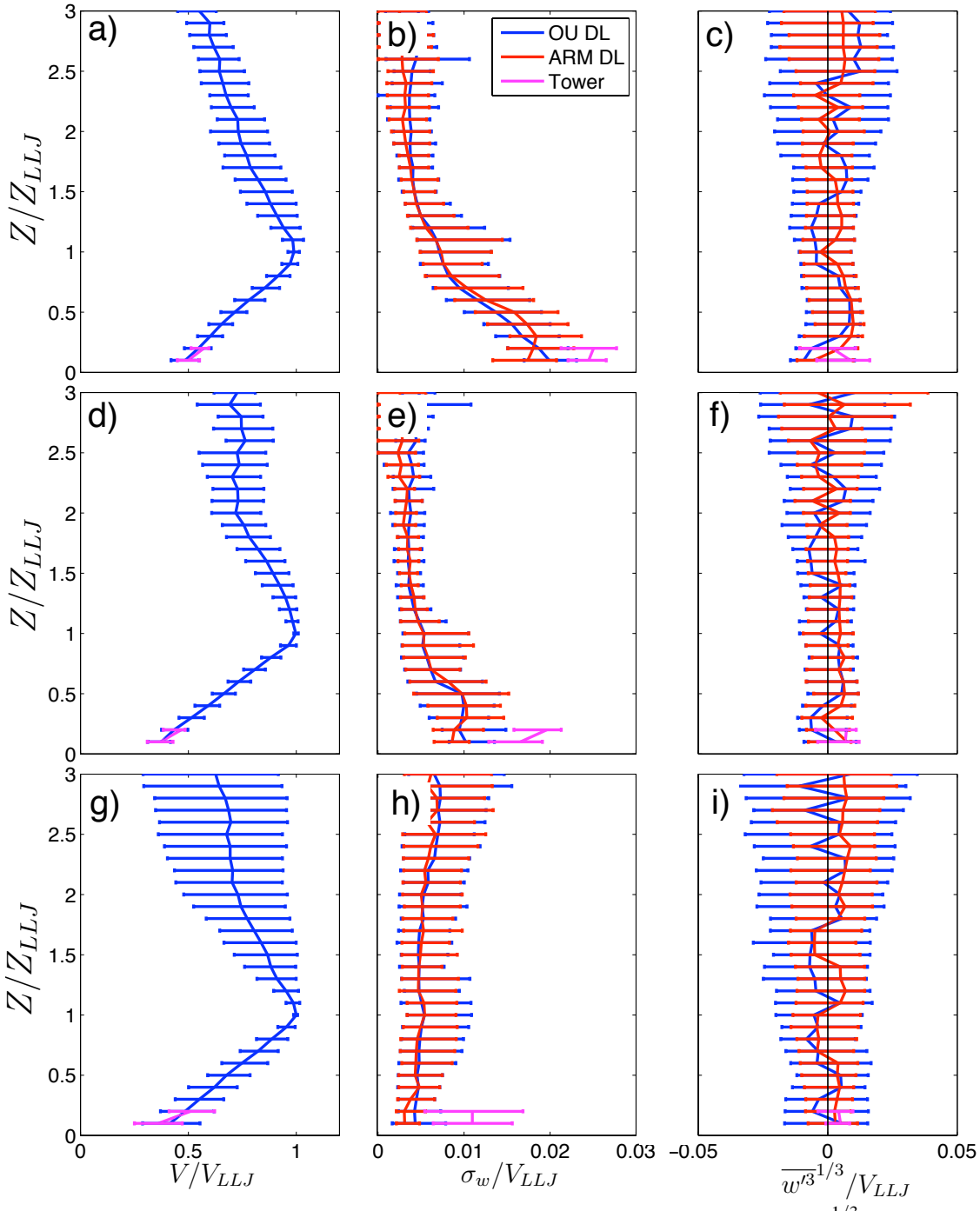

Figure 3.7: Composite profiles of the wind speed (a, d, g), σ_w (b, e, h), and $\overline{w'^3}^{1/3}$ (c, f, i) normalized by V_{LLJ}. The height is also normalized by Z_{LLJ}. Solid lines are the median values, while error bars denote the 15.9%-84.1% confidence interval ($\pm$1 standard deviation). Data shown are from profiles where the $\overline{\sigma_w}_{,0-100\text{m}}$ (calculated from the OU DL) is greater than 0.4 m s^{-1} (a, b, c), $\overline{\sigma_w}_{,0-100\text{m}}$ is greater than 0.2 m s^{-1} but less than 0.4 m s^{-1} (d, e, f), and $\overline{\sigma_w}_{,0-100\text{m}}$ is less than 0.2 m s^{-1} (g, h, i). Error bars are typically larger in the weak turbulence cases, since those profiles generally coincide with a weaker V_{LLJ}. Data from the ARM DL are not shown for the wind speed, since it provides no additional value and is very similar to the profile from the OU DL.

generally higher than those in weaker turbulence regimes. Generally in the strong turbulence regime, values of σ_w are highest near the surface and decrease linearly within the wSBL with height up to slightly above Z_{LLJ}, above which σ_w is nearly constant. This compares with similar profiles shown by Banta et al. (2006), in which σ_u is largest at the surface and decreases linearly with height and a minimum in σ_u exists at Z_{LLJ}, above which σ_u is roughly constant with height. No local minimum in σ_w at Z_{LLJ} is found using DL data from LABLE-I. This may be due to a different definition of Z_{LLJ}, as Banta et al. (2006) used the location of the wind maxima. The location where the shear becomes very weak is used in this study. Thus, the definition that is in use here sometimes leads to a lower value of Z_{LLJ}, hence no local minimum of σ_w is found at Z_{LLJ} within the present study.

The normalized σ_w profile within the weakly turbulent vSBL exhibits a nearly-constant value with height, shown in Fig. 3.7h. There is a weak indication of a localized maximum in σ_w at Z_{LLJ}, but it is difficult to make any conclusions with the large variability shown by the error bars. A maximum at Z_{LLJ} would agree with results from Prabha et al. (2008) and Kallistratova et al. (2013), who both used sodars and found a maximum of σ_w at the LLJ core. This would be indicative of an 'upside-down' SBL as described by Mahrt (1999), in which turbulence is generated above the surface and mixed downward. It is likely that the vSBL category presented here contains profiles in which either an 'upside-down' SBL or thin traditional SBL is present, as discussed by Mahrt and Vickers (2002).

Within the moderately turbulent SBL, the profile of normalized σ_w shown in Fig. 3.7e is a combination of the other two regimes. Values of normalized σ_w below Z_{LLJ} are smaller than those in the strongly turbulent wSBL, but higher than those in the weakly turbulent vSBL. The magnitude of normalized σ_w below 0.5 Z/Z_{LLJ} remains relatively constant. Banta et al. (2006) also categorized similar profiles, wherein σ_u remained constant within this same layer. With this profile, it is expected that turbulence is generated both underneath the LLJ core and near the surface. This indicates that the SBL with moderate turbulence intensity is a combination of an 'upside-down' and traditional boundary layer.

Profiles of σ_w from both DLs are generally in good agreement, although there are a few differences. At low heights (i.e., $Z/Z_{LLJ} < 0.3$), values of σ_w from the ARM DL increase with height above the surface, while the OU DL shows σ_w increasing towards the surface. These differences can be explained by the fact that the OU DL utilizes smaller range gates, so it is better capable of resolving the smaller turbulent eddies that are present near the surface. Measurements of σ_w from the sonic anemometers on the tower are significantly higher than those from the DLs; this is also explained by sampling volume differences, as the measurement volume of the sonic anemometers is several orders of magnitude smaller than those from the DLs. While the autocovariance method described in Ch. 2 can partially correct for these volume averaging effects of the DL, the correction is only applicable when the inertial subrange is explicitly resolved. Due to the predominantly small scales of turbulence in the SBL, the inertial subrange is often too small

to be resolved by the DL. Additionally, accurately retrieving estimates of σ_w^2 using the structure function fitting requires turbulence to be isotropic. However, vertical motions are suppressed under strong stratification and the turbulence becomes anisotropic (Hopfinger 1987; Riley and Lelong 2000; Waite and Bartello 2004; Lindborg 2006), which may invalidate this assumption leading to underestimates of σ_w^2 in comparison to those calculated from the sonic anemometer observations.

The composite profiles of normalized $\overline{w'^3}^{1/3}$, shown in Fig. 3.7c, f, i, are considerably more noisy than those of σ_w as evidenced by the larger error bars and less continuity in height. Additionally, the measurements from the different instruments do not always agree with each other. However, the measurement error, which was calculated using equations found in Lenschow et al. (2000), in 70% of the DL profiles is less than 10% of $\overline{w'^3}$. Thus, the profiles still contain useful information. Despite the significant uncertainty in the majority of the profiles, it is still possible to extract useful results. Within the strongly turbulent wSBL, both DLs indicate a generally positive $\overline{w'^3}$ below Z_{LLJ}, except near the surface where the DLs may not be able to properly measure this statistic due to sampling volume size and near-field effects. This generally positive $\overline{w'^3}$ is indicative of a traditional boundary layer being present, in which turbulence is generated near the surface and transported upward. This is also supported by σ_w decreasing with height below Z_{LLJ}.

Within the moderately turbulent regime, $\overline{w'^3}$ is generally positive in the layer of 0.5-1.0 Z/Z_{LLJ}, so turbulence is generated underneath that layer and transported

upward. However, within this regime, the negative minimum in $\overline{w'^3}$ at around 0.3 Z/Z_{LLJ} indicates turbulence from above is transported downward. Near the ground, turbulent energy is generally transported upward as indicated by the positive $\overline{w'^3}$ near the surface. This profile is indicative of a combination between a traditional and 'upside-down' boundary layer. In the weakly turbulent vSBL, no clear conclusions can be made about $\overline{w'^3}$ throughout the SBL since the profiles exhibit great variability, as shown in Fig. 3.7i. Additionally, as previously mentioned within this section, the vSBL regime is likely composed of both 'upside-down' and thin traditional SBLs in which $\overline{w'^3}$ is respectively negative and positive.

3.4.3 Evolution of Potential Temperature Profiles under Different SBL Turbulent Regimes

While the AERI uniquely provides high-temporal resolution temperature profiles, the quality of its measurements needs to be evaluated before being used to understand how the SBL temperature profile evolves overnight. The accuracy of the AERI measurements in the SBL is briefly discussed in Klein et al. (2015), but is also highlighted here with the emphasis on the accuracy of composite profiles. Individual and composite profiles of potential temperature θ from radiosondes and the AERI are shown in Fig. 3.8. Within these composites, the moderately and strongly turbulent regimes are combined since their thermal profiles and their evolution are similar. The small number of individual profiles within the moderately turbulent wSBL does not allow for meaningful hourly composites.

All of the observations shown in Fig. 3.8 are from 0530 UTC (2330 LT), which is when the 06Z radiosonde is typically launched. Within the θ profiles, the surface potential temperature θ_{sfc} is subtracted so that the values of θ relative to the θ_{sfc} are shown. This allows quantification of the inversion strength and depth. The individual profiles do show some differences, as the AERI tends to smooth out any sharp temperature gradients. Also, the altitude of any elevated inversion may not be properly captured by the AERI, due to the weighting functions of the AERI becoming more broad with increasing height. However, overall individual profiles of θ from both the AERI and radiosondes generally agree well for both $\overline{\sigma_w}_{,0-100\text{m}} > 0.2$ m s^{-1} and $\overline{\sigma_w}_{,0-100\text{m}} < 0.2$ m s^{-1}. Differences under the two turbulent regimes are apparent, and the composite profiles from the radiosondes agree well with those from the AERI. Although, in the composite profile for weak turbulence, the AERI tends to smooth out the strong surface based inversion over a deeper layer.

When turbulence is weak and $\overline{\sigma_w}_{,0-100\text{m}}$ is less than 0.2 m s^{-1}, a strong surface-based inversion is apparent which is congruent with the current understanding of a vSBL (Mahrt 2014). While the magnitude of the inversion varies from night to night, the composite θ profile provides an indication of the strength and depth of the nocturnal inversion on average. When turbulence is stronger and $\overline{\sigma_w}_{,0-100\text{m}}$ is greater than 0.2 m s^{-1}, only a weak surface-based inversion forms. This is consistent with characteristics expected with the wSBL, since the sustained turbulent mixing of air prevents a strong surface-based inversion from forming. In the

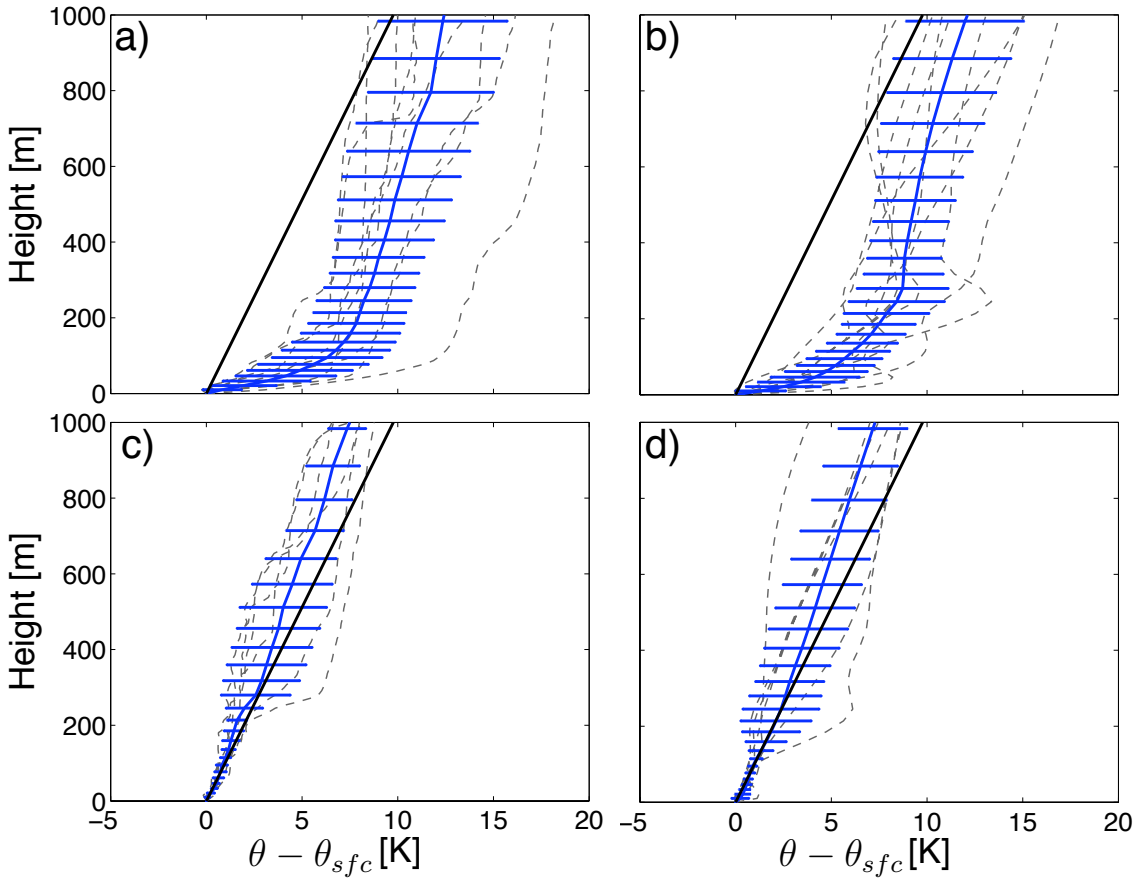

Figure 3.8: Composite profiles of $\theta - \theta_{sfc}$ showing the strength of the nocturnal inversion at 0530 UTC from radiosondes (a, c) and the AERI (b, d) when $\overline{\sigma_w}_{,0-100\text{m}}$ is less than 0.2 m s^{-1} (a, b) and $\overline{\sigma_w}_{,0-100\text{m}}$ is greater than 0.2 m s^{-1} (c, d). Dashed grey lines are individual profiles and the thick blue line denotes the mean profile, with the error bars showing the standard deviation. Thick black line denotes an isothermal profile.

wSBL in Fig. 3.8c, d, the temperature profiles tend to be isothermal throughout the lowest several hundered metres, up to a height where an elevated inversion is located or the profile becomes more unstable. This is reflected by both the individual and composite profiles from the AERI and radiosondes. The lower portion of the isothermal layer is located within the mixed wSBL, since the mean σ_w in the lowest 100 m is greater than 0.2 m s^{-1}. The reason for the tendency of the lower portion of the profile in the wSBL to be isothermal is unclear.

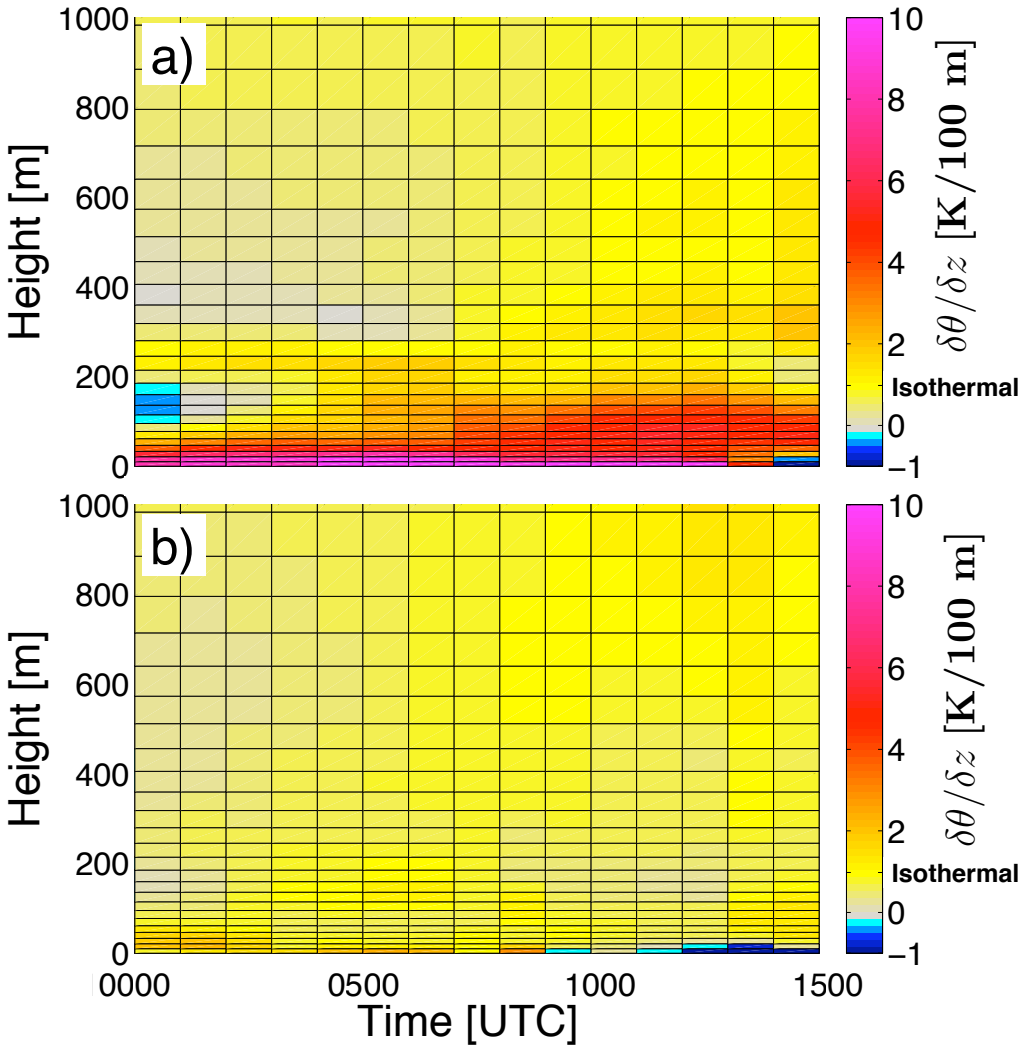

Figure 3.9: Nocturnal evolution of the local thermodynamic stability from AERI composite profiles for weakly turbulent ($\overline{\sigma_w}_{,0-100\text{m}} < 0.2\text{m s}^{-1}$) (a) and moderately/strongly turbulent ($\overline{\sigma_w}_{,0-100\text{m}} > 0.2\text{m s}^{-1}$) (b) periods. During LABLE-I, sunset was approximately at 0000 UTC and sunrise was at 1240 UTC, but exact times varied by $\pm$30 over the experiment.

Since the AERI composite θ profiles have been shown to be similar to those from the radiosondes, it is possible to use the AERI's high temporal resolution measurements to examine how the static stability and θ evolve overnight under different turbulence regimes, which is shown in Fig. 3.9. Within the vSBL, a strong surface-based nocturnal inversion develops very early around sunset. Between 0000-0600 UTC, the nocturnal inversion strengthens and slowly becomes deeper,

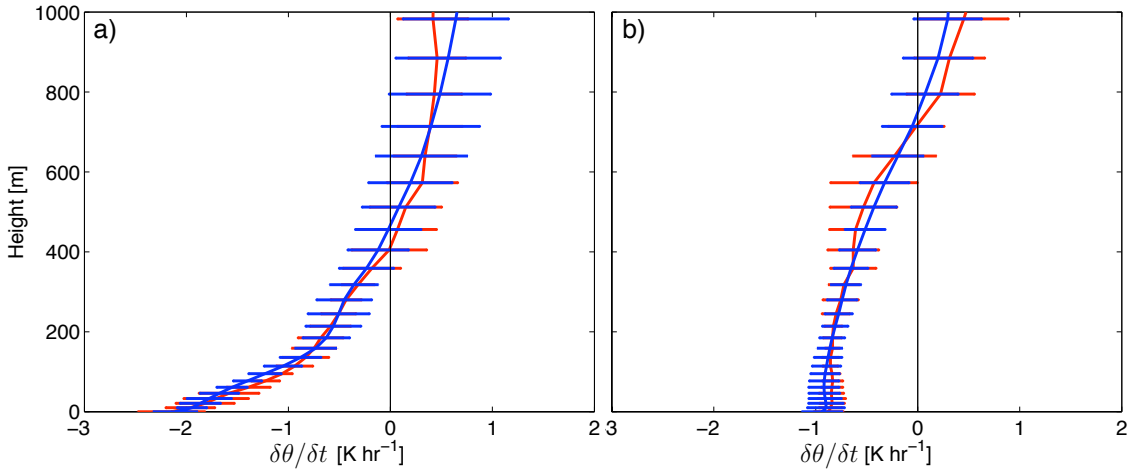

Figure 3.10: Vertical profiles of the mean rate of temperature change from AERI (blue) and radiosonde (red) temperature profiles from 0000Z to 1200 UTC for weakly turbulent (a) and moderately/strongly turbulent conditions (b). Errorbars show the standard deviation of $\delta\theta/\delta t$ at any given height within that turbulent regime.

growing to $\approx$ 200 m. After 0600 UTC, the nocturnal inversion continues to grow slowly in height, but the strength of the near-surface inversion becomes weaker as shown by $\delta\theta/\delta z$ near the surface decreasing with time approaching sunrise in Fig. 3.9a. The time evolution of the static stability within the wSBL shows some features that are similar and some that are different to the vSBL. Within the wSBL, no strong surface-based inversion forms during the entirety of the night as shown in Fig. 3.9b. Around 0000-0200 UTC, a weak surface-based inversion forms that extends through the lowest $\approx$ 100 m. However, that weak inversion erodes over the next couple of hours and is relatively non-existant throughout the rest of the night.

During the entire night, the residual layer above the surface within both SBL regimes tends to become more stable, as shown in Fig. 3.9a, b. While radiative cooling and sensible heat transfer are large and important near the surface, the

increase in stability within the residual layer (300-1000 m) may be from other effects such as differential warm air advection and radiative flux divergence. Since the profiles within this study are all during southerly winds, it is thought that this increasing stability both near the surface and within the residual layer is due to differential temperature advection up to the height of the LLJ. With southerly winds that increase with height up to 600 m (the height of the wind speed maxima in composite wind profiles), the warm air advection would be increasing with height up to the wind maximum within the LLJ. This differential temperature advection with southerly winds would tend to increase stability over time undernearth the LLJ. Additionally, differential radiative flux divergence may slightly contribute to the increase in stability over night throughout this layer up to 1000 m, but this effect can only explain a very small fraction of the increase in stability as clear-air radiative cooling only varies by 0.1 K/hr in the layer from 400–1000 m (Havijärvi 2006). While most studies focus on the effect of radiative flux divergence near the surface within the lowest 100 m (e.g., Ha and Mahrt 2003; Steeneveld et al. 2010; Edwards 2009), Havijärvi (2006) used simulations to show that clear-air long-wave radiational heating and cooling are significant and vary with height throughout the whole troposphere.

To more clearly evaluate which effects (e.g., warm air advection, turbulent heat flux, or radiative cooling) are important for this increase of static stability, the mean rate of temperature change overnight is computed and shown in Fig. 3.10 for both the weakly turbulent and moderate/strongly turbulent SBL. The mean

rate of change is computed by taking the difference between the 0000 UTC and 1200 UTC θ profiles from the AERI and radiosonde and calculating the mean and standard deviation of these temperature differences at each height. Overall, the $\delta\theta/\delta t$ profiles calculated from both the AERI and radiosonde observations are in agreement with each other under both turbulent regimes. Within all the composite $\delta\theta/\delta t$ profiles, the warming rate is smallest and negative (i.e., cooling) at the surface and decreases with height, eventually becoming positive (i.e., warming) at heights just under 1 km. The lowest height where warming first occurs is higher above the ground for the moderate/strong turbulent SBL compared to the weakly turbulent SBL. This is attributed to the fact that when turbulence is stronger, the air that is cooled near or by the surface is mixed through a deeper layer. Also, warmer air from above is mixed downward, reducing the cooling rate at the surface.

Within these mean heating rate profiles, it is difficult to discriminate the individual contributions from turbulent heat transport, clear-air radiative cooling, and warm air advection. Additional measurements of each quantity throughout the entire 1-km layer are necessary to properly identify these effects. However, the warming within the layer of air below 1 km is assumed to primarily be due to warm air advection, since radiative effects and turbulent heat transport would generally result in cooling in this layer at night. Thus, differential temperature advection, with warm air advection increasing with height, is shown to be a large contributing factor to the increase in stability in the SBL and its residual layer up

to 1 km. However, differential clear-air radiative cooling may be an important contributor to this change in stability, as shown by Havijärvi (2006), and may dampen the warming from temperature advection. More studies on the effects of clear-air radiative cooling and how it varies with height are needed to properly understand how it may alter the stability within the lower troposphere, which may influence the development of the convective boundary layer the following day. This could be done in the future by using the rapid radiative transfer model and the AERI-retrieved temperature and moisture profiles to compute the radiative cooling rate.

3.5 Results

The LABLE-I campaign was conducted at the ARM SGP site in north central Oklahoma, USA from 18 September to 13 November 2012. During the experiment the University of Oklahoma deployed several instruments at the SGP central facility to complement the suite of instruments that are permanently installed and maintained by the ARM program. Herein, observations from two Doppler lidars, an Atmospheric Emitted Radiance Interferometer (AERI), sonic anemometers on a 60-m tower, and radiosondes are used to evaluate turbulence and the evolution of the thermodynamic profile within the SBL. Noise within the Doppler lidar measurements is removed by using a method described by Lenschow et al. (2000).

The concept of a threshold wind speed, as introducted by Sun et al. (2012), is investigated using measurements from sonic anemometers and Doppler lidars. Threshold wind speeds, above which bulk-shear turbulence is generated, of similar

magnitude as those provided by Sun et al. (2012) are verified using data from the 60-m tower. Measurements from the Doppler lidars show that a threshold wind speed exists up to $\approx$ 300 m, although it becomes more difficult to determine the threshold value at higher altitudes since it becomes less well-defined. Since the threshold wind speed is a local criterion for differentiating if strong turbulence is generated, the influence of the wind profile above and below a height is investigated to examine its importance. It is found that the threshold wind speed needs to be exceeded near the surface in order for significant turbulence to be generated. Additionally, if the threshold wind speed is exceeded near the surface, then mixing tends to extend up to the height for which the wind speed fails to exceed the threshold wind speed. The threshold wind speed at a higher altitude (i.e., at 200 m) is an important criteria in determining if turbulence is generated and transported through a deeper layer. Generally, if the wind speed at 200 m exceeds the threshold wind speed at that height, then the threshold wind speed is exceeded at lower heights as well and significant turbulence is apparent throughout a deeper layer.

Composite profiles of wind speed, σ_w, and w'^3, all normalized by the wind speed at the base of the low-level jet (or low-level wind maximum), are produced for weak, moderate, and strong turbulence categories. Cases with moderate or strong turbulence profiles exhibit features of a weakly stable boundary layer (wSBL), while those with weak turbulence tend to resemble the very stable boundary layer (vSBL). Turbulence is generated near the surface and transported upwards when turbulence intensity is strong. When mixing is weak, turbulence is

generated either near the surface or aloft depending on if an 'upside-down' or traditional boundary layer is pressent. Within the moderate turbulence regime, the σ_w profile is a mixture of the weak and strong turbulence regimes in that turbulence is generated both at the surface and near the wind speed maximum. The wind profiles in all three turbulence categories are very similar, although wind profiles associated with weak turbulence exhibit greater variability. Differences in measurements of σ_w by the Doppler lidars and the sonic anemometers are observed, and are largely attributed to differences in volume averaging.

Individual and composite profiles of potential temperature from radiosonde and AERI observations are compared. While differences between the individual AERI and radiosonde profiles are apparent, since the AERI tends to smooth out sharp gradients, composite thermodynamic profiles from the AERI tend to agree well those from the radiosonde for both the wSBL and vSBL. By using mean θ profiles from the AERI, differences in the thermodynamic evolution of the wSBL and vSBL are explored. Around sunset in the vSBL, a strong surface-based inversion forms that strengthens and grows in depth for the first half of the night. Around midnight, the inversion continues to deepen but the static stability near the surface begins to decrease, which continues throughout the rest of the night. Within the wSBL, no strong surface-based inversion forms. A weak inversion forms in the hours after sunset, but it quickly diminishes and the temperature profile near the surface tends to be isothermal for much of the night. In both the wSBL and the

vSBL, the static stability within the residual layer ($\approx$ 400-1000 m) tends to increase overnight. While the reasons for this are not entirely clear, it is thought that differential radiative flux divergence and differential warm air advection causes static stability in this layer to increase over time. Since data used here are from time periods when the winds were southerly, the southerly wind speed increasing with height would result in stronger warm air advection at higher heights for a typical north-south temperature gradient.

Chapter 4

Different Characteristics and Evolution of Turbulent and non-Turbulent Southerly Low Level Jets

4.1 Background

As discussed within Ch. 3, the nocturnal PBL and any associated LLJ have very different characteristics depending on the strength of the turbulent mixing associated with the LLJ. However, to my knowledge, no one previously has examined in detail how LLJs evolve differently depending on this quantity of near-surface turbulent mixing. Within this chapter, the evolution of the LLJ and its relation to thermodynamic features, such as inversions, are carefully examined.

Previous studies have come to mixed conclusions on where the LLJ is located with respect to thermodynamic features. Baas et al. (2009) found that the LLJ is typically situated close to the top of the inversion layer, which is consistent with the Blackadar (1957) inertial oscillation theory theory. Bonner (1968) and Whiteman et al. (1997) both used radiosonde climatologies to study the Great Plains LLJ, and found that the height of the LLJ is typically above the tops of the surface-based inversion, with considerable variability. Andreas et al. (2000) examined LLJs that formed within the Antarctic Weddell Sea, which were caused by inertial oscillations, and found that the LLJs were embedded within the inversion layer itself. In

addition to these relationship with nocturnal inversions, Banta et al. (2002) found that the height of the LLJ sometimes followed the terrain and sometimes stayed constant with height with respect to sea level. It is possible that the LLJ may follow one type of surface (ground, height MSL, or even isentropic surface) for a strongly turbulent LLJ, and another for a weakly turbulent LLJ.

The data that is presented here was collected during the LABLE-I campaign, which is outlined within Sect. 3.2. Continuous thermodynamic profiles are provided by the AERI, while both σ_w^2 and wind profiles are derived from DL observations. In addition, radiosonde observations are used for investigating the relationship between inversions and the height of the LLJ.

Within this chapter, the following questions will be addressed:

1. Are there any general synoptic scale differences between strongly and weakly turbulent LLJs?

2. Do the height and strength of the LLJ evolve differently for strongly turbulent and weakly turbulent LLJs? If so, why do they evolve differently?

3. Since the literature is mixed on where the LLJ forms with respect to inversions, could differences be attributed to whether the LLJ is strongly turbulent or not? If so, what are those differences exactly?

To address these questions, three case studies each of strongly and weakly turbulent LLJs are presented within Sect. 4.2. For each case, the synoptic setup and the evolution of the LLJ are discussed. More general results for differences in

weakly and strongly turbulent LLJs will be presented in Sect. 4.3. The evolution of the height and strength of the LLJ is discussed, including a discussion of a different process that may govern how weakly turbulent LLJs evolve. The relation of the LLJ to any surface-based or nocturnal inversion is also discussed in Sect. 4.3.

4.2 Case Studies

To investigate how LLJs evolve differently when near-surface turbulence associated with the LLJs is strong or weak (based on the definition in Sect. 3.4.2), several nights where a LLJ formed will be investigated closely for comparison. Three nights when low-level turbulence intensity was weak, and three when the low-level turbulence was strong, are presented. For the cases presented, no clouds beneath 3-m were detected over the SGP ARM site by a ceilometer at any point during the night. However, based on infrared satellite observations, high cirrus were observed at some point during every night except for 8 November. For each case, the synoptic setup and the evolution of wind speed, wind direction, vertical velocity variance, and thermodynamic profiles are shown and discussed. The presented cases are chosen to represent the variability of the LLJ within each turbulence category, as observed during LABLE-I. Throughout the rest of the chapter, Z_{LLJ} and V_{LLJ} will be used to characterize the LLJ height and strength, which were previously defined within Sect. 3.4.2.

4.2.1 Weakly Turbulent Southerly LLJs

Over the course of LABLE-I, twelve weakly turbulent southerly LLJs with maximum wind speeds, V_{LLJ}, greater than 12 m s^{-1} were observed. While these are classified as weakly turbulent based on the 0–100 m averaged σ_w ($\overline{\sigma_w}_{,0-100\mathrm{m}}$) from the DL, several of these LLJs were associated with intermittent periods of elevated mixing that was disconnected from the surface. For comparison with LLJs of similar magnitude but with strong low-level mixing, the LLJs shown here are all associated with a V_{LLJ} greater than 20 m s^{-1}. On several nights, weaker LLJs (with a V_{LLJ} less than 20 m s^{-1}) developed within the lowest 200 m, which will not be discussed here.

4.2.1.1 9 October, 2012

Synoptic Setup At 0000 UTC on 9 October 2012, a surface low pressure system was located over northern Minnesota associated with a 500-mb trough as shown in Fig. 4.1. A cold front, associated with the low-pressure system, was located to its southwest through central Nebraska. Further south, near the ARM SGP site, flow at 500-mb and 700-mb was more zonal. However, at 850-mb, a shortwave trough is located over eastern Colorado and New Mexico. Overnight, as this 850-mb trough approached, a secondary low formed in western Kansas, which is evident on the surface and 850-mb charts at 1200 UTC. This approaching low-level trough and surface-low lead to an increase in the pressure-gradient force and

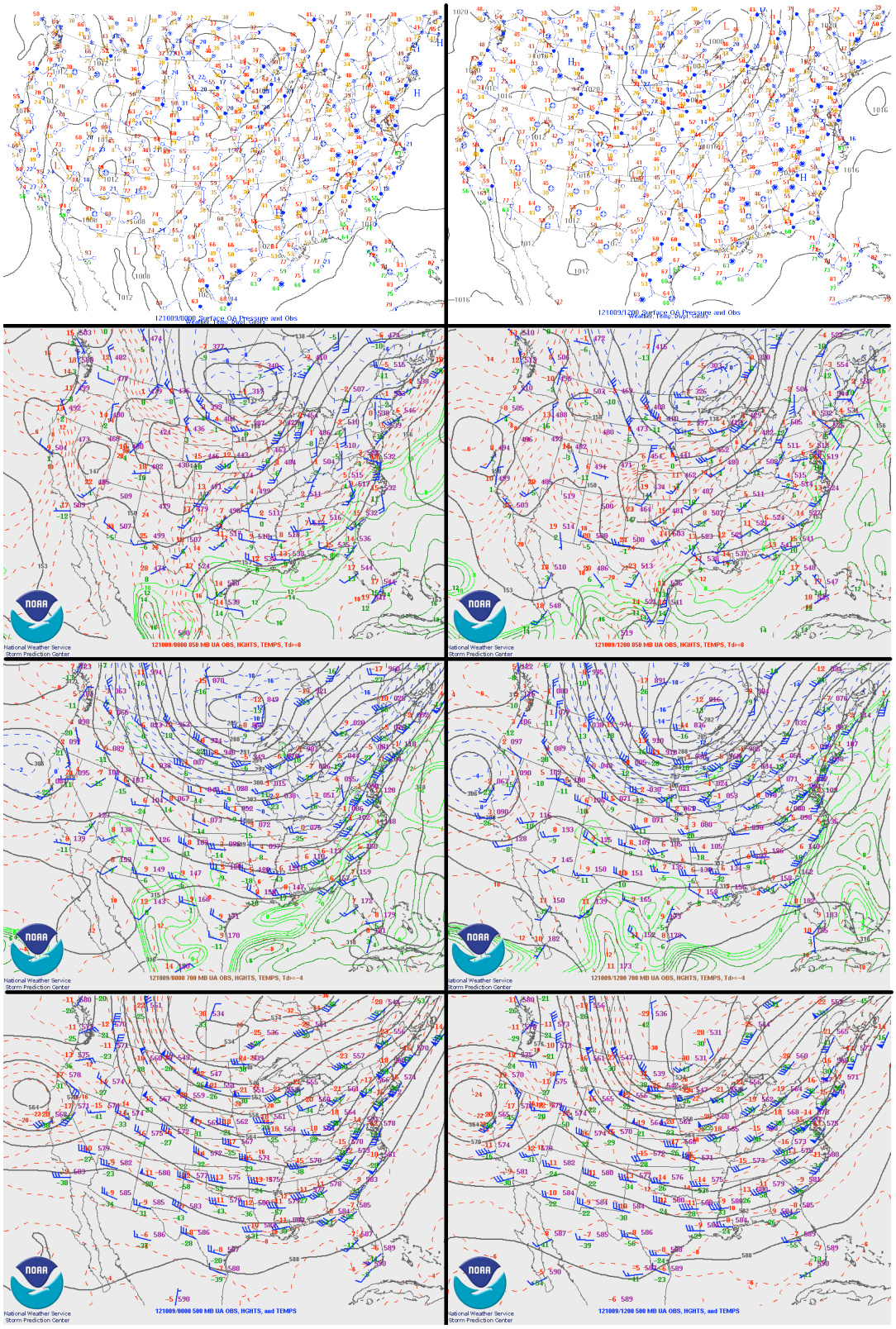

Figure 4.1: Surface, 850-mb, 700-mb, and 500-mb map (top to bottom) from 0000 UTC (left) and 1200 UTC (right) on 9 October 2012. Maps are from the Storm Prediction Center map archive, which are all available online at http://www.spc.noaa.gov/obswx/maps/ .

stronger synoptic-scale forcing over the course of the night over the SGP ARM site.

LLJ Evolution The LLJ that formed on 9 October slowly strengthened overnight from 0000 UTC to 1000 UTC, when wind speed reached a maximum, as shown in Fig. 4.2a. Coincident with the slow strengthening of the LLJ, the stability within the layer where the LLJ formed also increased overnight. This increase in stability is due to radiative cooling at the surface, and warming in the layer from 600-1000 m likely due to warm air advection. Over this time period, the LLJ core (defined as the depth where the wind speed is greater than 75% of V_{LLJ}), as shown by the white dashed lines in Fig. 4.2, became more narrow over time. Additionally, Z_{LLJ} tended to follow an isentropic surface throughout the night. As the surface-based inversion grew deeper overnight, Z_{LLJ} also increased.

Throughout the night, the wind direction within the LLJ core remained relatively constant (Fig. 4.2b. Above the LLJ, the wind direction generally turned westerly with height, until about 1000 UTC when the approaching trough shifted the winds to become mostly southerly above 1 km. The directional change in wind direction with height within the core of the LLJ remained relatively constant throughout the night; that is, as the LLJ core became more narrow overnight, the directional shear $d\varphi/dz$ increased as the depth of the core decreased.

Just before sunset, mixing throughout the PBL rapidly decayed as shown by the large decrease in σ_w^2 in the two hours before 0000 UTC in Fig. 4.2. After this, through much of the night, values of σ_w^2 below the jet remained quite small and

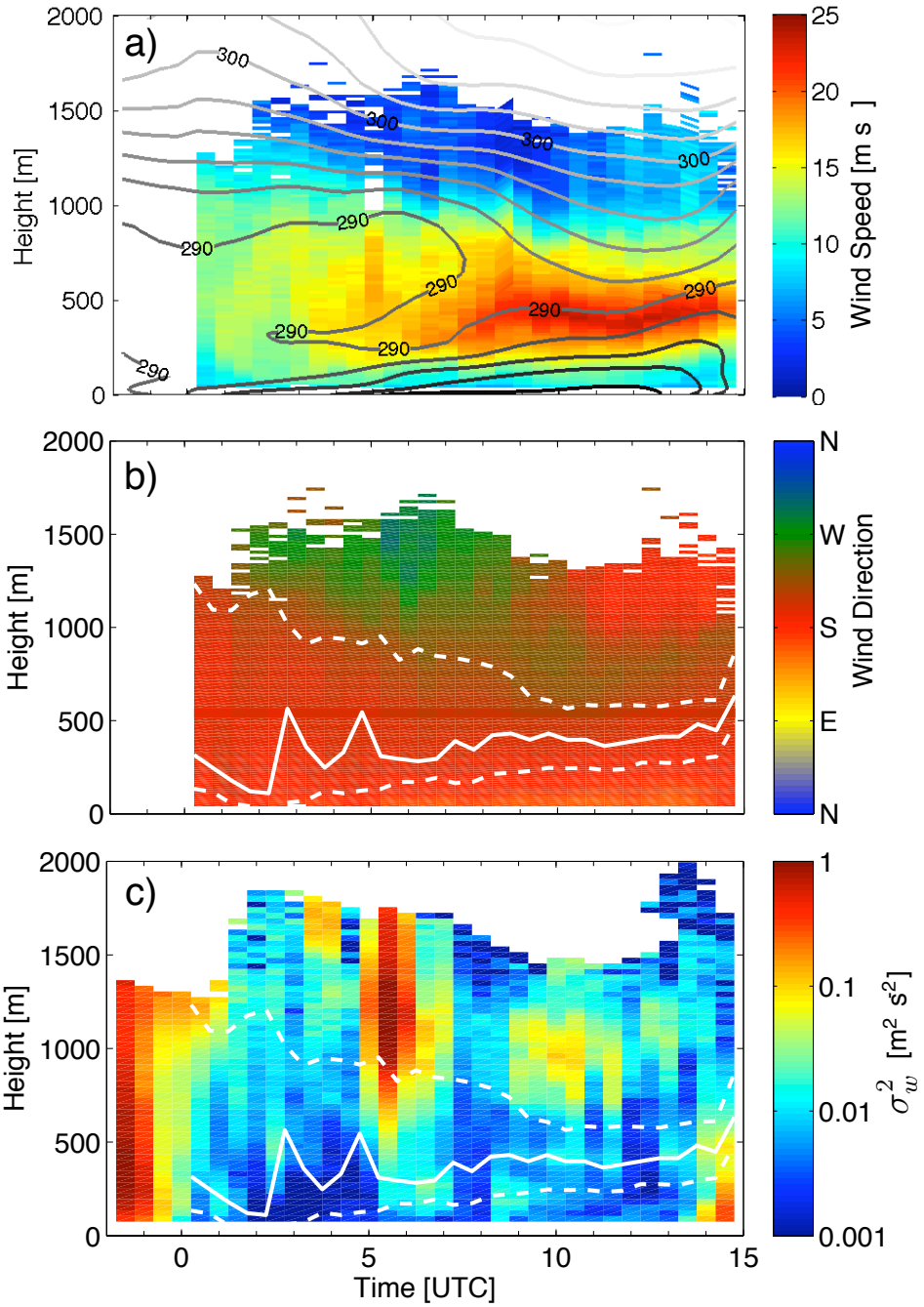

Figure 4.2: Time-height cross sections of wind speed overlaid with isentropes contoured every 2 K where darker colors indicate lower potential temperature (a), wind direction (b), and vertical velocity variance (c) on 9 October 2012. The solid white lines indicate the height of the LLJ, while the dashed lines show where the wind speed is 75% of the wind speed maximum, indicating the relative width of the LLJ. Sunset was at 0001 UTC.

less than 0.01 m^2 s^{-2}. Shortly after 0500 UTC, when the LLJ starts to form and strengthen, an increase in σ_w^2 below the LLJ is observed. In addition, pronounced waves with periodic rising and sinking motion became apparent above the LLJ starting at 0500 UTC and continued intermittently throughout the rest of the night. The waves were identified on time-height cross sections of w and SNR from the DL. The waves were not pure, as turbulence was generated within the layer where they were present through a process discussed by Finnigan et al. (1984).

4.2.1.2 21 October, 2012

Synoptic Setup On 21 October 2012, the 500-mb pattern at 0000 UTC indicated that northern Oklahoma was located between a pronounced trough to the east and a weaker trough to the west (see Fig. 4.3). Throughout the night and by 1200 UTC, the trough to the west was approaching and was located over the Baja of California. At lower levels, a 850-mb trough is evident to the west of the ARM SGP site, over the panhandle of Texas. Throughout the night, this trough strengthened and propagated slightly eastward, but the trough axis still remained to the west of the ARM SGP site. This lead to a larger pressure gradient force overnight, resulting in winds becoming stronger at the lower levels. Associated with this 850-mb trough, a weak surface low began to form over the Panhandle of Oklahoma.

LLJ Evolution Similarly to the LLJ that developed on 9 October, the LLJ on 21 October did not develop until about 6-hr after sunset, as shown in Fig. 4.4. While the wind speed quickly became larger right after sunset through a layer

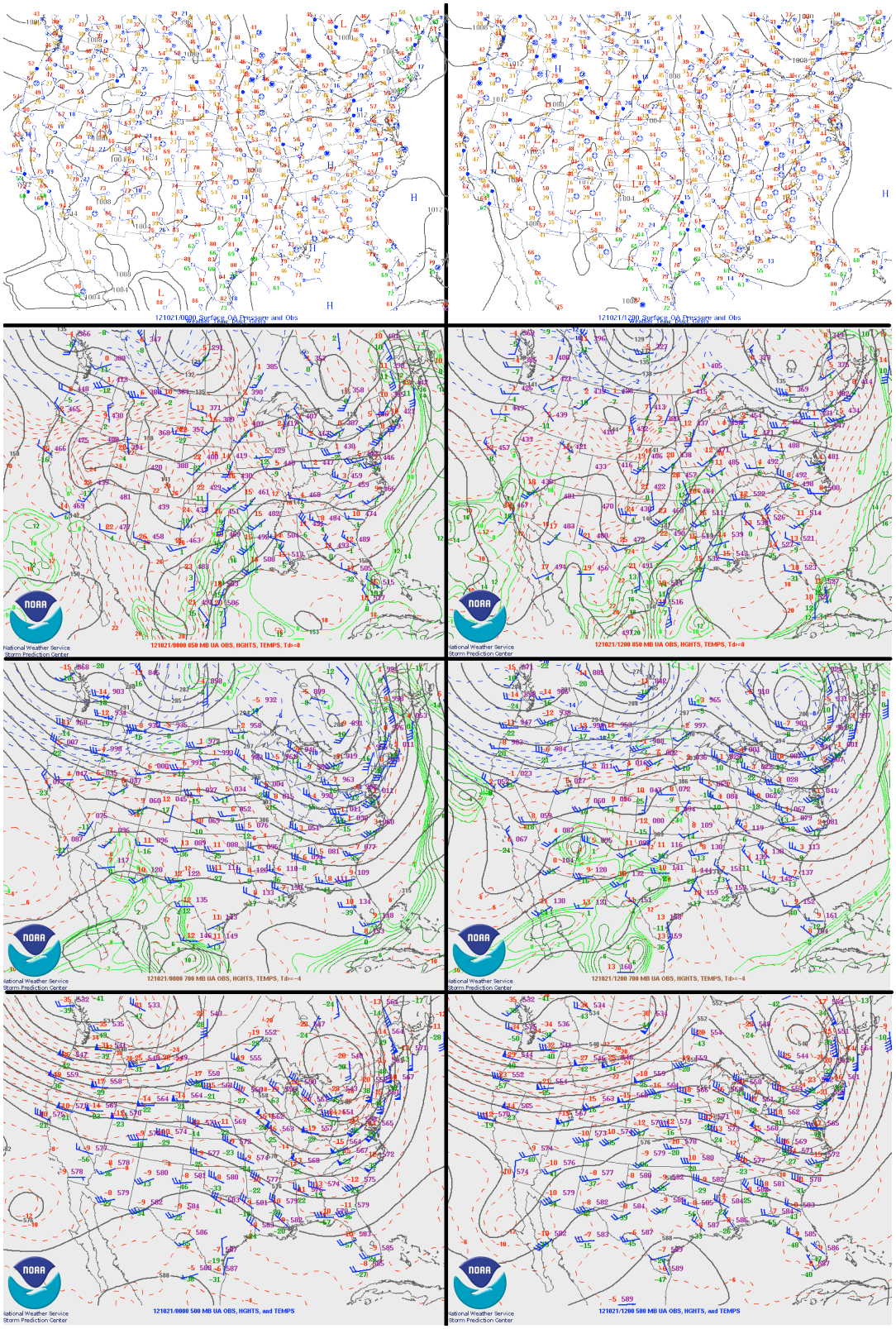

Figure 4.3: Surface, 850-mb, 700-mb, and 500-mb map (top to bottom) from 0000 UTC (left) and 1200 UTC (right) on 21 October 2012. Maps are from the Storm Prediction Center map archive.

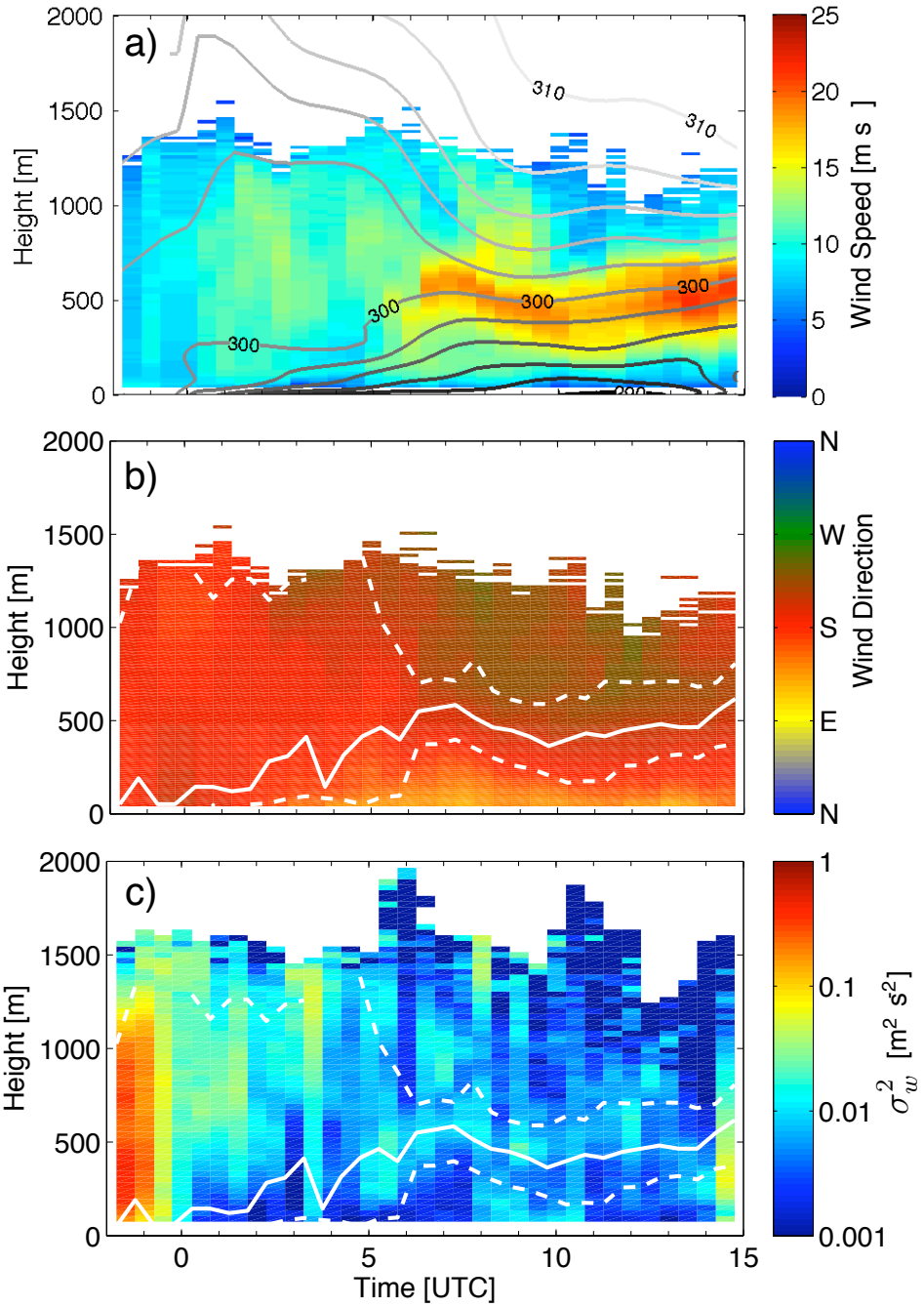

Figure 4.4: Time-height cross sections of wind speed overlaid with isentropes contoured every 2 K where darker colors indicate lower potential temperature (a), wind direction (b), and vertical velocity variance (c) on 21 October 2012. The solid white lines indicate the height of the LLJ, while the dashed lines show where the wind speed is 75% of the wind speed maximum, indicating the relative width of the LLJ. Sunset was at 2345 UTC.

extending from just above the surface to 1 km, which is to be expected with the rapid reduction in frictional effects, the wind speed within that layer remained relatively constant with height and time for several hours. At around sunset when the wind speed increased, a surface-based inversion began to form in conjunction with the decay of mixing throughout the PBL. While turbulent mixing rapidly decreased at the surface, values of σ_w^2 in the layer of air between 250–1200 m remained fairly large (≈ 0.05 m^2 s^{-2}) for several hours after sunset.

In the hours after sunset, the surface based inversion continued to become stronger and deeper over time. However, until 0500 UTC, the layer from 250–1200 m remained relatively dry adiabatic, which coincided with the aforementioned period when turbulent mixing within this layer persisted. During this time period, the wind direction remained relatively constant with height, although a veering profile began to develop after 0500 UTC when the elevated mixing decayed.

Between 0600–0700 UTC, a well-defined LLJ rapidly formed as the maximum wind speed increased from 12 m s^{-1} to 20 m s^{-1} over a few hours. This coincided with a large increase in stability in the layer from 500–1200 m over a very short period of time. While the reason for the rapid increase in elevated stability is not entirely clear, it is likely due to significant warm air advection increasing with height or large-scale subsidence. As the LLJ strengthened significantly between 0600–0700 UTC, directional wind shear also increased as $d\varphi/dz$ became larger,

especially within the LLJ core. The wind became more westerly with height. During this time period, values of σ_w^2 remain relatively low throughout the lowest 1-km. Although, there are some periods of slightly enhanced mixing intermittently.

4.2.1.3 8 November, 2012

Synoptic Setup A deep, large 500-mb trough was located over the eastern United States on 8 November 2012. The mid- and upper-level flow at 500 mb was northerly in northern Oklahoma on the back side of the trough at 0000 UTC, but the wind direction became more westerly and southwesterly as the trough propagated eastward further from the ARM SGP site overnight. At the lower levels, a 850-mb shortwave trough was evident at 0000 UTC over eastern Colorado and the Texas panhandle. Overnight, this 850-mb trough propagated eastward, increasing the pressure gradient in northern Oklahoma. With this, a low-pressure system over the Oklahoma panhandle formed. The synoptic evolution in the lower levels is similar to that which occurred on 21 October.

LLJ Evolution Similarly to the LLJs on 9 and 21 October, the LLJ on 8 November developed several hours after sunset after a strong surface-based inversion already formed, as shown in Fig. 4.6. After the strong daytime turbulent mixing within the PBL diminished around sunset, the wind speed within the lowest 1-km slowly increased throughout the night. The maximum wind speed of $\approx$28 m s^{-1} occurred at 1400 UTC, shortly before daytime mixing redistributed the momentum through a deeper layer. As the surface-based inversion grew throughout the

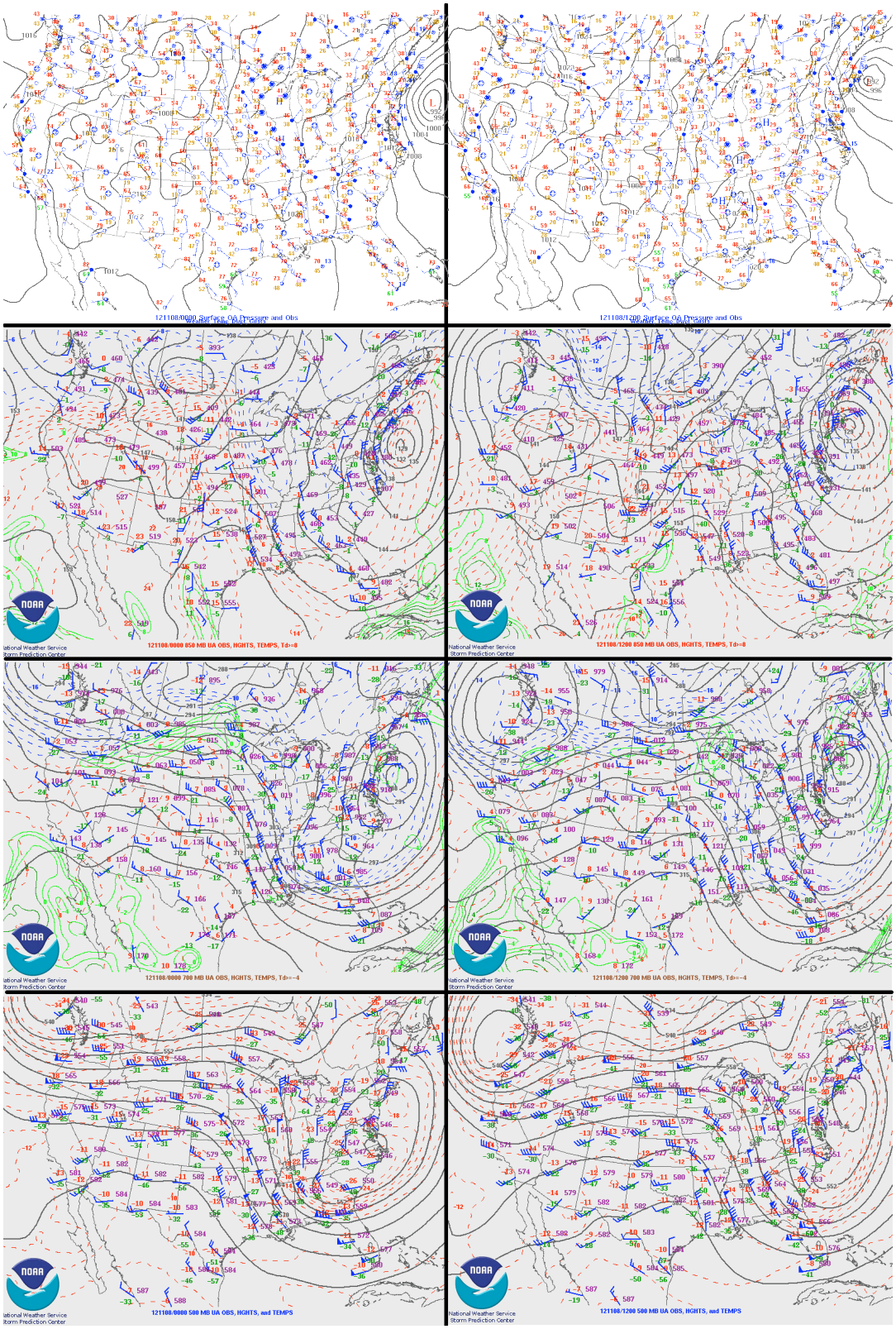

Figure 4.5: Surface, 850-mb, 700-mb, and 500-mb map (top to bottom) from 0000 UTC (left) and 1200 UTC (right) on 8 November 2012. Maps are from the Storm Prediction Center map archive.

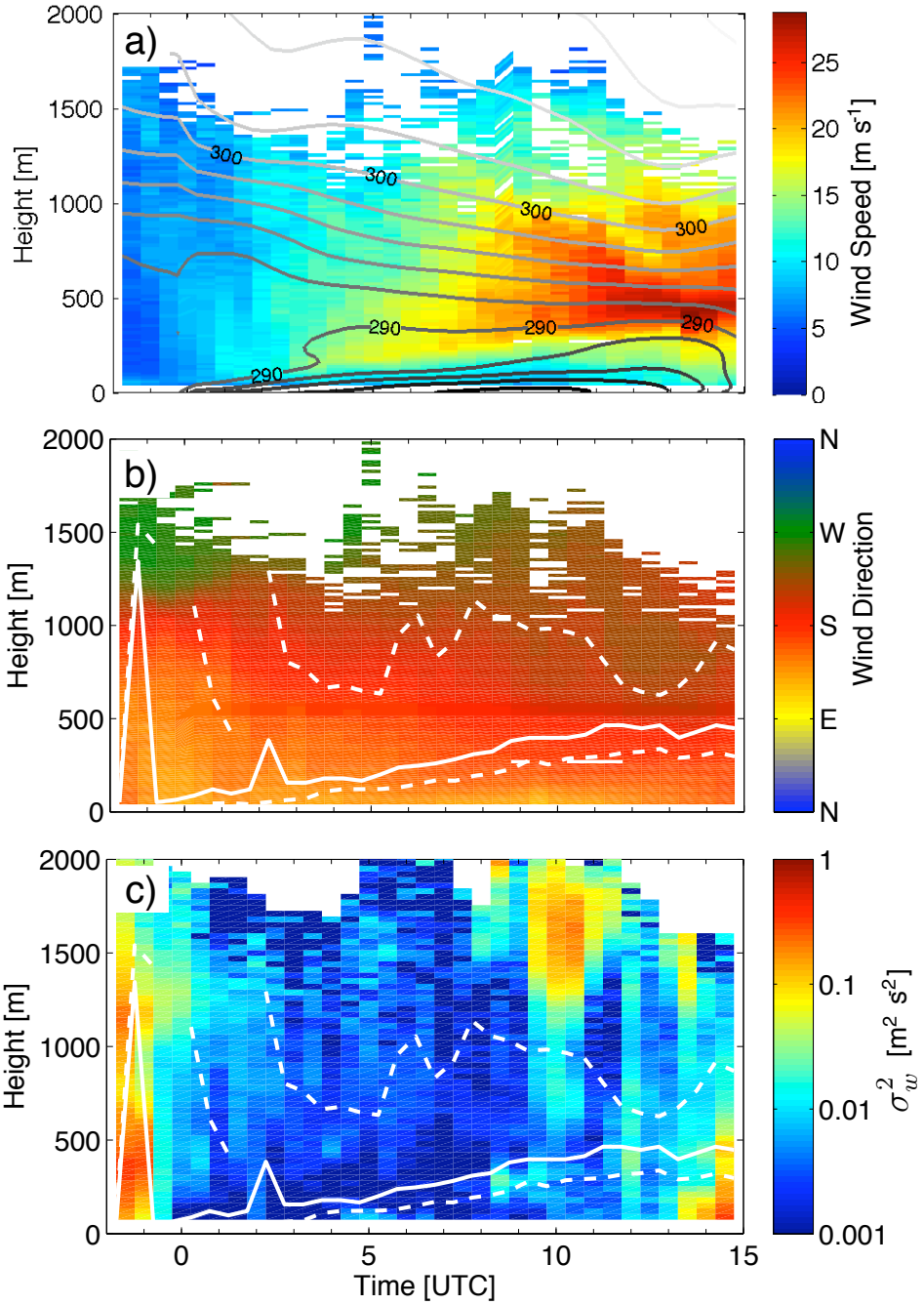

Figure 4.6: Time-height cross sections of wind speed overlaid with isentropes contoured every 2 K where darker colors indicate lower potential temperature (a), wind direction (b), and vertical velocity variance (c) on 8 November 2012. The solid white lines indicate the height of the LLJ, while the dashed lines show where the wind speed is 75% of the wind speed maximum, indicating the relative width of the LLJ. Sunset was at 2326 UTC.

night, Z_{LLJ} generally increased as well, coinciding well with the top of the nocturnal inversion. Additionally, as stability slowly increased throughout the night, V_{LLJ} tended to increase as well.

Around sunset, a large sharp wind shift was apparent at 1200 m. This wind shift is located at the top of the PBL, wherein the winds below are well-mixed. As the PBL collapsed and daytime mixing ceased, the large $d\varphi/dz$ at this height slowly decreased over the following hours. During this decrease in $d\varphi/dz$, elevated mixing is still evident within the layer of the strong directional shear, even though values of σ_w^2 closer to the surface have decreased substantially. The directional shear is likely sustaining turbulence within this layer, until $d\varphi/dz$ has decreased substantially as it does over the next few hours. Throughout the rest of the night, the wind direction within the lowest 1-km as a whole generally becomes more westerly with both height and time.

Similarly to the previous two LLJs associated with weak turbulence, values of σ_w^2 remain relatively small within and below the LLJ core for most of the night. Although, there are a few periods of intermittently generated turbulence, such as at 0800 UTC at 250 m. The higher values of σ_w^2 above 1 km at around 1000 UTC are due to waves passing over the SGP site, visible on time-height cross-sections of w.

4.2.2 Strongly Turbulent LLJs

Strongly turbulent LLJs were observed on nine nights during LABLE-I. Many of these low-level jets occurred on consecutive periods, often preceded by a weakly-turbulent LLJ as the synoptic setup slowly evolved to support highly-turbulent LLJs with stronger winds. For example, the nights of 22–24 October and 9–11 November all had LLJs that generated strong turbulence below their core. Most of the time, strong near-surface turbulence was persistent throughout the whole night. However, on a few occasions the near-surface σ_w^2 decreased to very low values after sunset before mixing increased again, such as on 9 November that is discussed in Sect. 4.2.2.3.

4.2.2.1 22 October, 2012

Synoptic Setup A large-scale 500-mb trough, with several imbedded shortwave troughs, was located over the west coast of the United States on 22 October, 2012. A shortwave propagated past northern Oklahoma early in the night, although the upper-level flow remained southwesterly with the main trough farther to the west the entire night. Similar troughs were also apparent at 700-mb. Associated with these mid-level troughs, a negatively tilted trough at 850-mb, which became a closed-low overnight, was evident to the northwest of the SGP ARM site. A cold front slowly advanced to the south through Kansas overnight, but remained to the north of the Oklahoma border.

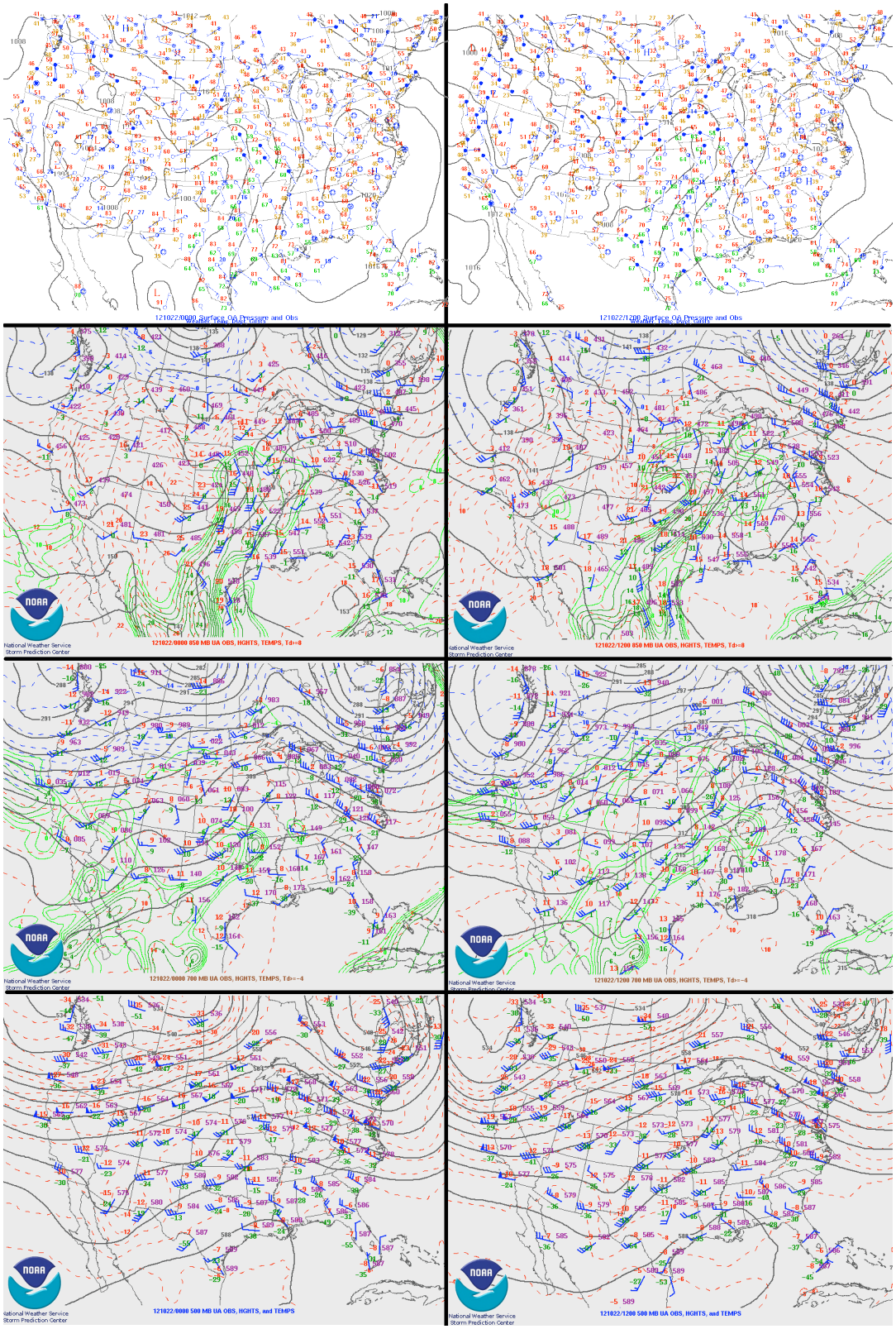

Figure 4.7: Surface, 850-mb, 700-mb, and 500-mb map (top to bottom) from 0000 UTC (left) and 1200 UTC (right) on 22 October 2012. Maps are from the Storm Prediction Center map archive.

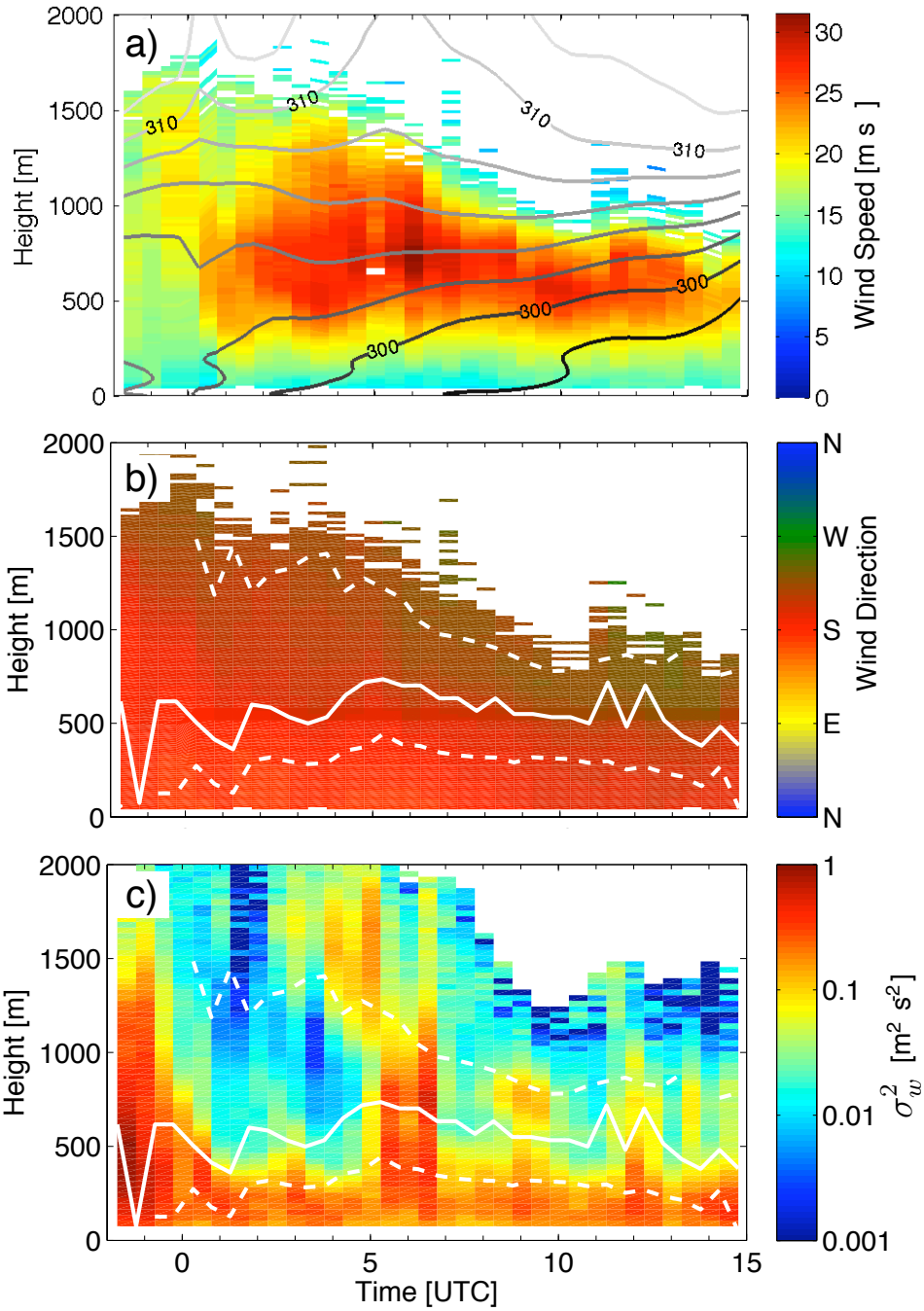

Figure 4.8: Time-height cross sections of wind speed overlaid with isentropes contoured every 2 K where darker colors indicate lower potential temperature (a), wind direction (b), and vertical velocity variance (c) on 22 October 2012. The solid white lines indicate the height of the LLJ, while the dashed lines show where the wind speed is 75% of the wind speed maximum, indicating the relative width of the LLJ. Sunset was at 2344 UTC.

LLJ Evolution The LLJ on 22 October rapidly developed after sunset, as shown in Fig. 4.8. For most of the night, the LLJ remained relative broad. The core of the jet where winds were greater than 75% of V_{LLJ} remained greater than 1 km deep for several hours after sunset. Throughout the night, the LLJ became more focused, as the depth of the core decreased. During this time, the LLJ strengthened through about 0600 UTC when Z_{LLJ} reached a maximum. Afterwards, V_{LLJ} decreased gradually throughout the rest of the night. Throughout the night, the wind direction remained relatively southerly near the surface. Directional shear increased throughout the night, as $d\varphi/dz$ reached a maximum in the early morning hours before sunset.

Throughout the entire night, no strong surface-based inversion formed, although the entire layer below 600 m slowly cooled off over night. Concurrently, values of σ_w^2 underneath the jet remained relatively large (greater than 0.1 m^2 s^{-2}) throughout the entire night. The absence of a strong surface-based inversion enabled the mixing to continue, which naturally helped to prevent the establishment of a low-level inversion by transporting warmer air towards the surface that was radiatively cooling. Several times throughout the night, such as at 0500 UTC and 0900 UTC, waves were apparent within and above the LLJ core. Interactions between these waves and the PBL enhanced turbulent mixing in the lower levels during these times. The observed waves may be an undular bore produced by the cold front in Kansas impinging on the nocturnal stable layer (e.g. Clarke et al. 1981; Koch et al. 1991).

4.2.2.2 24 October 2012

Synoptic Setup 24 October was the third and final consecutive day where a strong LLJ, which associated with substantial mixing underneath it, formed while a large-scale 500- and 700-mb trough was located over the western United States. At 850-mb, a closed-low was located over northeastern Colorado at 0000 UTC, and propagated to the east into western Kansas by 1200 UTC. With this, a strong cold front was surging to the south overnight and was located over northwestern Kansas by 1200 UTC. As the 850-mb trough approached overnight, the winds became more westerly.

LLJ Evolution The LLJ on 24 October developed particularly early, as a pronounced wind speed maximum was evident at 2200 UTC at 600 m in Fig. 4.10. This LLJ developed 2 hrs before sunset, during the EET that began several hours before sunset. The LLJ strengthened until ≈0300 UTC, when V_{LLJ} reached a maximum and remained relatively constant until 1000 UTC, when the LLJ began to weaken. The height of the LLJ was approximately constant overnight at 500 m, while the depth of the core decreased slowly overnight as the LLJ became more concentrated. Similarly to previously discussed LLJs, the wind direction became more westerly with height overnight, and $d\varphi/dz$ was largest at ≈1200 UTC.

Since substantial turbulent mixing below the LLJ continued throughout the night, no strong surface-based inversion formed again. Still, stability increased below Z_{LLJ} as air cooled near the surface was distributed throughout the entire

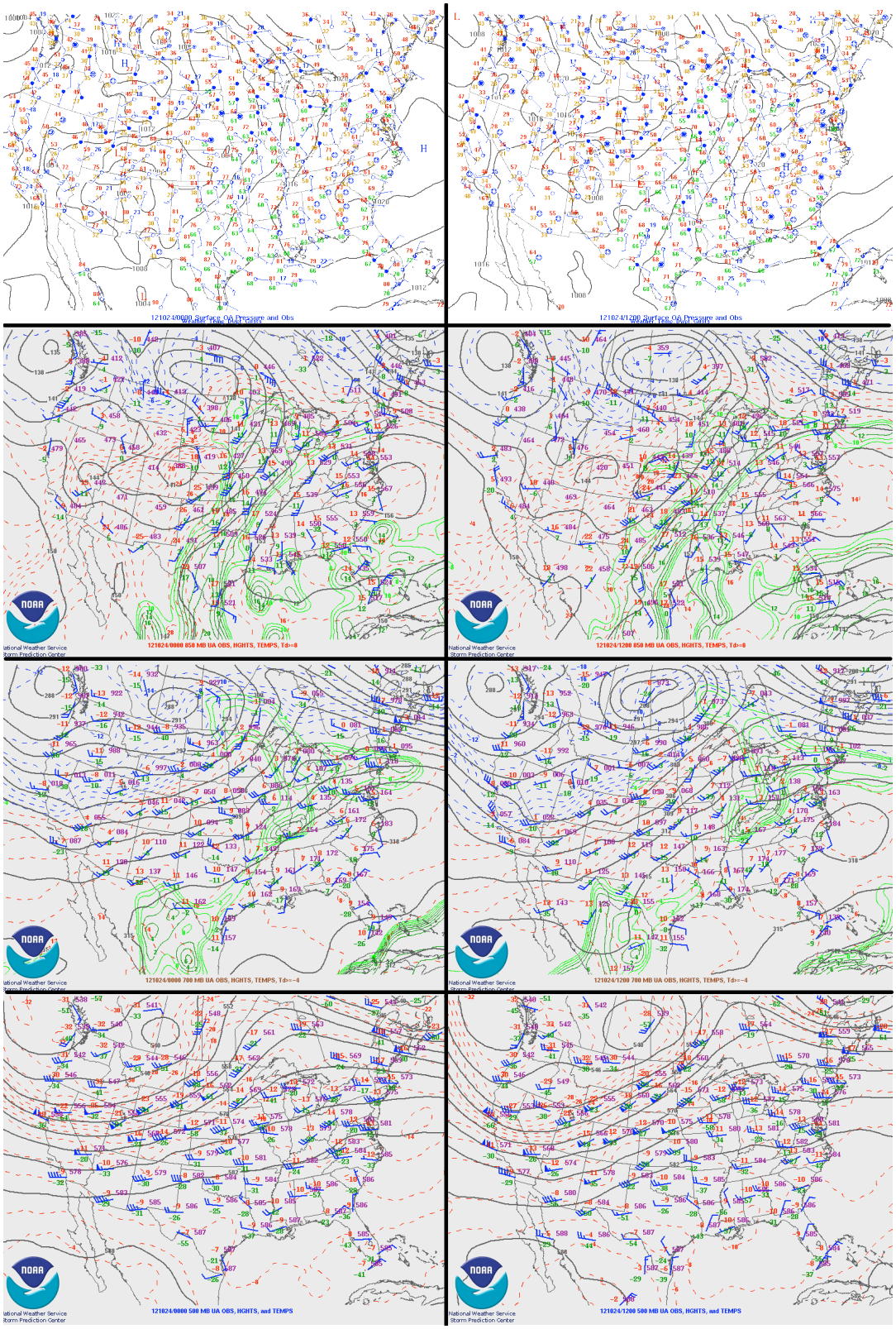

Figure 4.9: Surface, 850-mb, 700-mb, and 500-mb map (top to bottom) from 0000 UTC (left) and 1200 UTC (right) on 24 October 2012. Maps are from the Storm Prediction Center map archive.

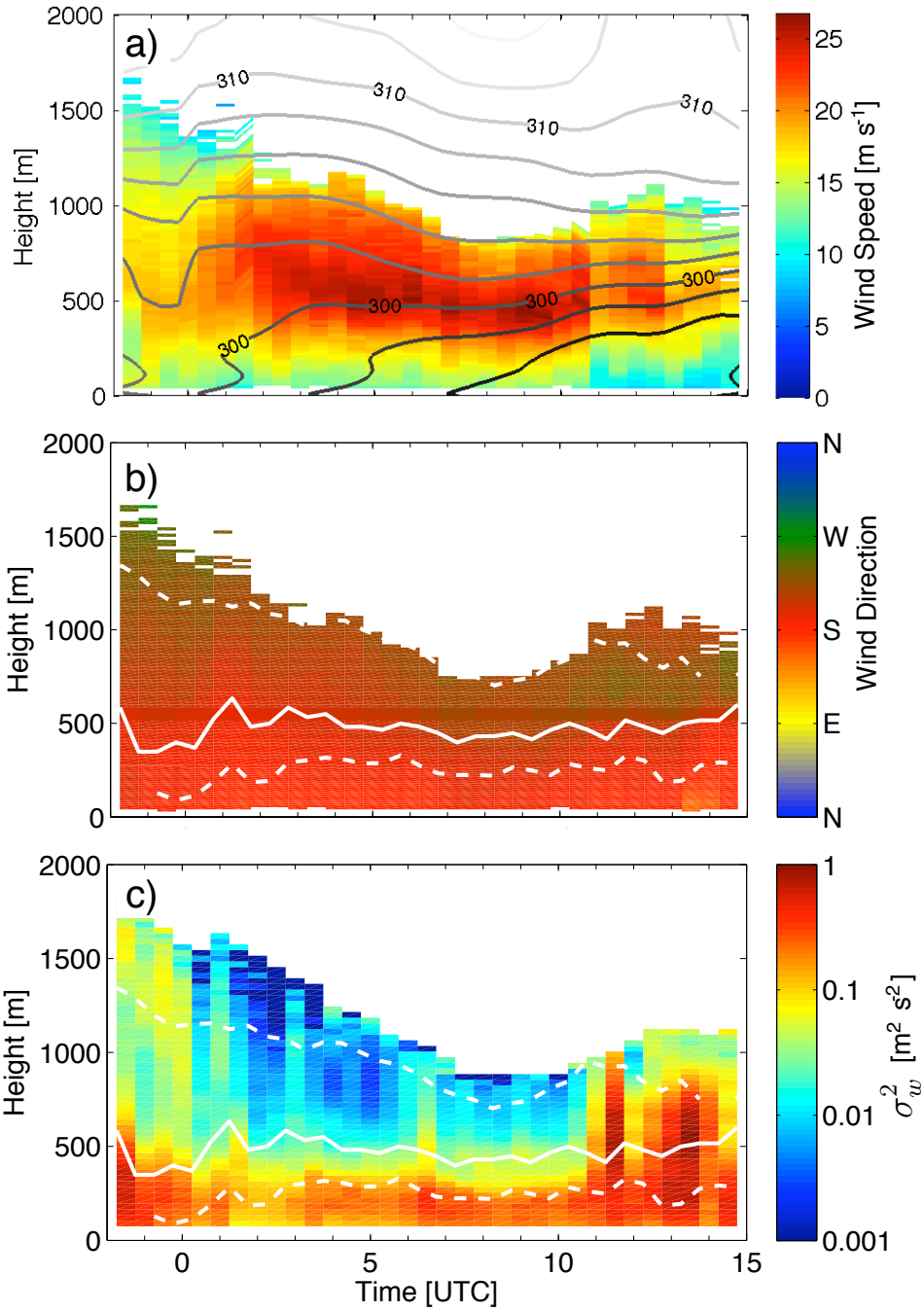

Figure 4.10: Time-height cross sections of wind speed overlaid with isentropes contoured every 2 K where darker colors indicate lower potential temperature (a), wind direction (b), and vertical velocity variance (c) on 24 October 2012. The solid white lines indicate the height of the LLJ, while the dashed lines show where the wind speed is 75% of the wind speed maximum, indicating the relative width of the LLJ. Sunset was at 2342 UTC.

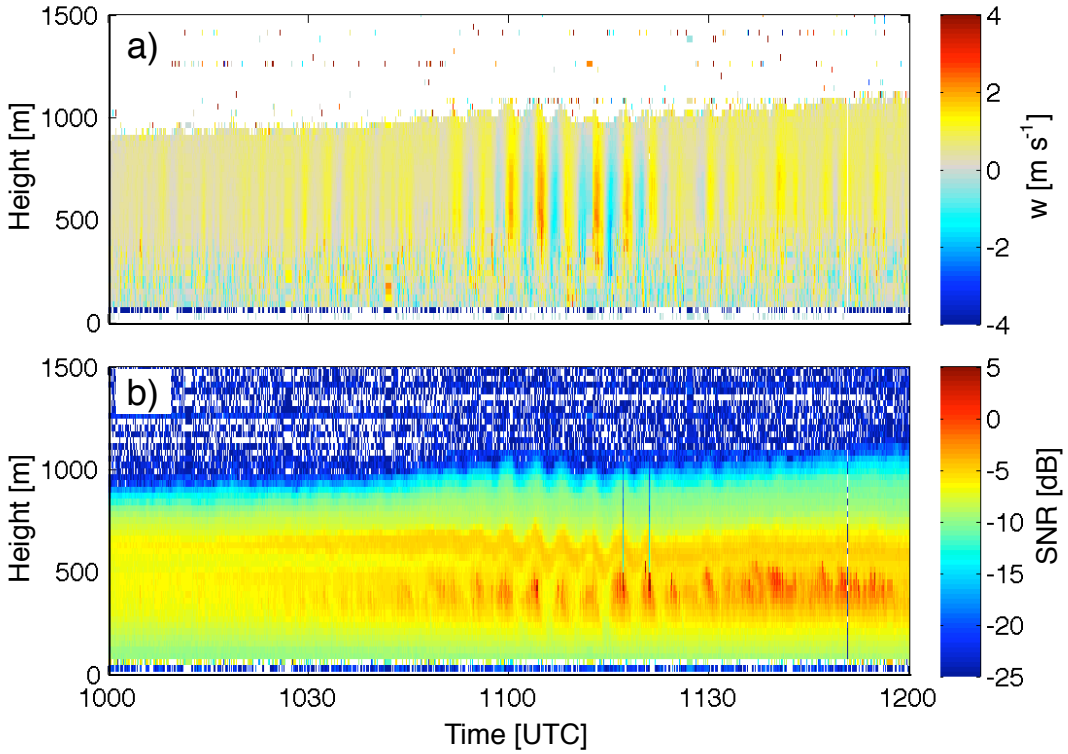

Figure 4.11: Time-height cross sections of w (a) and SNR (b) for a wave that passed over the SGP ARM site on 24 October.

layer by the turbulent mixing. Above Z_{LLJ}, where values of σ_w^2 were substantially lower, the layer of air generally warmed likely due to warm air advection. The increase in σ_w^2 through a deeper layer up to 1 km at 1100 UTC is due to waves that moved over the ARM SGP site, which are apparent in the DL observations of w, shown in Fig 4.11. The waves shown here are similar to the signature, distinct periodic rising and sinking motions, shown by waves on other nights.

4.2.2.3 9 November 2012

Synoptic Setup On 9 November 2012, large troughs were located on both coasts of the United States, with Oklahoma being approximately equally spaced between both at 0000 UTC. By 1200 UTC, both troughs had propagated eastward, and

the 500-mb wind became southwesterly over Oklahoma, indicated that the trough was affecting the area. At 700- and 850-mb, a shortwave trough was located to the northwest of the ARM SGP at 0000 UTC, and it propagated over the area overnight. During this time, the pressure gradient became larger over northern Oklahoma, which contributed to the lower-level winds strengthening over the night. At the surface, a weak and stationary cold front was located over central Kansas.

LLJ Evolution The evolution of the LLJ on 9 November was different than the previous two strong LLJs that maintained turbulent mixing overnight. The LLJ developed more slowly, as shown in Fig. 4.13, as V_{LLJ} did not increase rapidly after sunset. Starting at 0100 UTC and until 0600 UTC, V_{LLJ} rapidly increased from 16 m s^{-1} to 32 m s^{-1}. Additionally, the height of the LLJ subsided during that time period from $\approx$1 km to 600 m. After 0800 UTC, V_{LLJ} started to decrease which continued throughout the rest of the night. Over the entire night, the wind direction near the surface remained south-south-westerly. However, above 500 m, the wind direction became more westerly overnight, likely in response to the passage of a 850-mb shortwave trough. Similarly to previous nights, values of $d\varphi/dz$ increased over the course of the night as directional shear increased.

While no strong surface-based inversion formed on 9 November, a weak inversion began to form shortly after sunset. During this time period the near-surface wind speed was small, and turbulent mixing that was present during the day was rapidly decaying throughout the entire depth of the PBL. While the near-surface turbulent mixing never became as small as it was during the weakly-turbulent

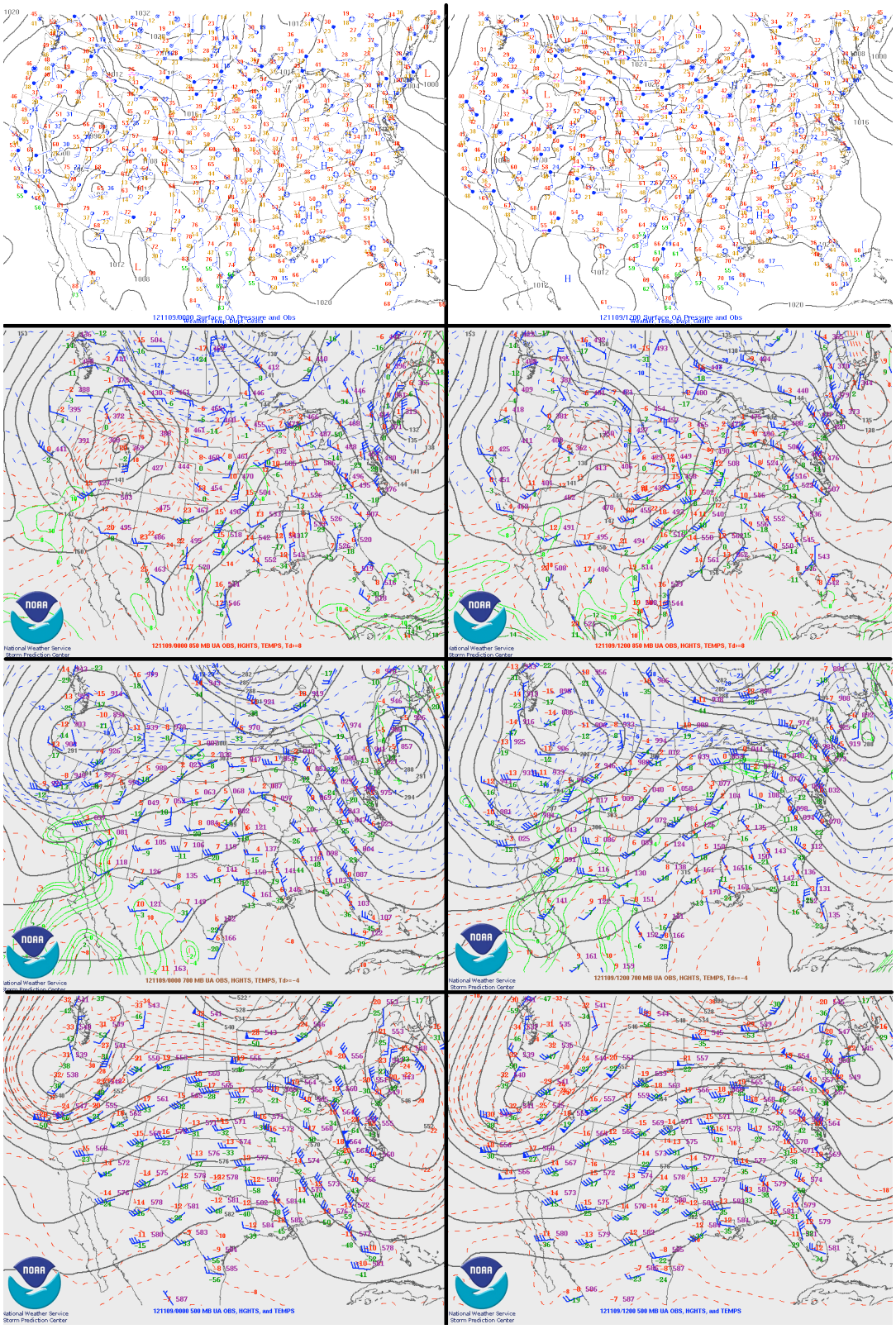

Figure 4.12: Surface, 850-mb, 700-mb, and 500-mb map (top to bottom) from 0000 UTC (left) and 1200 UTC (right) on 9 November 2012. Maps are from the Storm Prediction Center map archive.

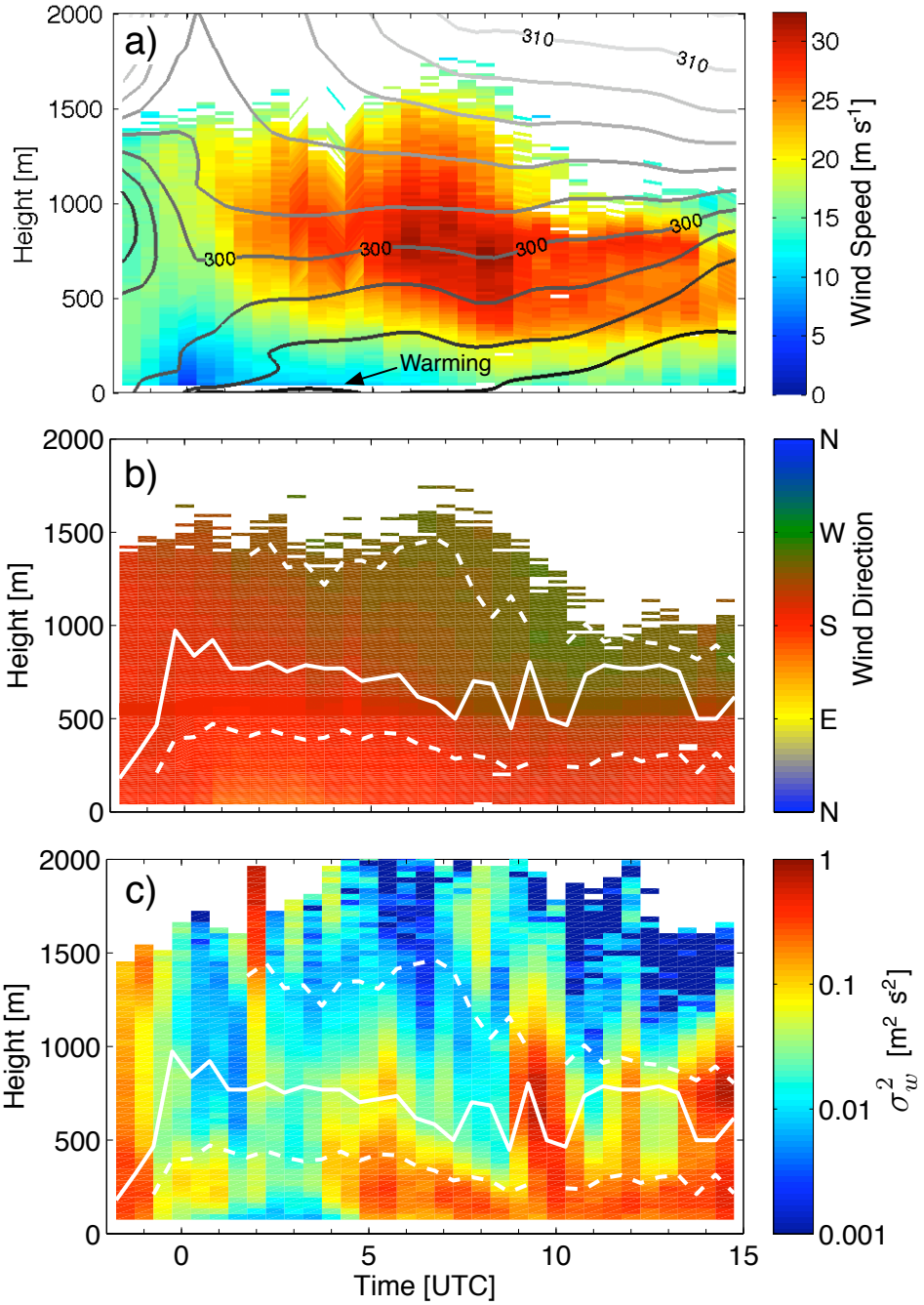

Figure 4.13: Time-height cross sections of wind speed overlaid with isentropes contoured every 2 K where darker colors indicate lower potential temperature (a), wind direction (b), and vertical velocity variance (c) on 9 November 2012. The solid white lines indicate the height of the LLJ, while the dashed lines show where the wind speed is 75% of the wind speed maximum, indicating the relative width of the LLJ. Sunset was at 2325 UTC.

LLJs, it was substantially less than in both 22 and 24 October cases from 0000–0400 UTC. At 0400 UTC, as the LLJ was descending, more substantial turbulent mixing (σ_w^2 greater than 0.1 m^2 s^{-2}) was generated underneath the jet. Between 0400-0500 UTC, this turbulent mixing became connected at the surface as it eroded a weak surface-based inversion that formed, which is shown in Fig. 4.13. After this, the turbulent mixing remained connected to the surface for the remainder of the night. Similarly to many other LLJs, waves passed over the ARM SGP site many times over the night, which show up as large increases in σ_w^2 often on the order of 1 m^{-2} s^{-2}.

4.3 General Differences in Weakly and Strongly Turbulent LLJs

From the above-mentioned case studies, the general synoptic setup and evolution of the LLJ tend to be different between weakly and strongly turbulent LLJs. The LLJs for which strong near-surface turbulent mixing is maintained overnight are generally associated with large mid- and upper-level troughs situated to the west. With these large troughs, the strong synoptic-scale forcing is apparent over the SGP throughout the entire night, from before sunset through sunrise. Conversely, the LLJs that do not generate strong mixing underneath their cores generally form when the synoptic-scale forcing is more subtle. With these LLJs, there is typically no large 500-mb trough over the western United States. Instead, shortwave troughs or closed-lows at the lower levels (below 700 mb) are often situated over eastern Colorado with these weakly turbulent LLJs. These low-level troughs typically

propagate eastward slowly overnight, increasing the pressure gradient and the low-level wind speeds through time.

4.3.1 Different Evolution of LLJ for Weakly and Strongly Turbulent LLJs

4.3.1.1 Evolution of Z_{LLJ} Overnight

In addition to differences in the synoptic setup for the weakly and strongly turbulent LLJs, the LLJs also tended to evolve differently overnight. The evolution of LLJ height Z_{LLJ} overnight, for the two types of jets of jet, are compared in Fig. 4.14. The mean profile with its associated standard deviation, as well as the evolution of Z_{LLJ} on individual nights, are provided. Generally, LLJs with weaker near-surface mixing showed greater variation of Z_{LLJ}, especially early in the night. This is due to the fact that these LLJs tended to originate and form in two different locations. Some weakly-turbulent LLJs formed very close to the surface, often within the lowest 100-m. Others originated much higher, occasionally even above 1 km.

However, values of Z_{LLJ} tended to collapse to a similar height overnight, as shown by the fact that the standard deviation of Z_{LLJ} in Fig. 4.14a became smaller over time. This is likely related to the fact that these weakly turbulent LLJs tend to follow isentropic surfaces, as shown in the case studies in Sect. 4.2.1. As the surface-based nocturnal inversion develops and becomes deeper overnight, as shown in Fig. 3.9, the LLJ would tend to rise following the isentropic surface. Conversely, the LLJs that originated at higher elevations would tend to sink

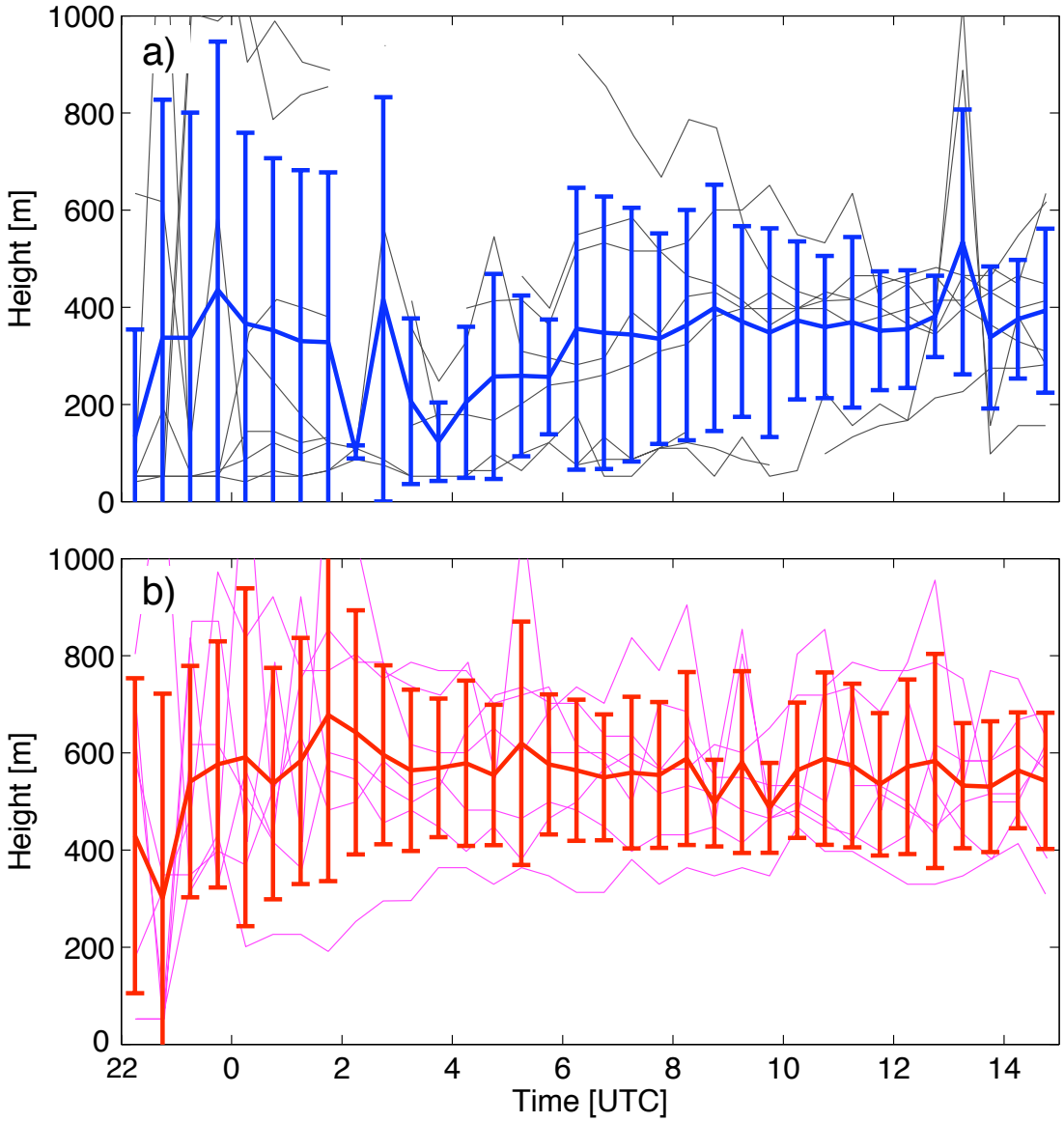

Figure 4.14: General time-evolution of Z_{LLJ} for eight weakly turbulent southerly LLJs (a) and seven strongly turbulent southerly LLJs (b) during LABLE-I. Grey and magenta lines denote the time-evolution on individual nights, while the blue and red lines show the mean height and the standard deviation of the jet height. Individual profiles may have large changes in Z_{LLJ} over short time periods when the LLJ is broad and not well-defined, or if multiple LLJs are present at different heights.

overnight following the isentrope, as the layer of air above 500 m tends to warm from southerly warm air advection. These effects of differential cooling/warming with height overnight, as shown in Fig. 3.10, tend to cause Z_{LLJ} to trend towards to the height where $d\theta/dt$ is zero.

The height of the LLJs that were associated with strong near-surface turbulent mixing evolved very differently overnight, as shown in Fig. 4.14b. The height of the LLJ did not appear to follow isentropic surfaces within the case studies, as the weakly-turbulent LLJs did. This is not surprising, since atmospheric flows only follow isentropic coordinates when turbulent mixing is negligible (Bluestein 1992). Instead, Z_{LLJ} with these strongly turbulent LLJs tended to stay roughly constant over the course of the night. This is reflected in both the mean and individual values of Z_{LLJ} in Fig. 4.14b. Generally, the mean Z_{LLJ} is higher throughout the night for strongly turbulent LLJs.

4.3.1.2 Evolution of V_{LLJ} Overnight

Just as Z_{LLJ} evolved differently for the two categories of LLJs, the relative strength of the jet also showed distinct progressions overnight, as is shown in Fig. 4.15. For weakly turbulent LLJs, V_{LLJ} generally increases throughout the night until shortly before sunrise (1000–1200 UTC). This is apparent for both the mean and individual timeseires of V_{LLJ}. Over the course of the night, variability increases in V_{LLJ} for weakly turbulent LLJs, as shown by standard deviation increasing with time. Early in the night, V_{LLJ} tends to be relatively small ($\approx$10 m s^{-1}) in all of these

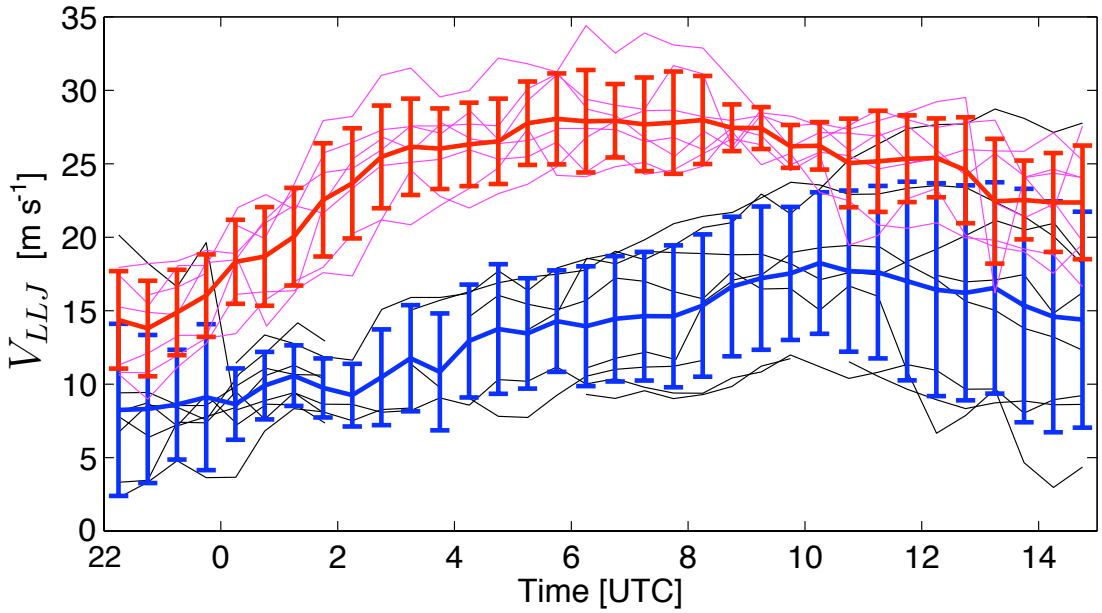

Figure 4.15: General time-evolution of V_{LLJ} from eight weakly-turbulent and seven strongly-turbulent southerly LLJs during LABLE-I. Blue line and errorbars denote the mean and standard deviation of V_{LLJ} for weakly turbulent LLJs, where grey lines are timeseries from individual nights. Red line and errorbars show the mean and standard deviation of V_{LLJ} for strongly turbulent LLJs, where magenta lines are timeseries over individual nights.

LLJs. Over time, V_{LLJ} generally increases by a varying amount depending on the night, with V_{LLJ} remaining relatively constant throughout the night on some occasions. Differences in how V_{LLJ} evolves overnight during weakly turbulent LLJs are likely largely attributed to differences in synoptic scale forcing. Additionally, these differences may be due how stability changes over time, as discussed in Sect. 4.3.2.

While V_{LLJ} generally increases for most of the night with weakly turbulent LLJs, V_{LLJ} typically reaches a maximum value around midnight for strongly turbulent LLJs, after which V_{LLJ} slowly decreases throughout the rest of the night. Additionally, all of these LLJs show a similar pattern, as evidenced by the relatively small standard deviation over the entire night. This timing of the maximum

V_{LLJ} is consistent with what is expected due to the inertial oscillation (Blackadar 1957). The time-evolution of V_{LLJ} for strongly turbulent jets is in better agreement with what is expected theoretically due to the fact that the synoptic-scale forcing remains relatively constant throughout the night. Conversely, shortwave troughs often approach central Oklahoma overnight when weakly turbulent jets are observed, increasing the geostrophic wind V_g.

The value of V_{LLJ} around sunset (≈2300–2400UTC), which is not truly the maximum within the LLJ since a LLJ is often not formed yet, is larger on nights when strongly turbulent LLJs form. Assuming that V_{LLJ} is representative of the mean wind speed in the well-mixed PBL in this time frame, this indicates the strong wind and large near-surface wind shear maintains sufficient turbulence to prevent a strong surface-based temperature inversion from forming. This larger shear contributes to the mechanical generation and maintenance of turbulence around sunset and throughout the night.

4.3.2 Relation to Stability

As shown within the case studies of the LLJs associated with weak turbulent mixing, the LLJs on those nights tend to follow isentropic surfaces. Additionally, V_{LLJ} tends to increase when thermodynamic stability $d\theta/dz$ increases. To further investigate this relationship, values of $\delta\theta/\delta z$ were compared with values of V_{LLJ} for nights with weakly turbulent LLJs where Z_{LLJ} was greater than 200 m. LLJs that were located within the lowest 200 m did not appear to follow this relationship as

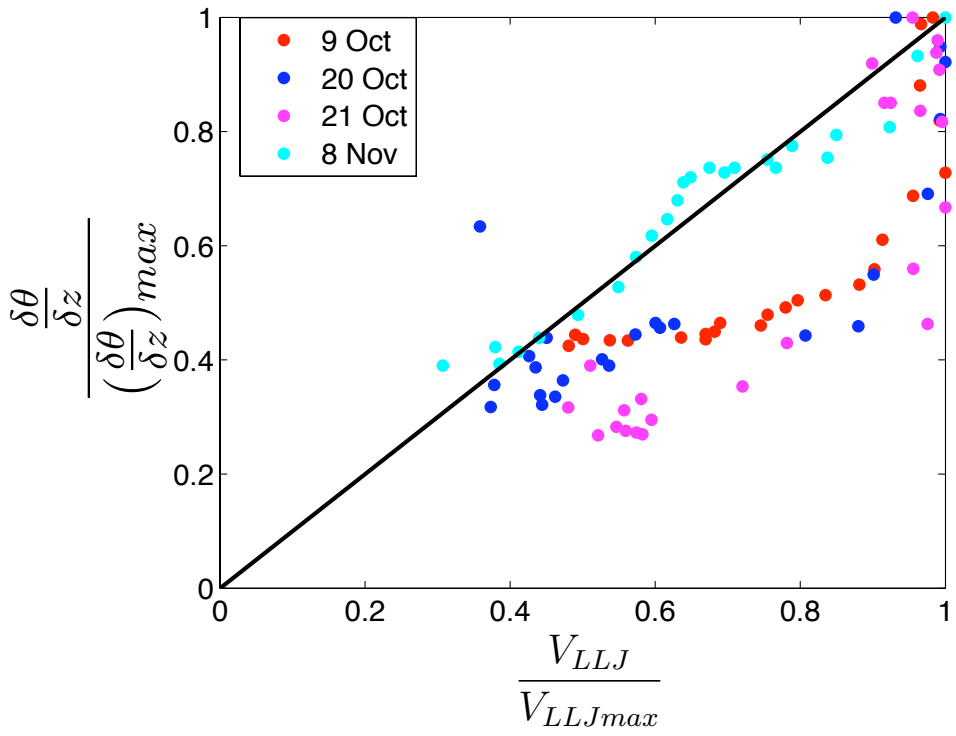

Figure 4.16: Relationship of the relative speed of the LLJ (V_{LLJ}) to the maximum wind speed of the LLJ over the night (V_{LLJmax}) with the static stability ($\delta\theta/\delta z$) over the course of the night. Points on the right relate to when the V_{LLJ} was highest in a given night, and points towards the top are when the stability at Z_{LLJ} is the greatest for that night. Data are shown for nights when near-surface turbulence was weak and Z_{LLJ} was greater than 200 m. Observations from different nights are colored differently, with dates given in legend.

closely, likely due to the fact that diabatic heating for the LLJs was not negligible. Values of $\delta\theta/\delta z$ were calculated from AERI observations, within a layer defined as $\pm$4 K of θ at Z_{LLJ}. Additionally, values of $\delta\theta/\delta z$ and V_{LLJ} were normalized by their respective maximum values on a given night, for comparison across various nights.

Although the relationship is not entirely clear, V_{LLJ} tends to increase with increasing stability as shown in Fig. 4.16. Generally, the maximum V_{LLJ} on a given night corresponded to when stability was the highest. Additionally, V_{LLJ} was often

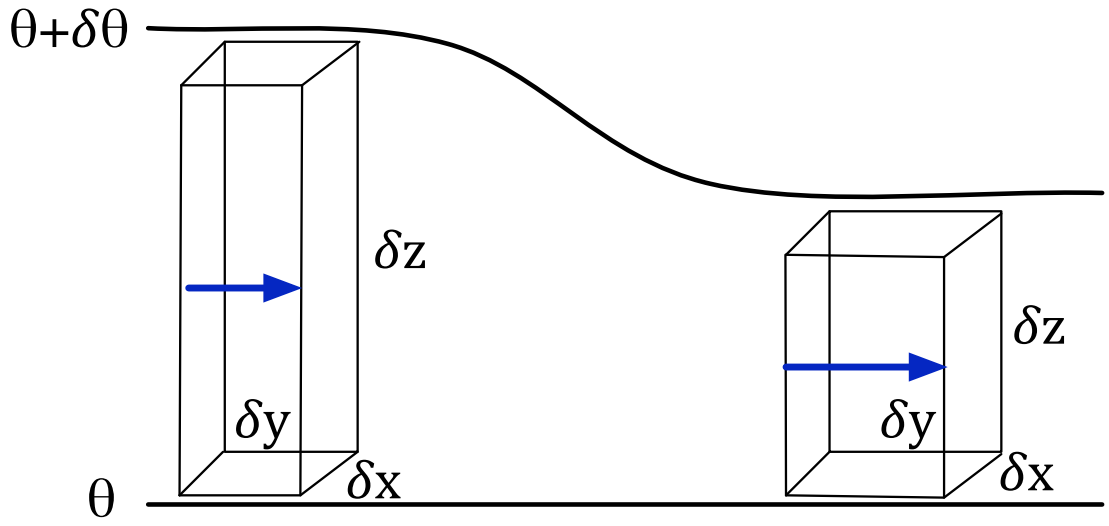

Figure 4.17: Schematic of how a volume of air will changes on an isentropic surface.

much smaller when static stability around it was much weaker. Large scatter in $\delta\theta/\delta z$ is evident for periods when V_{LLJ} is near the maximum.

This strengthening of these weakly turbulent LLJs could be explained by mass conservation on an isentropic surface. Considering a parcel of air that is located between two isentropic surfaces, as in Fig. 4.17, that has a mass M of

$$M = \rho \delta x \delta y \delta z, \tag{4.1}$$

where ρ is the density, δx is its dimension perpendicular to the flow, δy is its dimension along the flow, and δz are its vertical dimension. M will remain constant through time, due to the conservation of mass. The hydrostatic equation can be rearranged and used to substitute for density, where

$$\rho = -\frac{\partial p}{\partial z} g^{-1}. \tag{4.2}$$

As the parcel moves with the flow following the isentropic surface, δz will decrease if stability increases over time. As this happens, δx and δy will need to change to conserve mass. If changes in δx are small, then δy will need to compensate. By carefully looking at Rapid Update Cycle (RUC) analysis for the cases shown in Fig. 4.16, no significant divergence perpendicular to the flow is apparent over northern Oklahoma, indicating that changes in δx are indeed negligible. By neglecting δx, Eq. 4.1 can be used to relate the volume of air at two times by

$$\delta y_1 \delta z_1 \left(\frac{\partial p}{\partial z}\right)_1 = \delta y_2 \delta z_2 \left(\frac{\partial p}{\partial z}\right)_2, \tag{4.3}$$

where the subscripts indicate the values at different times. δy_2 can be related to δy_1 though the strain rate by

$$\delta y_2 = \delta y_1 + \frac{\partial v}{\partial y} \delta y_1 \delta t, \tag{4.4}$$

where $\frac{\partial v}{\partial y}$ is the change in speed along the flow, and δt is the change in time. By combining Eqs. 4.3 and 4.4, the following relationship can be obtained,

$$\frac{\partial v}{\partial y} \delta t = \frac{\delta y_1 \delta z_1 \left(\frac{\partial p}{\partial z}\right)_1}{\delta y_2 \delta z_2 \left(\frac{\partial p}{\partial z}\right)_2} - 1. \tag{4.5}$$

By using the DL and AERI data and using a time-to-space conversion and using finite differencing, $\partial y = \delta y = v \delta t$ for the time between measurement periods. Using finite differencing from the observations, Eq. 4.5 can be rewritten as

$$\frac{\delta v}{v} = \frac{\delta z_1}{\delta z_2} \frac{\left(\frac{\delta p}{\delta z}\right)_1}{\left(\frac{\delta p}{\delta z}\right)_2}, \tag{4.6}$$

where $\delta v = v_2 - v_1$, using the same subscript notation as earlier. While v is the mean average wind speed between the two measurement periods, v will be assumed to be v_1 for simplicity, which should be valid if the wind speed varies slowly. With this assumption Eq. 4.6 can be simplified to

$$v_2 = v_1 \frac{\delta z_1}{\delta z_2} \frac{\left(\frac{\delta p}{\delta z}\right)_1}{\left(\frac{\delta p}{\delta z}\right)_2}. \tag{4.7}$$

Within the lowest 1-km, the ratio of the pressure gradients is approximately unity, further simplifying the relation to

$$v_2 = v_1 \frac{\delta z_1}{\delta z_2}, \tag{4.8}$$

where δ_z is the depth between two isentropic surfaces at different times. This relationship can be used to show why these weakly-turbulent LLJs strengthen when stability increases. If stability increases over time, $\frac{\delta z_1}{\delta z_2}$ is less than one, showing that the velocity increases. Additionally, the ratio of v_2 to v_1 is equal to the ratio of δz_1 to δz_2. Thus theoretically, with the assumptions of no divergence perpendicular to the flow, $\frac{\delta p}{\delta z}$ remaining constant, and the pressure gradient remaining constant, V_{LLJ} should vary proportionally to $\delta\theta/\delta z$ and follow the 1-to-1 line on Fig. 4.16. Scatter is likely due to some divergence perpendicular to the flow or the larger scale forcing changing over time. In addition to LLJs, the above relationship may also be useful for investigating other atmospheric phenomena and

upper-level jets. Although, Eq. 4.7 should only be used for isentropic flows for which the pressure level or height changes substantially over time.

4.3.3 Relation to Inversions

4.3.3.1 Weakly Turbulent LLJs

The mean wind speed overlaid with the temperature profile, for the weakly turbulent LLJs discussed in Sect. 4.2.1, is shown in Fig. 4.18. All the thermodynamic data shown in these plots are from radiosondes, which are capable of resolving elevated inversions and small temperature changes. On 9 October at 0600 UTC, the nose of the LLJ was relatively broad, with the wind speed being $\approx$16–17 m s^{-1} over a layer extending from 250–700 m, as shown in Fig. 4.18a. This region was bounded by two inversions on the top and on the bottom. Between 0600–1200 UTC, the layer above 400 m but below the upper inversion warmed. During this time, V_{LLJ} increased and the shear associated with the LLJ also increased, as a pronounced well-defined LLJ nose formed. This coincided with the increase in stability discussed within Sect. 4.2.1.1. By 1200 UTC on 9 October, the LLJ nose was located within, but near the top of, a deep surface-based inversion, similarly to what was found by Andreas et al. (2000).

Profiles at both 0600 UTC and 1200 UTC over 21 October are shown within Fig. 4.18c, d. At 0600 UTC, two LLJ maxima were present at 400 m and 1500 m, although the DL was only able to capture the lower one due to reduced SNR about 1300 m. Between the two maxima, there was a relatively broad area of moderately

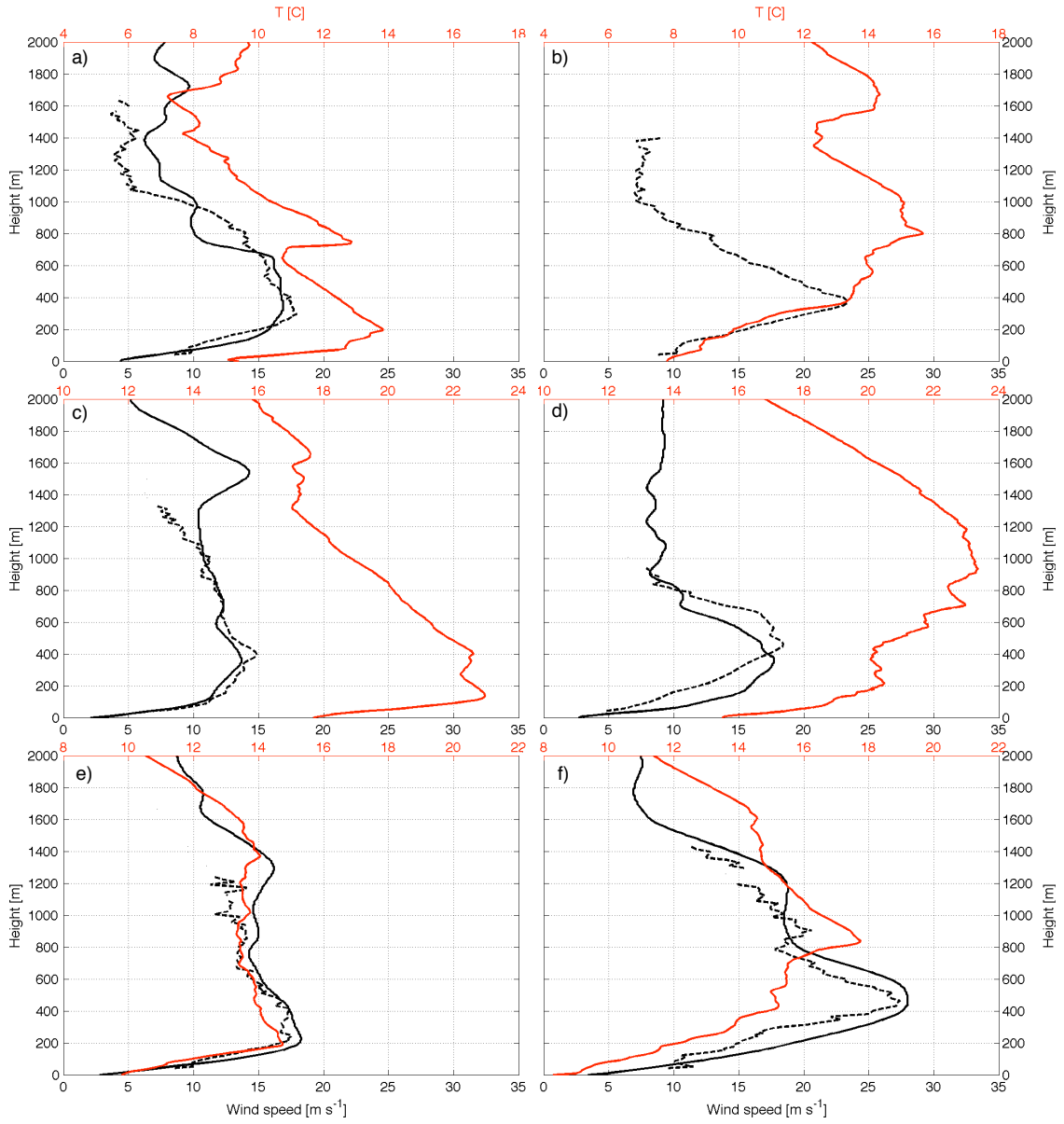

Figure 4.18: Profiles of temperature and wind speed during time periods when LLJs with weak near-surface turbulence. Red lines show the temperature measured by the radiosonde, and black shows the wind speed from the OU DL (dashed) and radiosonde (solid). Profiles are for the cases discussed in Sect. 4.2.1: 9 October (a, b), 21 October (c, d), and 8 November (e, f). Left column is from profiles at approximately 0600 UTC, right is at 1200 UTC. Radiosonde and DL observations may be up to 15 min apart.

strong winds greater than 10 m s^{-1}. The maxima at 400 m was located at the top of an inversion, although the inversion was not surface-based. The second maxima was located within an isothermal layer between two relatively dry-adiabatic regions. Additionally, a kink in the momentum profile is at the top of the surface-based inversion. By 1200 UTC, the layer above 550 m warmed resulting in a broad elevated inversion between 400–900 m, as shown in Fig. 4.18 d. Between 0600–1200 UTC, as this layer warmed, V_{LLJ} increased and the shear associated with the jet also increased. The LLJ at 1200 UTC was located underneath an elevated inversion.

At 0600 UTC on 8 November, a LLJ nose was collocated with the top of a strong surface-based inversion at 200 m (see Fig. 4.18 e), similarly to what was found in previous studies (Baas et al. 2009). Again, a secondary wind speed maxima is evident at 1300 m. By 1200 UTC, Z_{LLJ} was about twice as high as it was at 0600 Z, as Z_{LLJ} increased as the surface-based inversion grew deeper overnight. Additionally, the top of the LLJ was collocated with an elevated inversion at ≈800 m. Throughout all six profiles, no clear relation between Z_{LLJ} and the inversion height was consistently observed for weakly turbulent LLJs. Although, the LLJs were generally located within, just below, or between inversions in each case.

4.3.3.2 Strongly Turbulent LLJs

Similar comparisons between the temperature and wind speed profiles are made for strongly turbulent LLJs within Fig. 4.19. None of the LLJs shown here were associated with surface-based inversions, due to the continuous overnight mixing. On 22 October, Z_{LLJ} coincided with the location of an elevated inversion at 650 m, as shown in Fig. 4.19a, b. Between 0600–1200 UTC, the layer between the surface and the inversion cooled, as air cooled at the surface was mixed throughout the layer. Above Z_{LLJ}, the air warmed since turbulence within that layer was weak, as was shown in Fig. 4.8b. This lead to an intensification of the inversion at 650 m over the night. The shear at the top of the LLJ increased overnight with this increase in static stability.

On 24 October at 0600 UTC, the LLJ was again collocated with an elevated inversion (Fig. 4.19c), albeit a weaker one where T increased by 0.75 K over 150 m. By 1200 UTC, the stability with the elevated inversion strengthened, as the entire layer below it cooled and the layer above it warmed slightly, as shown in Fig. 4.19d. Again at 1200 UTC, Z_{LLJ} was located at the elevated inversion. The evolution of the LLJ, in relation to the temperature profiles, was a little different on 9 November (Fig. 4.19e, f). In both profiles Z_{LLJ} was located at an elevated inversion, but the shape of the LLJ changed over time. Shear in the lowest 200 m increased considerably as static stability also increased over time within the same layer. This is likely due to warm air advection, which becomes larger with height, being greater than the vertical redistribution of heat from turbulent mixing,

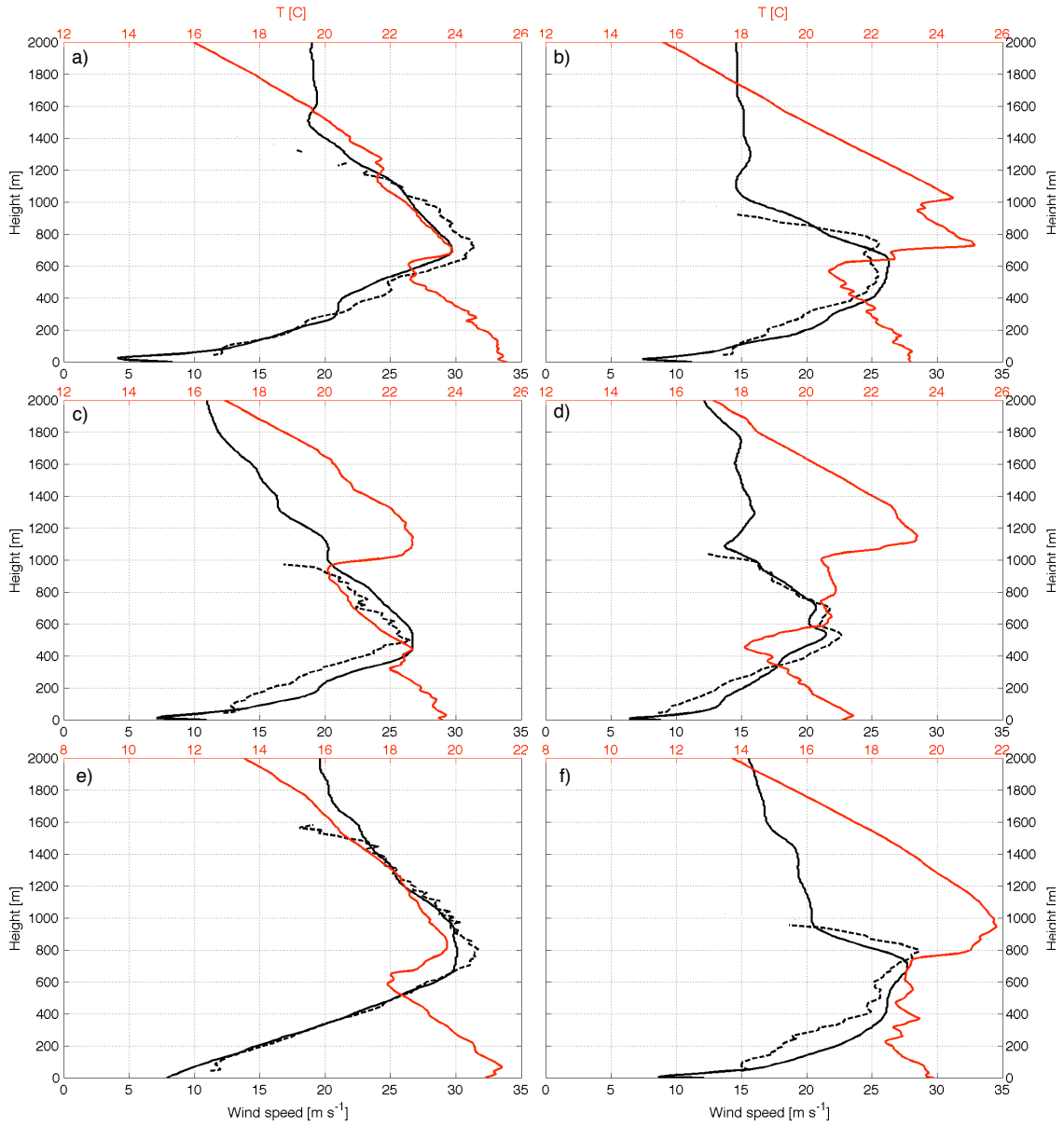

Figure 4.19: Profiles of temperature and wind speed during time periods when LLJs with strong near-surface turbulence. Red lines show the temperature measured by the radiosonde, and black shows the wind speed from the OU DL (dashed) and radiosonde (solid). Profiles are for the cases discussed in Sect. 4.2.2: 22 October (a, b), 24 October (c, d), and 9 November (e, f). Left column is from profiles at approximately 0600 UTC, right is at 1200 UTC. Radiosonde and DL observations may be up to 15 min apart.

Overall, Z_{LLJ} was collocated with an elevated inversion for strongly turbulent LLJs. This appears to be due to the fact that the air below Z_{LLJ} is well-mixed. Thus, air cooled near the surface is transported upward, and warmer air from above is mixed downward. However, at and above Z_{LLJ}, mixing is very weak and the layer generally warms over time due to the southerly warm air advection, intensifying the strength of the elevated inversion over time.

4.4 Results

During LABLE-I, many LLJs were observed at the SGP ARM site. The LLJs are grouped into two broad categories, strongly or weakly turbulent, based on near-surface values of σ_w. Three case studies are shown for each category of LLJ, wherein the synoptic setup and evolution of the LLJs are presented and discussed. The weakly turbulent LLJs were generally associated with weaker synoptic-scale forcing, and the forcing is usually delayed until after a strong surface-based inversion is formed. With these LLJs, shortwave troughs at 850-mb are often apparent a few hundred kilometers to the west. Conversely, the strongly turbulent LLJs are typically associated with strong large-scale 500-mb troughs situated over the west coast. Due to the size of the troughs and their slower propagation compared to shortwaves, turbulent LLJs often form on several consecutive nights before the system passes over the area. Additionally, the strong forcing and winds are present over the area before sunset, so the strongly generated mechanical mixing keeps a strong surface-based inversion from forming overnight.

Not only were the synoptic setups different, but the two categories of LLJs evolved differently overnight and were related to different thermodynamic features. The height of the LLJ generally stayed relatively constant throughout the night for turbulent LLJs, and the wind speed reached a maximum around midnight. Weakly turbulent LLJs tended to follow isentropic surfaces by rising overnight if they were initially located near the surface, or sink with time if the LLJ was located over 500 m. These LLJs generally slowly strengthened over the entire night, reaching a maximum in magnitude shortly before sunrise. Additionally, some weakly turbulent LLJs tended to strengthen overnight as the stability increased. This could be at least partially attributed to the conservation of mass along isentropic surfaces.

While LLJs tended to correspond with inversions in some way, no universal correlation was found. Weakly turbulent LLJs tended to be located within, near the top of, or just above surface-based temperature inversions. However, there was no consistent tendency with the inversion. Additionally, one of these LLJs was relatively broad and located distinctly between a surface-based inversion and elevated inversion. Strongly turbulent LLJs tended to be located at the bottom of an elevated inversion. On nights when these LLJs formed, no surface-based inversion was evident in the radiosonde profiles.

Chapter 5

Summary and Conclusions

Results from two separate field campaigns are presented herein. The first field campaign, LABLE-I, was conducted at the ARM SGP site in rural north central Oklahoma. During LABLE-I, OU brought and set up several instruments at the ARM SGP site to supplement the existing infrastructure and suite of measurements that is operated by the DOE. While there were several objectives of LABLE-I, the focus here is on the nocturnal SBL and their associated LLJs. Observations from several DLs, an AERI, sonic anemometer measurements on a 60-m tower, and radiosonde measurements were combined to reconstruct the state of the lower atmosphere as it evolved in height and over time.

The second field campaign, LATTE, took place in the late winter and early spring of 2014 at the BAO site in Erie, CO, which is located about 25 km east of the foothills of the Rocky Mountains. One of the primary objectives of LATTE was to validate and improve DL measurements of turbulent quantities, by comparing measurements with those from sonic anemometers installed at six levels on a 300-m tower. During an observational period from 26–28 March, two DLs were placed within a few meters of the base of the tower for a direct comparison of vertical velocity variances with those from sonic anemometer observations. One of

the DLs simply stared vertically continuously measuring w during this time. The second lidar continuously performs DBS scans, thus it only measured w every 4 s.

Observations taken during these two field experiments are used to answer the three overarching questions that were asked at the end of Ch. 1. Those questions are revisited now and the new findings obtained within this study are summarized for each question.

1. How accurate are DL-derived estimates of vertical velocity variance, and can these estimates be improved?

During LATTE, DL-derived estimates of σ_w^2 generally agreed well with those measured by the sonic anemometers under a wide variety of conditions. The high sampling frequency and half-hourly averaging times kept the random errors and sampling errors from the DL σ_w^2 estimates to be small and negligible. Thus, values of σ_w^2 computed from the raw DL timeseries (when SNR was high) are often very similar to those from the sonic anemometer, and values of σ_w^2 are in even closer agreement after applying the autocovariance correction for noise discussed by Lenschow et al. (2000). Values of raw DL σ_w^2 are generally underestimated when the SNR is low and σ_w^2 high, due to inabilities to accurately capture small-scales of turbulence resulting from time and volume averaging effects. Under stable conditions when the inertial subrange is small, applying the autocovariance correction generally improved estimates of σ_w^2 from the OU DL. While the corrected-DL estimates of σ_w^2 generally underestimated the sonic variances in these conditions, the uncorrected-DL values of σ_w^2 often greatly overestimated those from the sonic

data. During these conditions, even a small amount of noise lead to large overestimates of the raw σ_w^2.

Here, the autocovariance correction is refined by defining the ideal number of lags to use within the fitting based, whereas previously the amount of lagtime varied based on the authors' discretion (e.g., Behrendt et al. 2014; McNicholas and Turner 2014). Not only did this correction accurately remove noise when it was present, but it also corrected for underestimates of the DL-derived σ_w^2. The accuracy of the corrected estimates of σ_w^2 are shown to be very sensitive to the number of lags used in the fitting of the structure function to the autocovariances. By using a long lag time in the fitting (100 s or longer), estimates of σ_w^2 are often only 50–70% of the true atmospheric variance. This is due to a combination of two main effects: (i) some of the autocovariance values being out of the inertial subrange and (ii) turbulence evolving over time, invalidating the frozen turbulence hypothesis.

2. Can vertical velocity measurements from the DL be used to confirm or improve the classification of the nocturnal SBL as either weakly stable or very stable? How do the properties (i.e., turbulence, thermodynamic, velocity) within these subtypes of SBLs vary in time and height?

Using observations taken during LABLE-I, the nocturnal SBL typically fell into three distinct categories based on the near-surface turbulence level: weakly, moderately, and strongly turbulent. These categories are determined from how the values of σ_w in the lowest 100-m relate to the slope of $d\sigma_w/dV$, related to how V

compares to V_T. Weakly turbulent conditions occur when σ_w is less than 0.2 m s^{-1}, corresponding to time periods when $d\sigma_w/dV$ is near zero and the V was less than V_T. Moderately turbulent conditions typically are observed when σ_w is greater than 0.2 m s^{-1} but less than 0.4 m s^{-1}. In this range, the vertical velocity variance increases rapidly as the wind speed increases (i.e., $d\sigma_w/dV$ is the largest). Strongly turbulent conditions exist when σ_w is greater than 0.4 m s^{-1}. Cases where the low-level turbulence was either moderate or strong generally exhibited features of the wSBL, while weakly-turbulent conditions favored vSBL development. Additionally, the threshold wind speed hypothesis proposed by Sun et al. (2012) is confirmed and is expanded to heights up to 300 m using DL measurements, whereas previously values of V_T were only determined from sonic anemometer measurements on a tower up to 55-m.

Generalized vertical profiles of σ_w for each of the three turbulent regimes were different. Within the strongly turbulent SBL, turbulence is generated near the surface and transported upwards. When mixing is weak, turbulence is generated either aloft (near a wind maximum) or near the surface depending on if the SBL exhibited features of either an 'upside-down' or a thin traditional boundary layer. When mixing is of moderate intensity, the turbulence profile generally exhibited features of both the strongly and weakly turbulent regimes, where turbulence was

generated both at the surface and under the wind speed maxima. Normalized velocity profiles of the three regimes generally were very similar to each other, although the stronger mixing generally coincided with larger maximum wind speeds of an existing LLJ.

Due to the sustained turbulent mixing, in the moderately and strongly turbulent SBL, no strong surface-based nocturnal inversion formed throughout the night. However, throughout the night stability within the lowest 1-km tended to increase due to the cooling at the low levels, which was mixed through a deeper layer, and warming aloft from southerly warm air advection. In the lowest few hundred meters of the NBL, the temperature profile tended to remain relatively isothermal throughout the night. When turbulent mixing was weak and a vSBL developed, a strong surface based inversion formed around sunset, above which the profile remained relatively dry adiabatic in the residual layer. Throughout the night, the depth of the inversion continued to slowly grow. The strength of the inversion, in terms of highest stability at the surface, occurred around midnight.

3. How do LLJs themselves evolve under differing turbulence regimes? Do the LLJs have different features, or are driven by different mechanisms, under these different regimes?

Southerly nocturnal LLJs were frequently observed at the SGP ARM site during LABLE-I. These LLJs tended to behave differently depending on if they were associated with either the aforementioned wSBL (moderately or strongly turbulent)

or vSBL (weakly turbulent). Additionally, the synoptic conditions were also different for the development of LLJs within each turbulent regime. Often, LLJs that were associated with a wSBL formed on several consecutive nights when a large, deep 500-mb trough was located over the western United States for the duration of the night. On nights where a vSBL developed with a LLJ, the synoptic scale forcing was generally more subtle, often with just an 850-mb trough that was located several hundred kilometers to the west. Additionally, the pressure gradient often became tighter overnight.

LLJs that developed under each SBL type also had distinct characteristics and evolution cycles. The strongly turbulent LLJs tended to remain relatively constant in height overnight and were located at ≈600 m. The weakly turbulent LLJs tended to either rise or sink overnight, depending on if the LLJ formed near the surface or at a much higher elevation (over 500 m). However, the height of the weakly turbulent LLJs tended to become more similar overnight, approaching the height where the $d\theta/dt$ tends to be zero. The weakly turbulent LLJs also tended to increase in magnitude overnight, reaching a maximum wind speed shortly after sunrise. This is likely due to the general increase in the pressure gradient and larger-scale forcing overnight. Strongly turbulent LLJs tended to increase in strength rapidly after sunset and reached a maximum wind speed at around midnight, after which the wind speed tended to slowly decrease. This is in agreement with what is expected from an inertial oscillation (Blackadar 1957).

Outlook While several questions have been answered through observations during LABLE-I, additional questions were also raisied which may be addressed in followup studies. The relationship between mean wind speed and vertical velocity variance was observed to be different for southerly and northerly winds, as V_T for northerly winds appeared to be lower than V_T for southerly winds. This difference could be possibly due to temperature advection changing with height, wherein warm air advection with southerly winds increasing with height tends to increase stability with time and cold air advection with northerly winds increasing with height tends to decrease static stability. Additionally, the net flux at the surface could vary depending on the conditions. An upward soil heat flux may be large under northerly winds after a cold front passage where the ground is still relatively warm. These differences will need to be investigated more closely to understand the physics behind the difference in observed threshold wind speed. Waves of unknown origin were also frequently observed, which can impact the structure of the SBL and other weather conditions, and should be studied thoroughly.

Within this study, it is shown that the structure and evolution of the nocturnal SBL and LLJs is very different depending on the intensity of mixing. For the first time, high temporal- and vertical-resolution measurements of mean flow, temperature, and turbulent quantities have been measured concurrently within the lowest 1-km of the atmosphere. Within previous NBL and LLJ studies that use DLs, continuous thermodynamic measurements above the near surface are not available. However, observations from the AERI have yielded useful insight into

how the thermodynamics within entire NBL evolve overnight. These observations have shown that the nocturnal SBL and associated LLJ show distinct characteristics depending on the amount of near-surface turbulent mixing. LLJs associated with weakly and strongly SBLs evolve dissimilarly, which has not been shown previously. Thus, in the future, LLJs should be categorized differentially within climatological studies and it may be necessary to develop new theories and parameterizations for numerical models that better capture the differences between the two types of LLJs.

References

Acevedo, O. C. and D. R. Fitzjarrald, 2001: The early evening surface-layer transition: Temporal and spatial variability. *J. Atmos. Sci.*, **58**, 2650–2667.

Alvarez, R. J., II, C. J. Senff, A. O. Langford, A. M. Weickmann, D. C. Law, J. L. Machol, D. A. Merritt, R. D. Marchbanks, S. P. Sandberg, W. A. Brewer, R. M. Hardesty, and R. M. Banta, 2011: Development and application of a compact, tunable, solid-state airborne Ozone lidar system for boundary layer profiling. *J. Atmos. Ocean. Tech.*, **28**, 1258–1272.

Andreas, E. L., K. J. Claffey, and A. P. Makshtas, 2000: Low-level atmospheric jets and inversions over the western Weddell Sea. *Bound-Lay. Meteorol.*, **97**, 459–486.

Arritt, R. W., T. D. Rink, M. Segal, D. P. Todey, C. A. Clark, M. J. Mitchell, and K. Labas, 1997: The Great Plains low-level jet during the warm season of 1993. *Mon. Weather Rev.*, **125**, 2176–2192.

Augustine, J. A. and F. Caracena, 1994: Lower-tropospheric precursors to nocturnal MCS development over the central United States. *Wea. Forecasting*, **9**, 116–135.

Baas, P., F. C. Bosveld, H. Klein Baltink, and A. A. M. Holtslag, 2009: A climatology of noturnal low-level jets at Cabauw. *J. Appl. Meteorol. Clim.*, **48**, 1627–1642.

Banta, R. M., L. Mahrt, D. Vickers, J. Sun, B. B. Balsley, Y. L. Pichugina, and E. J. Williams, 2007: The very stable boundary layer on nights with weak low-level jets. *J. Atmos. Sci.*, **64**, 3068–3090.

Banta, R. M., R. K. Newsom, J. K. Lundquist, Y. L. Pichugina, R. L. Coulter, and L. Mahrt, 2002: Nocturnal low-level jets characteristics of Kansas during CASES-99. *Bound.-Lay. Meteorol.*, **105**, 221–252.

Banta, R. M., Y. L. Pichugina, and W. A. Brewer, 2006: Turbulent velocity-variance profiles in the stable boundary layer generated by a nocturnal low-level jet. *J. Atmos. Sci.*, **63**, 2700–2719.

Banta, R. M., P. B. Shepson, J. W. Bottenheim, K. G. Anlauf, H. A. Wiebe, A. Gallant, T. Biesenthal, L. D. Oliver, C. Zhu, I. G. McKendry, and D. G. Steyn, 1997: Nocturnal cleansing flows in a tributary valley. *Atmos. Environ.*, **31**, 2147–2162.

Barkwith, A. and C. Collier, 2011: Lidar observations of flow variability over complex terrain. *Meteorol. Appl.*, **18**, 372–382.

Barlow, J. F., T. M. Dunbar, E. G. Nemitz, C. R. Wood, M. W. Gallagher, F. Davies, E. O'Connor, and R. M. Harrison, 2011: Boundary layer dynamics over London, UK, as observed using Doppler lidar during REPARTEE-II. *Atmos. Chem. Phys.*, **11**, 2111–2125.

Behrendt, A., V. Wulfmeyer, E. Hammann, S. K. Muppa, and S. Pal, 2014: Profiles of second- to third-order moments of turbulent temperature fluctuations in the convective boundary layer: first measurements with Rotational Raman Lidar. *Atmos. Chem. Phys. Disc.*, **14**, 29019–29055.

Blackadar, A. K., 1957: Boundary layer wind maxima and their significance for the growth of nocturnal inversions. *Bull. Amer. Meteor. Soc.*, **38**, 282–290.

Bluestein, H. B., 1992: *Synoptic-Dynamic Meteorology in Midlatitudes*, volume I. Oxford University Press.

Bonin, T., P. B. Chilson, B. Zielke, and E. Fedorovich, 2013: Observations of early evening boundary layer transitions using a small unmanned aerial system. *Bound-Lay. Meteorol.*, **146**, 119–132.

Bonner, W. D., 1968: Climatology of the low level jet. *Mon. Wea. Rev.*, **96**, 833–850.

Brinkmann, W. A. R., 1974: Strong downslope winds at Boulder, Colorado. *Mon. Wea. Rev.*, **102**, 592–602.

Browning, K. A. and R. Wexler, 1968: The determination of kinematic properties of a wind field using Doppler radar. *J. Appl. Meteorol.*, **7**, 105–113.

Cariou, J.-P. and M. Boquet, 2010: LEOSPHERE Pulsed Lidar Principles. Contribution to UpWind WP6 on Remote Sensing Devices.
URL `http://www.upwind.eu/Publications/~/media/UpWind/Documents/Publications/6%20-%20Remote%20Sensing/D611.ashx`

Carrico, C. M., M. J. Rood, and J. A. Ogren, 1998: Aerosol light scattering properties at Cape Grim, Tasmania, during the First Aerosol Characterization Experiment (ACE 1). *J. Geophys. Res.*, **103**, 16565–16574.

Chanin, M. L., A. Garnier, A. Hauchecome, and J. Porteneuve, 1989: A Doppler lidar for measuring winds in the middle atmosphere. *Geophys. Res. Lett.*, **16**, 1273–1276.

Charland, A. M. and C. B. Clements, 2013: Kinematic structure of a wildland fire plume observed by Doppler lidar. *J. Geophys. Res.-Atmos.*, **118**, 3200–3212.

Clarke, R. H., R. K. Smith, and D. G. Reid, 1981: The Morning Glory of the Gulf of Carpentaria: an atmospheric undular bore. *Mon. Wea. Rev.*, **109**, 1726–1750.

Clough, S. A., M. J. Iacono, and J.-L. Moncet, 1992: Line-by-line calculations of atmospheric fluxes and cooling rates: Application to water vapor. *J. Geophys. Res.-Atmos.*, **97**, 15761–15785.

Cook, D. R., 2011: *Eddy correlation flux measurement system handbook*. Department of Energy, DOE/SC-ARM/TR-052.

Corsmeier, U., N. Kaithoff, O. Kolle, M. Kotzian, and F. Fiedler, 1997: Ozone concentration jump in the stable nocturnal boundary layer during a LLJ-event. *Atmos. Environ.*, **31**, 1977–1989.

Coulter, R. L., 1990: A case study of turbulence in the stable nocturnal boundary layer. *Boundary-Layer Meteorol.*, **52**, 75–91.

Cuxart, J. and M. A. Jiménez, 2007: Mixing processes in a nocturnal low-level jet: An LES study. *J. Atmos. Sci.*, **64**, 1666–1679.

Davies, F., C. G. Collier, G. N. Pearson, and K. E. Bozier, 2004: Doppler lidar measurements of turbulent structure function over an urban area. *J. Atmos. Ocean. Tech.*, **21**, 753–761.

Davis, J. C., C. G. Collier, F. Davies, and K. E. Bozier, 2008: Spatial variations of sensible heat flux over and urban area measured using Doppler lidar. *Meteorol. Appl.*, **15**, 367–380.

Dunbar, T. M., J. F. Barlow, and S. E. Belcher, 2014: An optimal inverse method using Doppler lidar measurements to estimate the surface sensible heat flux. *Boundary-Layer Meteorol.*, **150**, 49–67.

Edwards, J. M., 2009: Radiative process in the stable boundary layer: Part i. radiative aspects. *Boundary-Layer Meteorol.*, **131**, 105–126.

Einaudi, F. and J. J. Finnigan, 1993: Wave-turbulence dynamics in the stabily stratified boundary layer. *J. Atmos. Sci.*, **50**, 1841–1864.

Finnigan, J. J., E. Einaudi, and D. Fua, 1984: The interaction between an internal gravity wave and turbulence in the stably-stratified nocturnal boundary layer. *J. Atmos. Sci.*, **41**, 2409–2436.

Frehlich, R. and L. Cornman, 2002: Estimating spatial velocity statistics with coherent Doppler lidar. *J. Atmos. Ocean. Techn.*, **19**, 355–366.

Fuertes, F. C., G. V. Iungo, and F. Porté-Agel, 2014: 3d turbulence measurements using three synchronous wind lidars: Validation against sonic anemometry. *J. Atmos. Ocean. Tech.*, **31**, 1549–1556.

Gal-Chen, T., M. Xu, and W. L. Eberhard, 1992: Estimations of atmospheric boundary layer fluxes and other turbulence parameters from Doppler lidar data. *J. Geophys. Res.*, **97**, 18409–18423.

Garratt, J., 1992: *The Atmospheric Boundary Layer*. Cambridge University Press, 316 pp, 1 edition.

Grund, C. J., R. M. Banta, J. L. George, J. N. Howell, M. J. Post, R. A. Richter, and A. M. Weickmann, 2001: High-resolution Doppler lidar for boundary layer and cloud research. *J. Atmos. Ocean. Tech.*, **18**, 376–393.

Ha, K.-J. and L. Mahrt, 2003: Radiative and turbulent fluxes in the nocturnal boundary layer. *Tellus*, **55**, 317–327.

Havijärvi, H., 2006: Radiative and turbulent heating rates in the clear-air boundary layer. *Q. J. R. Meteorol. Soc.*, **132**, 147–161.

Higgins, C. W., M. Froidevaux, V. Simeonov, N. Vercauteren, C. Barry, and M. B. Parlange, 2013: The effect of scale on the applicability of Taylor's frozen turbulent hypothesis in the atmospheric boundray layer. *Boundary-Layer Meteorol.*, **143**, 379–391.

Higgins, R. W., Y. Yao, E. S. Yarosh, J. E. Janowiak, and K. C. Mo, 1997: Influence of the Great Plains low-level jet on summertime precipitation and moisture transport over the Central United States. *J. Climate*, **10**, 481–507.

Hogan, R. J., A. L. M. Grant, A. J. Illingworth, G. N. Pearson, and E. J. O'Connor, 2009: Vertical velocity variance and skewness in clear and cloud-topped boundary layers as revealed by Doppler lidar. *Q. J. R. Meteorol. Soc.*, **135**, 635–643.

Hollinger, D. Y. and A. D. Richardson, 2005: Uncertainty in eddy covariance measurements and its application to physiological models. *Tree Physiol*, **25**, 873–885.

Holton, J. R., 1967: The diurnal boundary layer wind oscillation above sloping terrain. *Tellus*, **19**, 199–205.

Hopfinger, E. J., 1987: Turbulence in stratified fluids: a review. *J. Geophys. Res.*, **92**, 5287–5303.

Hu, X., P. M. Klein, M. Xue, J. K. Lundquist, F. Zhang, and Y. Qi, 2013a: Impact of low-level jets on the nocturnal urban heat island intensity in Oklahoma City. *J. Appl. Meteorol. Clim.*, **52**, 1779–1802.

Hu, X., P. M. Klein, M. Xue, F. Zhang, D. C. Doughty, R. Forkel, E. Joseph, and J. D. Fuentes, 2013b: Impact of vertical mixing induced by low-level jets on boundary layer ozone concentration. *Atmos. Environ.*, **70**, 123–130.

Iwai, H., Y. Murayama, S. Ishii, K. Mizutani, Y. Ohno, and T. Hashiguchi, 2011: Strong updraft at a sea-breeze front and associated vertical transport of near-surface dense aerosol observed by Doppler lidar and ceilometer. *Bound-Lay. Meteorol.*, **141**, 117–142.

Kaimal, J. C. and J. J. Finnigan, 1994: *Atmospheric Boundary Layer Flows: Their structure and measurement*. Oxford University Press, 304 pp.

Kaimal, J. C. and J. E. Gaynor, 1983: The Boulder Atmospheric Observatory. *J. Clim. Appl. Meteorol.*, **22**, 863–880.

Kallistratova, M. A., R. D. Kouznetsov, V. F. Kramar, and D. D. Kuznetsov, 2013: Profiles of wind speed variances within nocturnal low-level jets observed with a sodar. *J. Atmos. Ocean. Tech.*, **30**, 1970–1977.

Kaplan, M. L., Y. Lin, J. J. Charney, K. D. Pfeiffer, D. B. Ensley, D. S. DeCroix, and R. P. Weglarz, 2000: A terminal area PBL prediction system at Dallas–Fort Worth and its application in simulating diurnal PBL jets. *B. Am. Meteorol. Soc.*, **81**, 2179–2204.

Karipot, A., M. Y. Leclerc, G. Zhang, T. Martin, G. Starr, D. Hollinger, J. H. McCaughey, and G. R. Hendrey, 2006: Nocturnal CO_2 exchange over a tall forest canopy associated with intermittent low-level jet activity. *Theor. Appl. Climatol.*, **85**, 243–248.

Käsler, Y., S. Rahm, R. Simmet, and M. K uhn, 2010: Wake measurements of a multi-MW wind turbine with coherent long-range pulsed Doppler wind lidar. *J. Atmos. Ocean. Tech.*, **27**, 1529–1532.

Kasten, F., 1969: Visibility forecast in the phase of pre-condensation. *Tellus*, **5**, 631–635.

Kelley, N., M. Shirazi, D. Jagger, S. Wilde, J. Adams, M. Buhl, P. Sullivan, and E. Patton, 2006: Lamar low-level jet project interim report. Technical Report NREL/CP-500-40176, National Renewable Energy Laboratory: Golden, CO.

Klein, P., T. A. Bonin, J. F. Newman, D. D. Turner, P. B. Chilson, C. E. Wainwright, W. G. Blumberg, S. Mishra, M. Carney, E. P. Jacobsen, S. Wharton, and R. K. Newsom, 2015: LABLE: a multi-institutional, student-led, atmospheric boundary-layer experiment. *B. Am. Meteorol. Soc.*, in press.

Klein, P. M., X. Hu, and M. Xue, 2014: Impacts of mixing processes in nocturnal atmospheric boundary layer on urban ozone concentrations. *Bound.-Lay. Meteorol.*, **150**, 107–130.

Knuteson, R. O., H. E. Revercomb, F. A. Best, N. C. Ciganovich, R. G. Dedecker, T. P. Dirkx, S. C. Ellington, W. F. Feltz, R. K. Garcia, H. B. Howell, W. L. Smith, J. F. Short, and D. C. Tobin, 2004a: Atmospheric emitted radiance interferometer. part 1: Instrument design. *J. Atmos. Ocean. Tech.*, **21**, 1763–1776.

—, 2004b: Atmospheric emitted radiance interferometer. part ii: Instrument performance. *J. Atmos. Ocean. Tech.*, **21**, 1777–1789.

Koch, S. E., P. B. Dorian, R. Ferrare, S. H. Melfi, W. C. Skillman, and D. Whiteman, 1991: Structure of an internal bore and dissipating gravity current as revealed by Raman lidar. *Mon. Wea. Rev.*, **119**, 857–887.

Kolmogorov, A., 1941: The local structure of turbulence in incompressible viscous fluid for very large Reynolds' numbers. *Dokl. Akad. Nauk. SSSR*, **30**, 301–305.

Krishnamurthy, R., R. Calhoun, B. Billings, and J. Doyle, 2011: Wind turbulence estimates in a valley by coherent Doppler lidar. *Meteorol. Appl.*, **18**, 361–371.

Lenschow, D. H., M. Lothon, S. D. Major, P. P. Sullivan, and G. Canut, 2012: A comparison of higher-order vertical velocity moments in the convective boudnary layer from lidar with in situ measurements and large-eddy simulation. *Boundary-Layer Meteorol.*, **143**, 107–123.

Lenschow, D. H., J. Mann, and L. Kristensen, 1994: How long is long enough when measuring fluxes and other turbulence statistics? *J. Atmos. Ocean. Tech. Technol.*, **11**, 661–673.

Lenschow, D. H., V. Wulfmeyer, and C. Senff, 2000: Measuring second- through fourth-order moments in noisy data. *J. Atmos. Ocean. Tech.*, **17**, 1330–1347.

Lindborg, E., 2006: The energy cascade in a strongly stratified fluid. *J. Fluid Mech.*, **550**, 207–242.

Lindseth, B., W. O. J. Brown, J. Jordan, D. Law, T. Hock, S. A. Cohn, and Z. Popović, 2012: A new portable 449-MHz spaced antenna wind profiler radar. *IEEE Trans. Geosci. Remote Sens.*, **50**, 3544–3553.

Lothon, M., D. H. Lenschow, and S. D. Major, 2006: Coherence and scale of vertical velocity in the convective boundary layer from a Doppler lidar. *Boundary-Layer Meteorol.*, **121**, 521–536.

—, 2009: Doppler lidar measurements of vertical velocity spectra in the convective boundary layer. *Boundary-Layer Meteorol.*, **132**, 205–226.

Lundquist, J. K. and J. D. Mirocha, 2007: Interaction of nocturnal low-level jets with urban geometries as seen in Joint Urban 2003 data. *J. Appl. Meteorol. Clim.*, **47**, 44–58.

Machol, J. L., T. Ayers, K. T. Schwenz, K. W. Koenig, R. M. Hardesty, C. J. Senff, M. A. Krainak, J. B. Abshire, H. E. Bravo, and S. P. Sandberg, 2004: Preliminary measurements with an automated compact differential absorption lidar for profiling of water vapor. *Appl Optics*, **43**, 3110–3121.

Machol, J. L., R. D. Marchbanks, C. J. Senff, B. J. McCarty, W. L. Eberhard, W. A. Brewer, R. A. Richter, R. J. A. II, D. C. Law, A. M. Weickmann, and S. P. Sandberg, 2009: Scanning tropospheric ozone and aerosol lidar with double-gated photomultipliers. *Appl Optics*, **48**, 512–524.

Mahrt, L., 1998: Flux sampling errors for aircraft and towers. *J. Atmos. Oceanic Technol.*, **15**, 416–429.

—, 1999: Stratified atmospheric boundary layers. *Boundary-Layer Meteorol.*, **90**, 375–396.

—, 2010: Common microfronts and other solitary events in the nocturnal boundary layer. *Q. J. R. Meteorol. Soc.*, **136**, 1712–1722.

—, 2011: The near-calm stable boundary layer. *Boundary-Layer Meteorol.*, **105**, 351–363.

—, 2014: Stably stratified atmospheric boundary layers. *Annu. Rev. Fluid Mech.*, **46**, 23–45.

Mahrt, L. and D. Vickers, 2002: Contrasting vertical structures of nocturnal boundary layers. *Boundary-Layer Meteorol.*, **105**, 351–363.

Mauder, M., M. Cuntz, C. Drüe, A. Graf, C. Rebmann, H. P. Schmid, M. Schmidt, and R. Steinbrecher, 2013: A strategy for quality and uncertainty assessment of long-term eddy-covariance measurements. *Agr. Forest Meteorol.*, **169**, 122–135.

McNicholas, C. and D. D. Turner, 2014: Characterizing the convective boundary layer turbulence with a High Spectral Resolution Lidar. *J. Geophys. Res.-Atmos.*, **119**, 12910–12927.

Miller, K. A. and M. H. Glantz, 1988: Climate and economic competitiveness: Florida freezes and the global citrus processing industry. *Climatic Change*, **12**, 135–164.

Mitchell, M. J., R. W. Arritt, and K. Labas, 1995: A climatology of the warm season great plains low-level jet using wind profiler observations. *Weather and Forecasting*, **10**, 576–591.

Monin, A. S. and A. M. Yaglom, 1979: *Statistical Fluid Mechanics*. MIT Press, pp. 874.

Newsom, R. K., 2012: Doppler lidar (dl) handbook. Technical Report DOE/SE-ARM-TR-101, U. S. Department of Energy, Atmospheric Radiation Measurement.

Newsom, R. K. and R. M. Banta, 2003: Shear-flow instability in the stable nocturnal boundary layer as observed by Doppler lidar during CASES-99. *J. Atmos. Sci.*, **60**, 16–33.

Neyland, L. J., 1956: Change without notice. *Flying Safety*, **14**, 16–20.

Nieuwstadt, F. T. M., 1984: The turbulent structure of the stable, nocturnal boundary layer. *J. Atmos. Sci.*, **41**, 2202–2216.

Nieuwstadt, F. T. M. and R. A. Brost, 1986: The decay of convective turbulence. *J. Atmos. Sci.*, **43**, 532–546.

O'Connor, E. J., A. J. Illingworth, I. M. Brooks, C. D. Westbrook, R. J. Hogan, F. Davies, and B. J. Brooks, 2010: A method for estimating the turbulence kinetic energy dissipation rate from a vertically pointing Doppler lidar, and independent evaluation from balloon-borne in situ measurements. *J. Atmos. Ocean. Tech.*, **27**, 1652–1664.

Päschke, E., R. Leinweber, and V. Lehmann, 2014: A one year comparison of 482 MHz radar wind profiler, RS92-SGP radiosonde and 1.5 μm Doppler ldar wind measurements. *Atmos. Meas. Tech. Discuss.*, **7**, 11439–11479.

Pearson, G., F. Davies, and C. Collier, 2009: An analysis of the performance of the UFAM pulsed Doppler lidar for observing the boundary layer. *J. Atmos. Ocean. Tech.*, **26**, 240–250.

—, 2010: Remote sensing of the tropical rain forest boundary layer using pulsed Doppler lidar. *Atmos. Chem. Phys.*, **10**, 5891–5901.

Peltola, O., A. Hensen, C. Helfter, L. Belelli Marchesini, F. C. Bosveld, W. C. M. van den Bulk, J. A. Elbers, S. Haapanala, J. Holst, T. Laurila, A. Lindroth, E. Nemitz, T. R/"ockmann, A. T. Vermeulen, and I. Mammarella, 2014: Evaluating the performance of commonly used gas analysers for methane eddy covariance flux measurements: the InGOS inter-comparison field experiment. *Biogeosciences*, **11**, 3163–3186.

Pichugina, Y. L., R. M. Banta, N. D. Kelley, B. J. Jonkman, S. C. Tucker, R. K. Newsom, and W. A. Brewer, 2008: Horizontal-velocity and variance measurements in the stable boundary layer using Doppler lidar: Sensitivity to averaging procedures. *J. Atmos. Ocean. Tech.*, **25**, 1307–1327.

Prabha, T. V., M. Y. Leclerc, A. Karipot, D. Y. Hollinger, and E. Mursch-Radlgruber, 2008: Influence of nocturnal low-level jets on eddy-covariance fluxes over a tall forest canopy. *Boundary-Layer Meteorol.*, **126**, 219–236.

Rife, D. L., J. O. Pinto, A. J. Monaghan, C. A. David, and J. R. Hannan, 2010: Global distribution and characteristics of diurnally varying low-level jets. *J. Climate*, **23**, 5041–5064.

Riley, J. J. and M.-P. Lelong, 2000: Fluid motions in the presence of strong stable stratification. *Annu. Rev. Fluid Mech.*, **32**, 613–657.

Rodgers, C. D., 2000: *Inverse methods for atmospheric sounding: theory and practice*. World Scientific, pp. 238.

Sathe, A. and J. Mann, 2013: A review of turbulence measurements using ground-based wind lidars. *Atmos. Meas. Tech.*, **6**, 3147–3167.

Sathe, A., J. Mann, N. Vasiljevic, and G. Lea, 2015: A six-beam method to measure turbulence statistics using ground-based wind lidars. *Atmos. Meas. Tech.*, **8**, 729–740.

Shapiro, A. and E. Fedorovich, 2009: Nocturnal low-level jet over a shallow slope. *Acta Geophys.*, **57**, 950–980.

—, 2010: Analytical description of a nocturnal low-level jet. *Q. J. R. Meteorol. Soc.*, **136**, 1255–1262.

Shukla, K. K., D. V. Phanikumar, R. K. Newsom, K. N. Kumar, M. V. Ratman, M. Naja, and N. Singh, 2014: Estimation of the mixing layer height over a high altitude site in Central Himalayan region by using Doppler lidar. *J. Atmos. Sol.-Terr. Phy.*, **48-53**, 48–53.

Slinger, C. and M. Harris, 2012: Introduction to continuous-wave Doppler lidar. *Summer School in Remote Sensing for Wind Energy*, Boulder, CO.

Smith, D. A., M. Harris, A. S. Coffey, T. Mikkelsen, H. E. Jørgensen, J. Mann, and R. Danielian, 2006: Wind lidar evluation at the Danish wind test site in høvsøre. *Wind Energy*, **9**, 87–93.

Soler, M. R., M. Udina, and E. Ferreres, 2014: Observational and numerical simulation study of a sequence of eight atmospheric density currents in northern Spain. *Boundary-Layer Meteorol.*, **153**, 195–216.

Song, J., K. Liao, R. L. Coulter, and B. M. Lesht, 2005: Climatology of the low-level jet at the southern great plains atmospheric boundary layer experiments site. *J. Appl. Meteorol.*, **44**, 1593–1606.

Srinivasa Rao, I., V. K. Anandan, and P. Narasimha Reddy, 2008: Evaluation of DBS wind measurement techniques in different beam configurations for a VHF wind profiler. *J. Atmos. Oceanic Technol.*, **25**, 2304–2312.

Steeneveld, G. J., M. J. J. Wokke, C. D. Groot Zwaaftink, S. Pijlman, B. G. Heusinkveld, A. F. G. Jacobs, and A. A. M. Holtslag, 2010: Observations of the radiation divergence in the surface layer and its implication for its parameterization in numerical weather prediction models. *J. Geophys. Res.*, **115**, D06107.

Stensrud, D. J., 1996: Importance of low-level jets to climate: A review. *J. Climate*, **9**, 1698–1711.

Stommel, H., 1948: The westward intensification of wind-driven ocean currents. *Trans. Amer. Geophys. Union*, **29**, 202–206.

Storm, B., J. Dudhia, S. Basu, A. Swift, and I. Giammanco, 2009: Evaluation of the weather research and forecasting model on forecasting low-level jets: Implications for wind energy. *Wind Energy*, **12**, 81–90.

Stull, R. B., 1988: *An Introduction to Boundary Layer Meteorology*. Kluwer Academic Publishers, 666 pp.

Sun, J., 2011: Vertical variations of mixing lengths under neutral and stable conditions during CASES-99. *J. Appl. Meteorol. Clim.*, **50**, 2030–2041.

Sun, J., S. P. Burns, D. H. Lenschow, R. Banta, R. Newsom, R. Coulter, S. Frasier, T. Ince, C. Nappo, J. Cuxart, W. Blumen, X. Lee, and X.-Z. Hu, 2002: Intermittent turbulence associated with a density current passage in the stable boundary layer. *Boundary-Layer Meteorol.*, **105**, 199–219.

Sun, J., L. Mahrt, R. M. Banta, and Y. L. Pichugina, 2012: Turbulence regimes and turbulence intermittency in the stable boundary layer during CASES-99. *J. Atmos. Sci.*, **69**, 338–351.

Sun, J., L. Mahrt, C. Nappo, and D. H. Lenschow, 2014: Wind and temperature oscillations generated by wave-turbulence interactions in the stabily stratified boundary layer. *J. Atmos. Sci.*, **10.1175/JAS-D-14-0129.1**, in press.

Taylor, G. I., 1938: The spectrum of turbulence. *Proc. Roy. Soc.*, **A164**, 476–490.

Ting, M. and H. Wang, 2006: The role of the North American topography on the maintenance of the Great Plains summer low-level jet. *J. Atmos. Sci.*, **63**, 1056–1068.

Tucker, S. C., W. A. Brewer, R. M. Banta, C. J. Senff, S. P. Sandberg, D. C. Law, A. M. Weickmann, and R. M. Hardesty, 2009: Doppler lidar estimation

of mixing height using turbulence, shear, and aerosol profiles. *J. Atmos. Ocean. Tech.*, **26**, 673–688.

Turner, D. D., R. A. Ferrare, V. Wulfmeyer, and A. J. Scarino, 2014a: Aircraft evaluation of ground-based Raman lidar water vapor turbulence profiles in convective mixed layers. *J. Atmos. Ocean. Tech.*, **31**, 1078–1088.

Turner, D. D., R. O. Knuteson, H. E. Revercomb, C. Lo, and R. G. Dedecker, 2006: Noise reduction of Atmospheric Emitted Radiance Interferometer (AERI) observations using principal component analysis. *J. Atmos. Ocean. Tech.*, **23**, 1223–1238.

Turner, D. D. and U. Löhnert, 2014: Information content and uncertainties in thermodynamic profiles and liquid cloud properties retrieved from the ground-based Atmospheric Emitted Radiance Interferometer (AERI). *J. Appl. Meteorol. Clim.*, **53**, 752–771.

Turner, D. D., V. Wulfmeyer, L. K. Berg, and J. H. Schween, 2014b: Water vapor turbulence profiles in stationary continental convective mixed layers. *J. Geophys. Res.-Atmos.*, **119**, 11151–11165.

Valdez, J., 2000: National weather service—a high impact agency . . . we make a difference: Reinvention goals for 2000. National Weather Service.

Van de Wiel, B. J. H., A. F. Moene, and H. J. J. Jonker, 2012a: The cessation of continuous turbulence as precursor of the very stable nocturnal boundary layer. *J. Atmos. Sci.*, **69**, 3097–3115.

Van de Wiel, B. J. H., A. F. Moene, H. J. J. Jonker, P. Baas, S. Basu, J. M. M. Donda, J. Sun, and A. A. M. Holtslag, 2012b: The minimum wind speed for sustainable turbulence in the nocturnal boundary layer. *J. Atmos. Sci.*, **69**, 3116–3127.

Van de Wiel, B. J. H., A. F. Moene, G. J. Steeneveld, P. B. amd F. C. Bosveld, and A. A. M. Holtslag, 2010: A conceptual view on inertial oscillations and nocturnal low-level jets. *J. Atmos. Sci.*, **67**, 2679–2689.

van Hooijdonk, I. G. S., J. M. M. Donda, H. J. H. Clercx, F. C. Bosveld, and B. J. H. van de Wiel, 2014: Shear capacity as prognostic for nocturnal boundary layer regimes. *J. Atmos. Sci.*, **doi: 10.1175/JAS-D-14-0140.1**, in press.

Vermeer, L. J., J. N. Sørensen, and A. Crespo, 2003: Wind turbine wake aerodynamics. *Prog. Aerosp. Sci.*, **39**, 467–510.

Waite, M. L. and P. Bartello, 2004: Stratified turbulence dominated by vortical motion. *J. Fluid Mech.*, **517**, 281–308.

Walters, C. K., J. A. Winkler, R. P. Shadbolt, J. van Ravensway, and G. D. Bierly, 2008: A long-term climatology of southerly and northerly low-level jets for the Central United States. *Ann. Assoc. Am. Geogr.*, **98**, 521–552.

Wang, Y., E. Creegan, M. Felton, D. Ligon, and G. Huynh, 2013: Investigation of nocturnal low-level jet-generated gravity waves over Oklahoma City during the morning boundary layer transition period. *J. Appl. Rem. Sens.*, **7**, 073487.

Wang, Y., C. L. Klipp, D. M. Garvey, D. A. Ligon, C. C. Williamson, S. S. Chang, R. K. Newsom, and R. Calhoun, 2007: Nocturnal low-level-jet-dominated atmospheric boundary layer observed by a Doppler lidar over Oklahoma City during JU2003. *J. Appl. Meteorol. Clim.*, **46**, 2098–2109.

Werner, C., 2005: *Lidar: Range-resolved optical remote sensing of the atmosphere*, Springer, volume 102 of *Series in Optical Sciences*, chapter Dopper wind lidar. 325–354.

Wexler, H., 1961: A boundary layer interpretation of the low-level jet. *Tellus*, **13**, 368–378.

Wharton, S. and J. K. Lundquist, 2012: Atmospheric stability affects wind turbine power collection. *Environ. Res. Lett.*, **7**, 014005.

Whiteman, C. D., X. Bian, and S. Zhong, 1997: Low-level jet climatology from enhanced rawinsonde observations at a site in the southern great plains. *J. Appl. Meteorol.*, **36**, 1363–1376.

Wulfmeyer, V., S. Pal, D. D. Turner, and E. Wagner, 2010: Can water vapour Raman lidar resolve profiles of turbulent variables in the convective boundary layer? *Bound.-Lay. Meteorol.*, **136**, 253–284.

Appendix A : List Of Acronyms

AERI	Atmospheric Emitted Radiance Interferometer
AGL	Above ground level
ARM	Atmospheric Radiation Measurement
BAO	Boulder Atmospheric Observatory
CBL	Convective boundary layer
DBS	Doppler beam swinging
DIAL	Differential Absorption Lidar
DL	Doppler lidar
DOE	Department of Energy
EET	Early evening transition
LABLE-I	Lower Atmospheric Boundary Layer Experiment (phase I)
LATTE	Lower Atmospheric Thermodynamics and Turbulence Experiment
LLJ	Low-level jet
LLNL	Lawrence Livermore National Laboratory
MCS	Mesoscale convective system
NCAR	National Center for Atmospheric Research
NWC	National Weather Center
OU	University of Oklahoma
PBL	Planetary boundary layer
PPI	Plan-position-indicator
RAP	Rapid Refresh
RHI	Range-height-indicator

SBL	Stable boundary layer
SGP	Southern Great Plains
SNR	Signal-to-noise ratio
UBL	Urban boundary layer
UTC	Coordinated Universal Time
VAD	Velocity-azimuth-display
vSBL	Very stable boundary layer
WC	WindCube v2
wSBL	Weakly stable boundary layer

Appendix B : List Of Commonly Used Symbols

$d\varphi/dz$	Directional wind shear
f	Coriolis parameter
g	Gravity
M_{11}	Second-order autocovariance function
M_{11}^{*}	Structure-function fit to second order autocovariance function
Ri	Bulk Richardson number
T	Temperature
t	Time
t_{int}	Integral time scale
u	Zonal wind
V	Mean horizontal wind speed
V_{LLJ}	Speed at base of LLJ
V_T	Threshold wind speed
v	Meridional wind
v_r	Radial velocity
w	Vertical wind
$\overline{w'^2}$	Vertical velocity variance
$\overline{w'^3}$	Third-order moment of vertical velocity
Z_{LLJ}	Height of base of LLJ
z	Height
ε	Error from noise
Θ	Azimuthal angle
θ	Potential temperature
θ_{sfc}	Potential temperature at the surface

ω	Rotation of the Earth
Φ	Elevation angle
ϕ	Latitude
σ_w	Standard deviation of vertical velocity
$\overline{\sigma_w}_{,0-100\text{m}}$	Mean vertical standard deviation between the surface and 100 m
σ_w^2	Vertical velocity variance
τ_{min}	Shortest lagtime for M_{11}^*
τ_{max}	Longest lagtime for M_{11}^*

Appendix C : List of Low-Level Jets Observed During LABLE-I

Below is a table that contains information about the LLJs that were observed during LABLE-I. A few LLJs were omitted if not all the information was available, if an instrument was not operated.

Date gives the date (in UTC time) when the LLJ was observed.

Direction is the mean LLJ direction over the night.

Max V_{LLJ} is maximum wind speed overnight with the LLJ.

$\overline{Z_{LLJ}}$ is the mean height of the LLJ.

σZ_{LLJ} is the standard deviation of the height of the LLJ.

$\overline{Z_{LLJ}}$ is the standard deviation of the vertical velocity in the lowest 100-m, as observed by the DL, over averaged over 0200–1200 UTC.

Table C.1: List and information about the LLJs observed during LABLE-I.

Date [MMDD]	Direction [° from]	Max V_{LLJ} [m s^{-1}]	$\overline{Z_{LLJ}}$ [m]	σZ_{LLJ} [m]	$\overline{\sigma_{w,0-100\text{m}}}$ [m^2 s^{-2}]
0929	87	10.4	197	44	0.17
0930	88	10.3	377	47	0.14
1002	19	22.6	412	116	0.52
1003	190	8.4	122	57	0.08
1004	193	23.1	342	113	0.07
1005	45	13.2	411	256	0.61
1006	45	13.0	409	210	0.15
1009	197	23.7	365	99	0.10
1010	48	16.3	381	142	0.16
1012	215	17.7	647	290	0.10

Date [MMDD]	Direction [° from]	Max V_{LLJ} [m s^{-1}]	$\overline{Z_{LLJ}}$ [m]	σZ_{LLJ} [m]	$\overline{\sigma_{w,0-100\mathrm{m}}}$ [m^2 s^{-2}]
1013	191	28.6	557	109	0.27
1014	291	23.3	332	135	0.26
1015	249	13.3	149	27	0.05
1016	214	27.4	349	42	0.47
1020	232	19.4	727	295	0.06
1021	194	19.0	417	103	0.07
1022	198	31.1	600	83	0.52
1023	206	27.8	614	186	0.47
1024	205	26.7	475	47	0.54
1029	161	12.0	99	28	0.09
1030	217	16.4	260	134	0.05
1031	55	13.5	228	98	0.13
1102	186	20.6	507	274	0.08
1103	1	17.7	447	48	0.32
1108	163	27.4	300	107	0.07
1109	206	31.7	681	119	0.50
1110	206	34.4	693	130	0.63
1111	192	34.8	1177	134	0.70